Studies on Interference Compensation Techniques and Performance Evaluation for Digital Radio Systems

Graduate School of Systems and Information Engineering

University of Tsukuba

March 2015

Shuta Uwano

Abstract

This dissertation presented research results regarding techniques that improve interference compensation and performance evaluation in digital radio systems. As mobile Internet access becomes more widely used and the ubiquity of radio communication devices increases, interference issues will becomes more serious in light of the lack of unused frequency bands. Interference compensation techniques must be established in order to avoid interference in the same system and the interference between different systems, or to expand the coverage area. Interference compensation techniques should be provided without the need to change standard specifications, because interference may not always occur. However, conventional interference compensation schemes have four main problems that must be addressed to achieve high performance in digital radio systems. (1) The problem of adjacent channel interference (ACI) in the wireless local area network (LAN) system is caused by nonlinear distortion characteristics of high power amplifiers at the transmitter. (2) The problem of co-channel interference (CCI) occurs between base stations (BSs) in Personal Handy-phone System (PHS) when there is mutual overlapping in a zone in a mixed cell architecture. (3) The problem of the same path interference (SPI) between two routes in a fixed microwave communication system occurs when the desired signal level is degraded by fading. (4) The problem of intersymbol interference (ISI) between multiple radio repeaters in a wireless LAN occurs due to the delay difference between the two received waves.

In this study, in order to resolve these problems, the following four techniques were established. (1) A novel technique to suppress ACI at a transmitter is proposed, which is named Linearized Constant Peak-power Coded OFDM (LCP-COFDM) transmission and compensates nonlinear distortion in broadband wireless OFDM systems such as wireless LAN, WiMAX, and LTE. The proposed technique abates ACI by suppressing the out-of-band emission due to nonlinear distortion. (2) A technique to avoid interference using specific antenna patterns is proposed. Where both microcells and macrocells co-exist in the same geographical urban area, the BS antennas mounted on the rooftops of buildings to cover wide circular radio zones suffer severe CCI from the surrounding low BSs. The combination of the beam tilt and horizontal polarization reduces the CCI. (3) As a technique to cancel SPI from received signals, the Extraction and Reinjection-type Interference Canceller (ERIC) is recommended. This interference canceller is more advantageous than other cancellers because it can be applied under various severe interference conditions. (4) A non-regenerative repeating technique comprising multiple radio repeaters was established without generating ISI. A new radio repeater, the CE, was proposed that targets 5-GHz broadband wireless access systems to improve the coverage probability without the need to set up a new AP. The following summarizes the results obtained this research.

In Chapter 3, LCP-COFDM is proposed, which combines the CP-OFDM technique with baseband predistortion. The proposed technique significantly reduces out-of-band power emission

and ACI by more than 10 dB, respectively. In this case, given the propagation distance characteristic expressed as a power decay of 2.9 , LCP-COFDM allows the distance between the desired station and adjacent interfering station to be reduced to 1/3 that when not using LCP-COFDM. As a result, multiple APs can coexist without interfering with each other in a small area.

In Chapter 4, an antenna technique to avoid CCI is proposed, which is the combination of beam tilt and horizontal polarization. The proposed technique significantly reduces the CCI level by approximately 23 dB, which is equivalent to a reduction to 1/200 of the interference level that the BS receives. The distance between the interference receiving BS and the interfering BS can be shortened to approximately 1/6.

In Chapter 5, a theoretical evaluation is performed using the ERIC, and the degree of improvement in the interference cancellation is estimated using this canceller in a fading environment. The results clarify that this canceller is the most valid when the average received signal power rate, D/U, is 20 dB, and the maximum improvement using this canceller is 7.5 times better than without using this canceller. The quality-degradation time due to the interference can be shortened from 28 seconds to 3.7 seconds per 50 km per month for the 16-QAM system in a fixed microwave communication system.

In Chapter 6, a new radio repeater, the CE, is proposed that targets 5-GHz broadband wireless access systems to improve the coverage probability without the need to set up a new AP. It is clarified that multiple CEs can use the same second frequency and provide better coverage with useful macro diversity gain in 5-GHz indoor environments, because when the delay difference between the two received waves is less than 300 ns, the ISI can be removed using the guard interval in an OFDM system.

The above research results show fundamental data regarding interference compensation for the exiting digital radio systems.

Contents

Chapter 1

Introduction

1. Introduction

1.1 Background

Triggered by the diffusion of the Internet, the number of users who use mobile Internet access has continued to increase over the past decade, and the demand for higher-speed applications has become ubiquitous. There is a definite lack in the number of radio frequency bands for wireless communications, and this fact influences frequency reallocation in various fields of industry. Frequency reallocation has been repeatedly implemented as digitization has progressed in radio systems for telecommunications, broadcast, business use, and disaster prevention.

Table 1.1 shows the history of cellular systems. The original purpose for digitization in cellular systems was to enhance the accommodation rate for each frequency channel in order to increase the number of telephone users. However, since the 2000s, the transmission speed has increased rapidly to more than 100 fold [1.1], [1.2]. On the other hand, wireless local area networks (LANs) were developed for data communications from the beginning. As shown in Table 1.2, the transmission speed of wireless LAN has not improved to the point of cellular systems, reaching only approximately 10 fold during the same period [1.3], [1.4].

Figure 1.1 shows the change and forecast for the number of smartphone subscribers [1.5]. Smartphones have spread among the population in a short period after the iPhone was commercialized in 2008. They currently exceed half of the cellular phone market and it is predicted that the smartphones will exceed 70% by March 2019. Many smartphone users use Social Networking Services (SNSs) such as LINE, Twitter, or Facebook. Services for watching videos or animations, such as YouTube, are accessible in a train with a smartphone. The demand for high-speed data communications will increase further with the increasing number of people using smartphones in mobile environments.

Various high-speed transmission techniques have been applied to mobile communication systems and wireless LAN systems such as Orthogonal Frequency Division Multiplexing (OFDM) [1.6], Multiple Input Multiple Output (MIMO) [1.7], [1.8], Multi User MIMO (MU-MIMO) [1.9], [1.10] and Carrier Aggregation (CA). In particular, OFDM is an epoch making transmission technique and is employed by many transmission systems including cellular, wireless LAN, digital terrestrial broadcasting, and disaster radio. This is because it provides superior frequency utilization efficiency with multicarrier modulation to overcome multipath fading. However, OFDM signals may suffer from intermodulation distortion among subcarriers caused by the nonlinearity of the high-power amplifier (HPA). This nonlinear distortion degrades the own transmission quality and since it causes the spectrum to expand significantly, these out-of-band emissions result in interference to adjacent frequency channels. Since OFDM is a very important modulation technique that will most likely be used in the future, the nonlinear distortion technique is being studied with increasing intensity.

Table 1.1 History of mobile communication systems.

	Release year	Standard	Frequency band	Transmission speed	Main service
1 G	1980	HiCAP (Analog)	800 MHz		Voice
2 G	1993	PDC	800 MHz and 1.5 GHz	10 kbps	Voice, Email
	1995	PHS	1.9 GHz	64 kbps	Voice, Low-speed data
3 G	2001	W-CDMA CDMA2000	2 GHz	384 kbps	Voice, Picture, Low-speed data
	2009	WiMAX	2.5 GHz	40 Mbps	Middle-speed data
3.9 G	2010	LTE	800 MHz, 1.5 GHz, 1.7 GHz, and 2 GHz	100 Mbps	Video, High-speed data
4 G	2016	LTE-Advanced	3.4 GHz – 3.6 GHz	1 Gbps	High-speed data
5 G	2020	Planning stage		10 Gbps	High-definition video

HiCAP : High Capacity
PDC : Personal Digital Cellular
PHS : Personal Handyphone System
CDMA2000 : Code Division Multiple Access 2000
W-CDMA : Wideband Code Division Multiple Access
WiMAX : Worldwide Interoperability for Microwave Access
LTE : Long Term Evolution

Table 1.2 History of wireless LAN systems.

802.11 protocol	Release year	Frequency band	Maximum PHY layer rate	Modulation	MIMO streams
802.11	1997	2.4 GHz	2 Mbps	DSSS, FHSS	N/A
802.11a	1999	5 GHz	54 Mbps	OFDM	N/A
802.11b	1999	2.4 GHz	11 Mbps	DSSS	N/A
802.11g	2003	2.4 GHz	54 Mbps	OFDM	N/A
802.11n	2007	2.4 GHz and 5 GHz	600 Mbps	OFDM	4
802.11ac	2013	5 GHz	1,300 Mbps	OFDM	8

DSSS : Direct Sequence Spread Spectrum
FHSS : Frequency Hopping Spread Spectrum
OFDM : Orthogonal Frequency Division Multiplexing
MIMO : Multiple Input Multiple Output

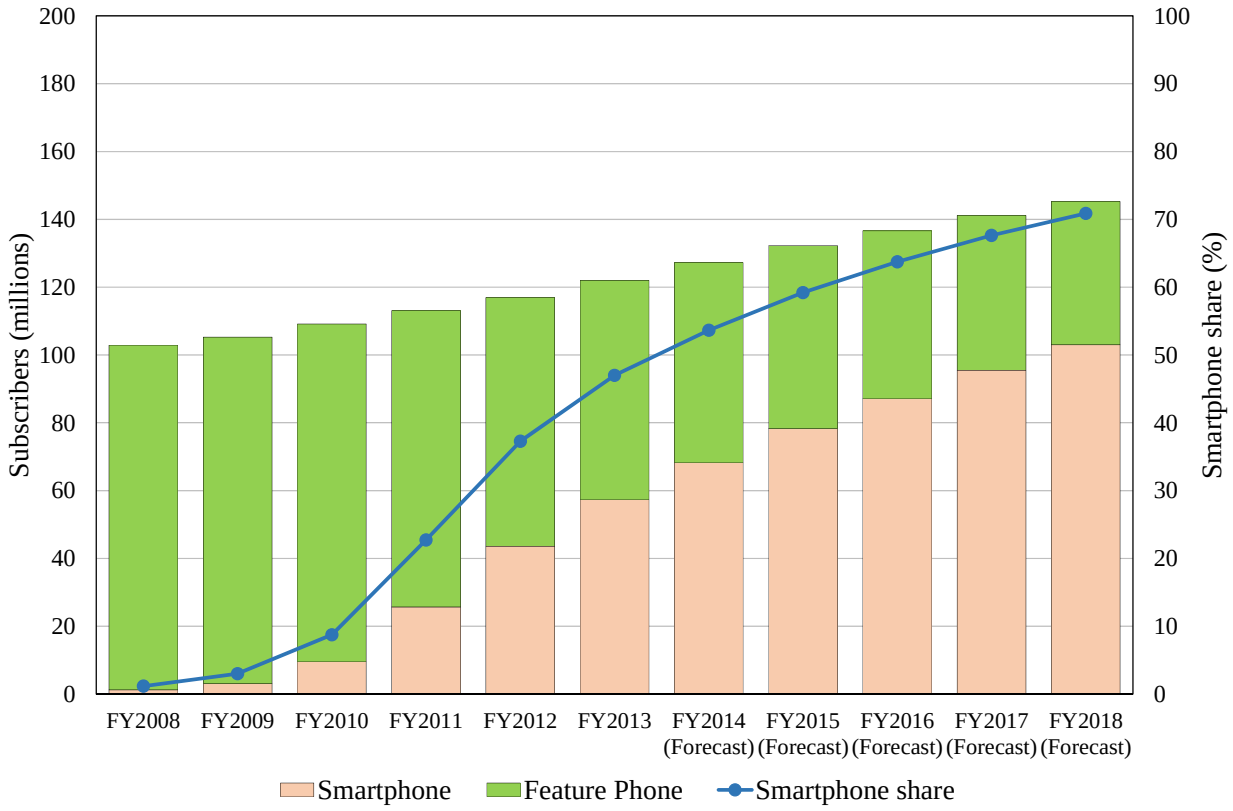

Fig. 1.1 Change and forecast in the number of smartphone subscribers.

1.2 Aims and objectives

Although high-speed transmission techniques improve the channel capacity or the user capacity in wireless communication systems, if the demand for high-speed mobile Internet connections exceeds the capacity, more radio frequency bands will be required. Consequently, unexpected interference locally or temporarily will occur.

Figure 1.2 shows three examples of interference problems facing various wireless systems. In the case of wireless LAN systems, as shown in Fig. 1.2(a), they operate using radio frequencies in the unlicensed 2.4 GHz band and 5 GHz band. An access point (AP) generally searches for and uses an unused frequency channel. If an unused channel is not available, the wireless LAN devices that use the same channel can avoid interfering with each other by autonomously using carrier sense multiple access (CSMA) operation. However, wireless LAN devices suffer from adjacent channel interference (ACI) from other devices caused by out-of-band emissions generated from nonlinear distortion [1.11].

Next, in the case of the personal handy-phone system (PHS) in Fig. 1.2(b), autonomous distribution control is adopted to assign frequency channels. When receiving a connection request from a terminal station, the base station (BS) automatically selects an idle frequency channel from among all frequency bands assigned to PHS and employs that channel. Autonomous distribution control makes it easy for PHS system designers to establish more BSs without full cell design in which all frequency channels are allocated. However, in crowded telecommunication traffic areas, when the number of BSs exceeds the number of frequency channels, autonomous distribution control finally fails and co-channel interference (CCI) occurs between overlapping BSs [1.12], [1.13]. CCI is likely to occur when users crowd into locations such as train stations or busy shopping streets in urban areas.

In the third case, as shown in Fig. 1.2(c), a fixed microwave communication system transmits a variety of information such as telephone, television, and data using super high frequency (SHF) radio, which constitutes a long-distance country wide radio route that hops through multiple radio relay stations [1.14]. In 1990, the 4/5/6G-150M system using 16-QAM and 4/5/6G-300M system using 256-QAM were put into practical use, corresponding to international standard Synchronous Digital Hierarchy (SDH). Some fading compensation techniques such as digital transversal equalization, Forward Error Correction (FEC) [1.15], and Cross Polarization Interference Cancelation (XPIC) were applied to the systems to prevent quality degradation of multilevel quadrature amplitude modulation [1.16]. Because the radio routes are concentrated into large metropolitan areas, it is necessary to design radio routes with careful attention to the interference between the routes. However, when the desired signal level is degraded by fading without suppressing the interference level, the quality of the desired signal is degraded from the interfering signal in that moment. The source of fading in fixed microwave communications is a momentary drop in the signal strength due to fluctuations in the propagation parameters such as atmospheric

refraction or sea surface reflection due to changes in the weather.

For the 16-QAM system in the fixed microwave communication system, the route outage probability that the bit error rate (BER) can exceed 1E-4 is limited to less than approximately 28 seconds per 50 km in any month [1.14]. When the desired-to-undesired (D/U) signal ratio is approximately 20 dB, the BER is 1E-4. Although the trunk route is designed so that the static D/U ratio exceeds 45 dB, the D/U ratio may sometimes decrease significantly under the influence of fading. An interference compensation technique is required that will improve the D/U ratio to more than 20 dB under fading conditions.

In the fourth case, an example of a public wireless LAN service provided in an underground shopping mall is shown in Fig. 1.2(d). When the mobile terminal (MT) in this figure cannot receive radio waves from the AP directly, a radio repeater can connect the devices as a gap filler. Although this blind zone can also be covered using the bridge mode of an AP, additional APs are costly and the throughput is reduced to half because the data transmission requires double the time. Thus, it is more desirable to employ several simple radio repeaters so that throughput is not degraded. However, interference occurs if the radio waves of the same channel coming from multiple radio repeaters are received at one MT. The interference in this case results in intersymbol interference (ISI) [1.17], [1.18]. On the other hand, OFDM transmission is known to possess the ability to suppress some ISI through the use of a guard interval. Utilizing this ability, the coverage area of the AP can be expanded without incurring ISI.

In this dissertation, an interference compensation scheme is proposed and the performance of the scheme is evaluated. As described above, some interference problems occur in the current systems when traffic temporarily exceeds the system capacity or when the propagation environment changes briefly. It is desirable to address the interference problems by means of adding small functions within the specifications without redesigning the system architecture. It is very important to estimate from an appropriate viewpoint to what degree the proposed interference compensation technique can improve the performance for each system.

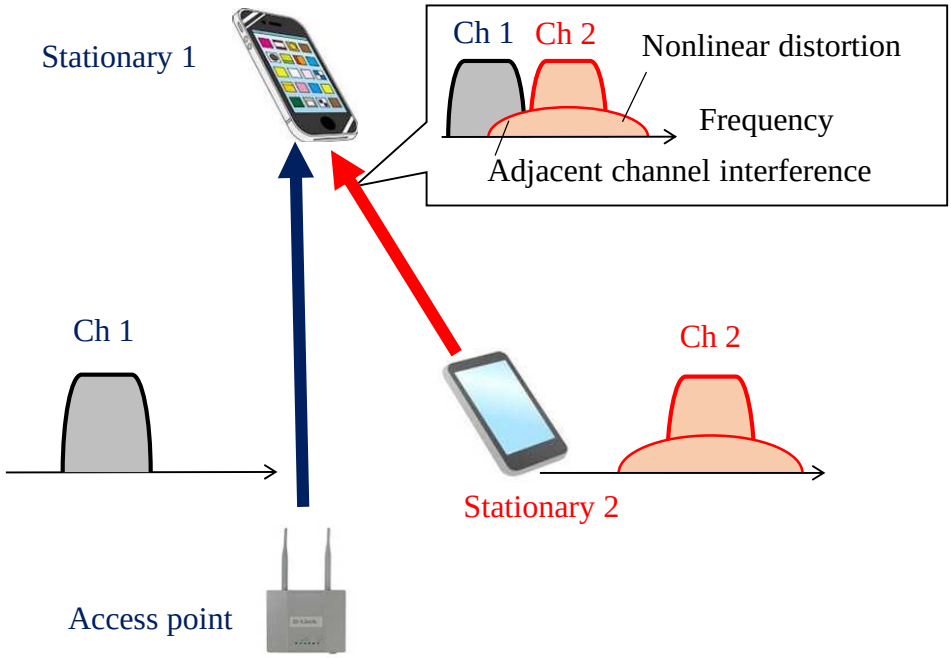

1.2(a) Wireless LAN

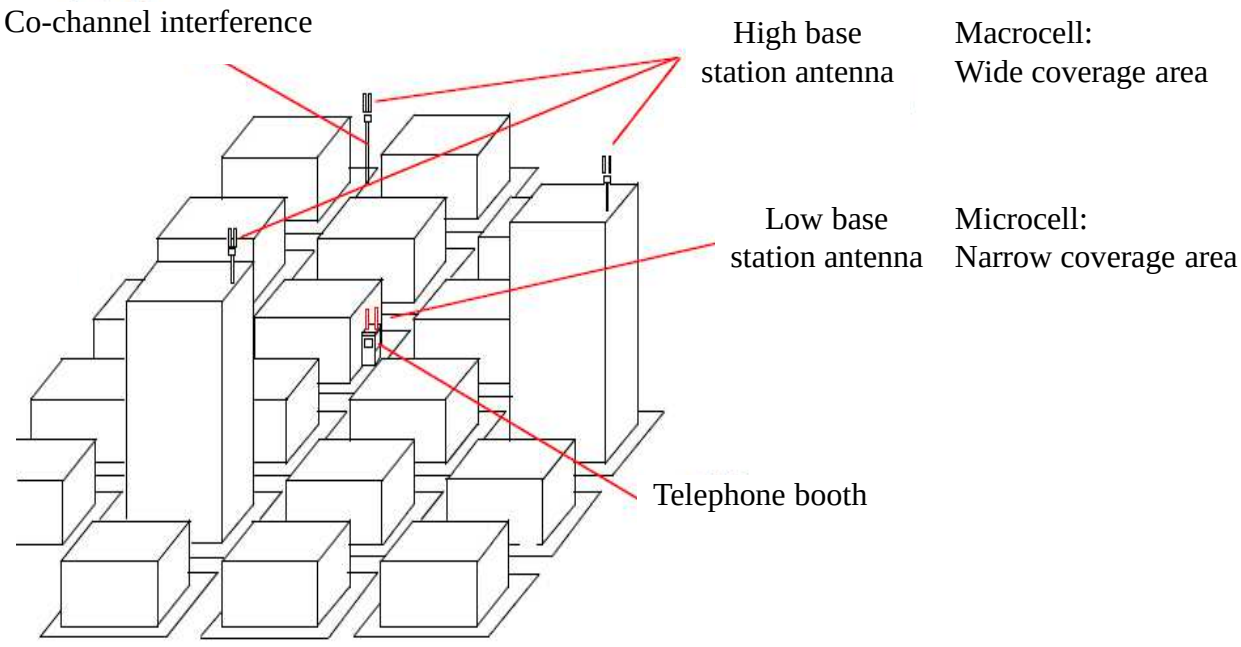

1.2(b) PHS

Fig. 1.2 Interference problems facing various wireless systems.

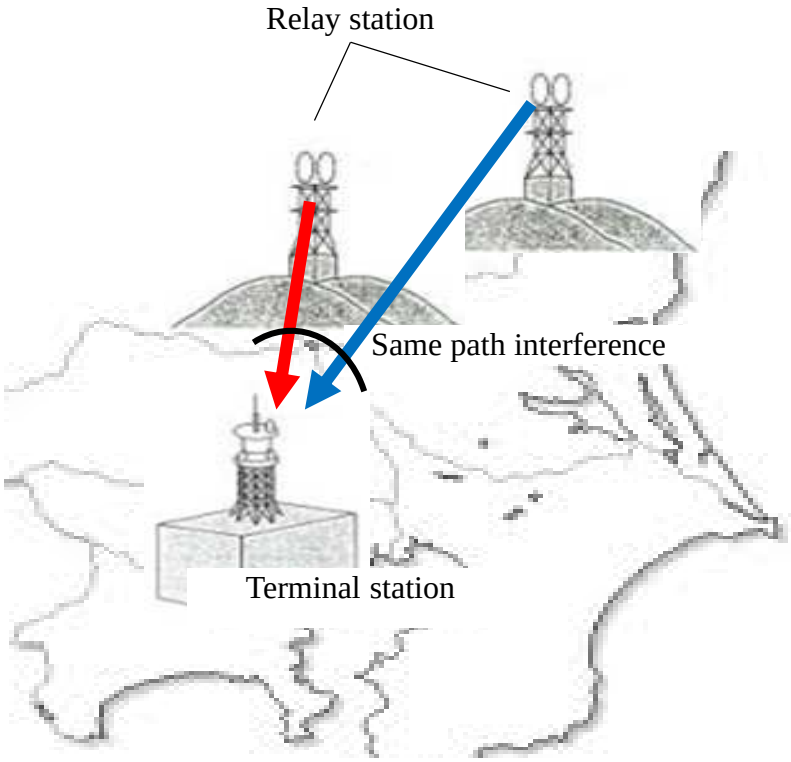

1.2(c) Fixed microwave communications

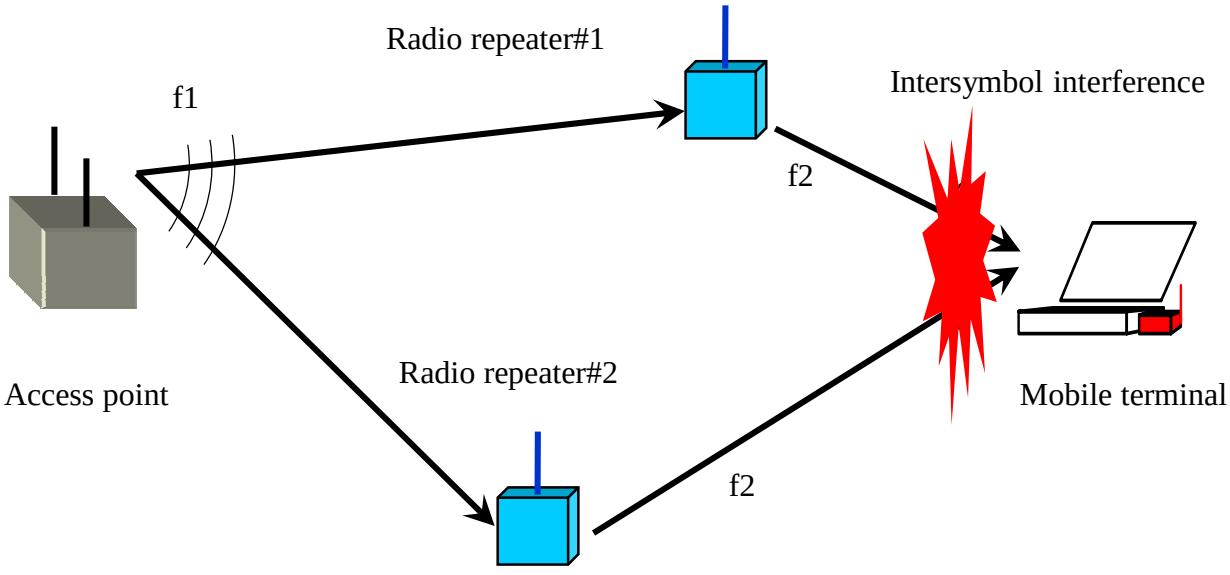

1.2(d) Radio repeaters in wireless LAN system

Fig. 1.2 Interference problems facing various wireless systems.

1.3 Dissertation structure

The flow of the dissertation is shown in Fig. 1.3. This dissertation consists of seven chapters.

Chapter 2 gives an overview of technologies and issues regarding advanced interference compensation techniques. Interference is classified based on various perspectives and fundamental technologies for interference compensation are reviewed.

Chapter 3 describes a technique to suppress interference at a transmitter, and proposes Linearized Constant Peak-power Coded OFDM (LCP-COFDM) transmission as a novel technique for compensating nonlinear distortion in broadband wireless OFDM systems such as wireless LAN, WiMAX [1.19], and LTE [1.20], [1.21]. The proposed technique abates adjacent channel interference (ACI) by suppressing the out-of-band emission due to nonlinear distortion. This chapter verifies the validity of using the proposed linearizer in terms of increased system capacity.

Chapter 4 describes a technique to avoid interference using specific antenna patterns, and addresses the problem of CCI generated in a mixed cell architecture in PHS. Where both microcells and macrocells co-exist in the same geographical urban area, the BS antennas mounted on the rooftops of buildings to cover wide circular radio zones suffer severe CCI from the surrounding low BSs. The combination of the beam tilt and horizontal polarization reduces the CCI.

Chapter 5 describes a technique to cancel interference from received signals, and recommends an Extraction and Reinjection-type Interference Canceller (ERIC). This interference canceller is more advantageous than other cancellers because it can be applied under various severe interference conditions. It is particularly effective in the case of the same path interference (SPI), in which the propagation path of the desired signal is the same as that for the interfering signal. The degree of improvement in interference cancellation is estimated when using this device under fading conditions.

Chapter 6 describes a technique to synthesize interference to desired signals, and proposes a radio repeater for broadband wireless access (BWA) systems, which is called a cell enhancer (CE), to expand the coverage area without the need to establish a new AP. This repeater adopts a non-regenerative repeating scheme to transfer signals using relatively simple circuits [1.22]. The repeater actualizes double frequency networks (DFNs) using two different frequency channels synchronized to the AP [1.23]. The repeater achieves synchronization by demodulating the control signals broadcast from the AP. Simulation evaluations of the CE performance are discussed and as one consequence it is apparent that using multiple CEs yields a useful macro diversity gain with little ISI in indoor environments.

Chapter 7 describes the conclusions on the work and summarizes the performance of techniques proposed in this dissertation.

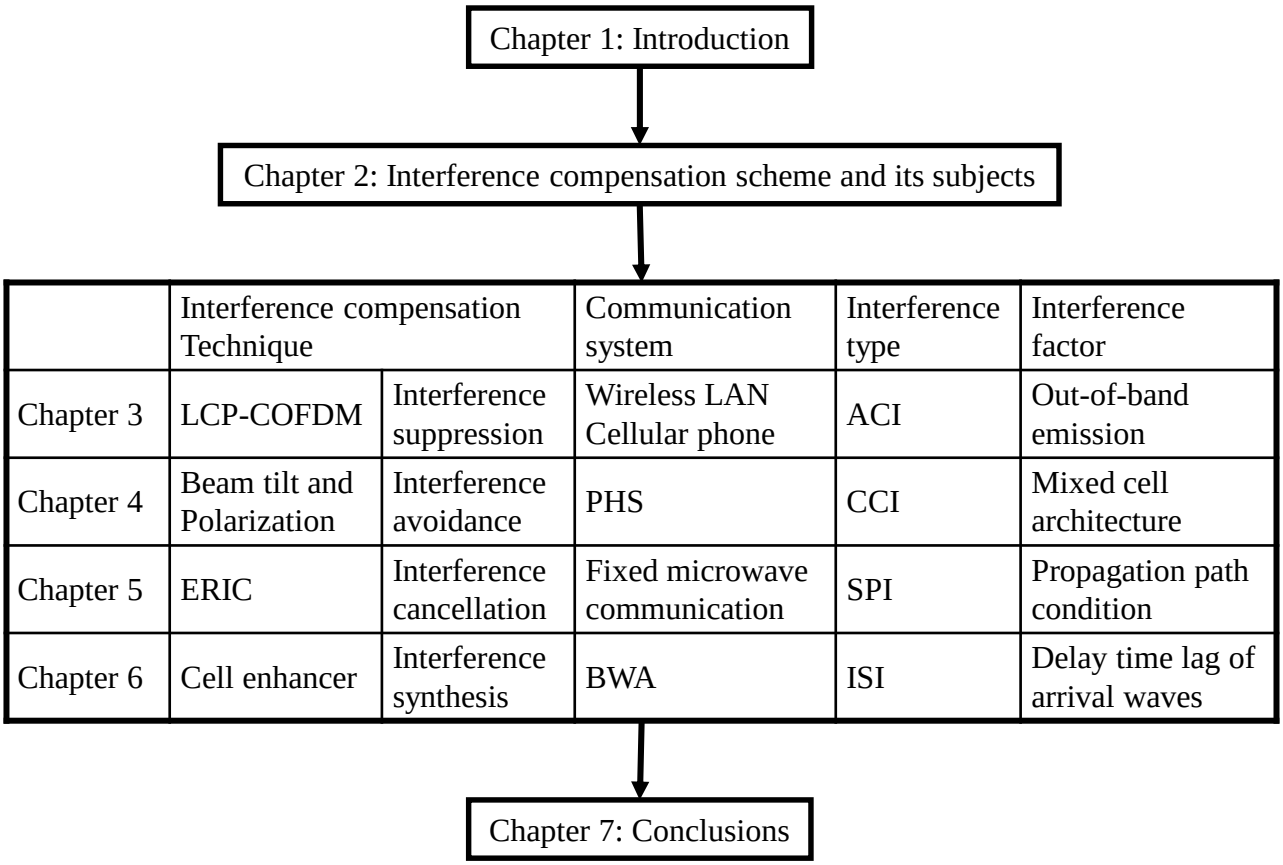

	Interference compensation Technique		Communication system	Interference type	Interference factor
Chapter 3	LCP-COFDM	Interference suppression	Wireless LAN Cellular phone	ACI	Out-of-band emission
Chapter 4	Beam tilt and Polarization	Interference avoidance	PHS	CCI	Mixed cell architecture
Chapter 5	ERIC	Interference cancellation	Fixed microwave communication	SPI	Propagation path condition
Chapter 6	Cell enhancer	Interference synthesis	BWA	ISI	Delay time lag of arrival waves

LCP-COFDM: Linearized Constant Peak-Power Coded OFDM
ERIC: Extraction and Reinjection-type Interference Canceller
ACI: Adjacent Channel Interference
CCI: Co-Channel Interference
SPI: Same Path Interference
ISI: Intersymbol Interference

Fig. 1.3 Structure of dissertation.

References for chapter 1

[1.1] S. Stefan, et al, “LTE Advanced – Evolving LTE towards IMT-Advanced,” IEEE VTC 2008-Fall, pp.1-5, Sept. 2008.

[1.2] Astely, et al, “LTE: The Evolution of Mobile Broadband,” IEEE Communications Magazine, PP.44-51, April 2009.

[1.3] M. Tauber, S. N. Bhatti and Yi Yu, “Application Level Energy and Performance Measurements in a Wireless LAN,” Green Computing and Communications, pp.100-109, Aug., 2011.

[1.4] M. Tauber, S. N. Bhatti and Yi Yu, “Towards Energy-Awareness in Managing Wireless LAN Applications,” IEEE/IFIP Network Operations and Management Symposium, pp.453-461, April, 2012.

[1.5] “Lifestyle and Work Style Transformations Caused by ICT Advancement,” 2014 WHITE PAPER Information and Communications in Japan, Chapter 4, section 1, pp.33-38, Ministry of Internal Affairs and Communications, Japan, 2014.

[1.6] R. van Nee and R. Prasad, OFDM for wireless Multimedia Communications, Artech House Publishers, 2000.

[1.7] S. M. Alamouti, “A Simple Transmit Diversity Technique for Wireless Communications,” IEEE J. Select. Areas in Comm., vol. 16, No. 8, pp.1451-1458, Oct. 1998.

[1.8] S. Kurosaki, Y. Asai, T. Sugiyama and M. Umehira, “A SDM-COFDM Scheme Employing a Simple Feed-Forward Inter-Channel Interference Canceller for MIMO Based Broadband Wireless LANs,” IEICE Trans. Commun., vol. E86-B, No. 1, pp.283-290, Jan. 2003.

[1.9] D. Gesbert, et al, “Shifting the MIMO Paradigm,” IEEE Signal Processing Magazine, Vol. 24, Issue 5, pp.36-46, Sept. 2007.

[1.10] K. Nishimori, et al, “16x16 Multiuser MIMO Testbed Employing Simple Adaptive Modulation Scheme,” IEEE VTC 2009-Spring, pp.1-5, April 2009.

[1.11] M. Gudmundson and P. O. Anderson, “Adjacent channel interference in an OFDM system,” IEEE VTC 1996, Mobile Technology for the Human Race., vol. 2, pp.918-922, April 1996.

[1.12] Y. Yu-Dong and A. U. H. Sheikh, “Investigations into cochannel interference in microcellular mobile radio systems,” IEEE Trans. on Vehicular Technology, vol. 41, Issue 2, pp.114-123, May 1992.

[1.13] A. Ando, K. Kondo and S. Kubota, “A Study of Radio Zone Length of Dual-Polarized Omnidirectional Antennas Mounted on Rooftop for Personal Handy-Phone System,” IEEE Trans. on Vehicular Technology, vol. 57, Issue 1, pp.2-10, Jan. 2008.

[1.14] T. Murase, A. Hashimoto and J. Segawa, “Design and Performance of SDH Based Microwave Digital Radio Systems,” ECRR Proc. 3rd, pp.48-55, 1991.

[1.15] S. Aikawa, T. Okuno, R. Ohmoto and M. Hatai, “Bit Interleaving Technique as a Radar Interference Canceler in Digital Microwave Radio Systems,” IEEE ICC'92, vol.3, pp.1482-1486, June 1992.

[1.16] H. Matsue, H. Ohtsuka and T. Murase, “Digitalized Cross-Polarization Interference Canceller for Multilevel Digital Radio,” IEEE J. Select. Areas in Comm., vol. 5, No. 3, pp.493-501, April 1987.
[1.17] N. Mochizuki et al, “A High Performance Frequency and Timing Synchronization Technique for OFDM,” IEEE GCOM’98, vol. 6, pp. 3443-3448, Nov. 1998.
[1.18] T. Onizawa, et al, “A Novel Channel Estimation Scheme Employing Adaptive Selection of Frequency-Domain Filters for OFDM Systems,” IEICE Trans. Commun., vol. E82-B, No.12, pp.1923-1931, Dec. 1999.
[1.19] IEEE Std 802.16-2009, “IEEE Standard for Local and metropolitan area networks Part 16: Air Interface for Broadband Wireless Access Systems”, May 2009.
[1.20] 3GPP TS 36.201, “Evolved Universal Terrestrial Radio Access (E-UTRA); LTE Physical Layer - General Description (Release 8),” V8.1.0, Nov. 2007.
[1.21] 3GPP TS 36.211, “Evolved Universal Terrestrial Radio Access (E-UTRA); Physical Channels and Modulation (Release 8),” V8.3.0, May. 2008.
[1.22] K. Watanabe, “Estimation Method of Route Outage Probability in Non-regenerative Repeater Digital Microwave Radio Systems,” IEICE Trans. Commun., Vol. E81-B, No. 1, pp.89-95, Jan. 1998.
[1.23] A. M. Gallardo, M. E. Woodward and J. R. Tellez, “Performance of DVB-T OFDM based single frequency networks: effects of frame synchronization, carrier frequency offset and non-synchronized sampling errors,” IEEE VTC 2001-Fall, pp. 962-966, Oct. 2001.

Chapter 2

Technologies and Issues Facing Interference Compensation

2. Technologies and Issues Facing Interference Compensation

2.1 Classification of interference issues

In this section, interference issues facing digital radio systems are classified from the standpoint of interference compensation techniques. Herein, interference is defined briefly as a receiving antenna receiving an undesired interfering wave in addition to a desired wave. This occurs when both radio waves are used in the same radio frequency band and are received at the same time and under the same spatial conditions. In other words, interference issues do not occur if even one of three conditions, i.e., the radio frequency band, time, or space can be separated between the desired signal and interference signal. These three dimensions are shown in Fig. 2.1. Interference becomes problematic when the removal of the interference is so difficult that the interfering signal is hard to distinguish from the desired signal because the interference is very similar to the desired signal. In other cases, the removal of the interference is difficult when the interference source cannot be identified because the interference occurs suddenly and unexpectedly. In the case where the interference signal can be separated based on the radio frequency band, the interference is classified according to the interference caused between the same operators or the interference caused between different operators. In the case of the same operator, the interference problems can be resolved through system control, that is, channel separation becomes possible by properly reallocating the radio frequency channels, assigning timing slots correctly, or effectively adjusting the transmission power. Conversely, in the case of different operators, because the system control solution is impossible, regulation is required to limit the radio frequency spacing, separation distance, transmission power, antenna pattern, or device count.

Next, in a case where the interference signal can be separated in the time domain, a wireless LAN system can prevent interference by utilizing carrier sensing before packets are transmitted. Another example is if a device connected to a wireless LAN detects a radar signal, it should stop using the radio frequency channel immediately and should employ the Dynamic Frequency Selection (DFS) function which changes the other radio frequency channel.

Finally, when an interfering signal is received in the same frequency band and at the same time as the desired signal, it is extremely difficult to separate the interference signal by using spatial parameters as the last method in the three dimensions in Fig.2.1. Phase components and amplitude components of the received signals are included in the spatial parameters. Strictly speaking, since the transmitter antenna of the interference wave is different from that of the desired wave, the spatial parameters of both signals are different. Despite this, it is not guaranteed that the two signals can be distinguished using the spatial parameters, unlike with radio frequency and time domain cases. For example, in the case that an interfering wave is received by the receiving antenna in the same direction and in the same propagation distance range as the desired wave, both spatial parameters of the two radio waves are similar. Then the interference canceller must remove the interfering wave in the received signal with high accuracy. There are other methods that decrease the occurrence rate of

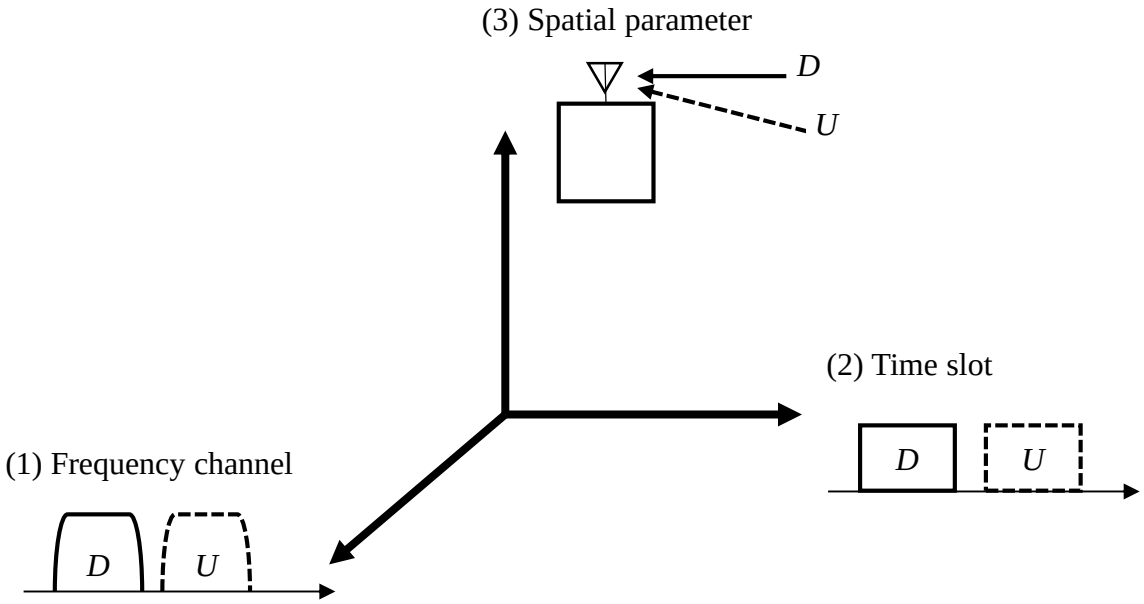

Fig. 2.1 Three methods for separating interference signal.

the desired and interfering waves arriving under the same conditions. These methods use antenna radiation patterns such as beam tilt or use orthogonal polarization. Chapter 4 describes a technique to avoid interference using the combination of beam tilt and orthogonal polarization. If available, in the case of interference between known systems, the rule to avoid interference is decided based on which system has priority. An example based on radio law involving a fixed communication system and a satellite system, is that the elevation angle of an antenna used in the fixed communication system should be inclined below the direction of the satellite.

2.2 Fundamental technologies for interference compensation

In Section 1.2, ACI is described to be caused by out-of-band emissions due to nonlinear distortion of the HPA. There are two types of methods by which nonlinear distortion is reduced. One method is the feedforward technique, and the other is the predistortion technique. Figure 2.2 shows a configuration for the feedforward amplifier at the transmitter [2.1]. The transmission signal is divided before amplification. One part of the signal is amplified by the HPA and is added by Adder 1 to the other signal without amplification after adjusting the signals to the same amplitude and reverse phase. As a result, the nonlinear distortion component can be extracted. Subsequently, amplified by

an auxiliary amplifier, the extracted nonlinear distortion is added by Adder 2 to the output signal of the HPA after adjusting the signals to the same amplitude and reverse phase. Consequently, the nonlinear distortion in the HPA output signal can be cancelled.

On the other hand, in the predistortion technique as shown in Fig. 2.3, the transmission signal is multiplied by inverse characteristic F^{-1} of the nonlinear distortion characteristic, F, at the predistortion circuit in front of the HPA [2.2], [2.3]. By multiplying the predistortion characteristic beforehand and providing nonlinear distortion with the HPA later, the final characteristic can be linearized. Consequently, the nonlinear distortion can be reduced. The predistortion technique has come into common use recently because it can generate inverse characteristics with baseband processing unlike the feedforward technique which requires the auxiliary amplifier. Chapter 3 describes the baseband predistortion technique proposed for OFDM systems.

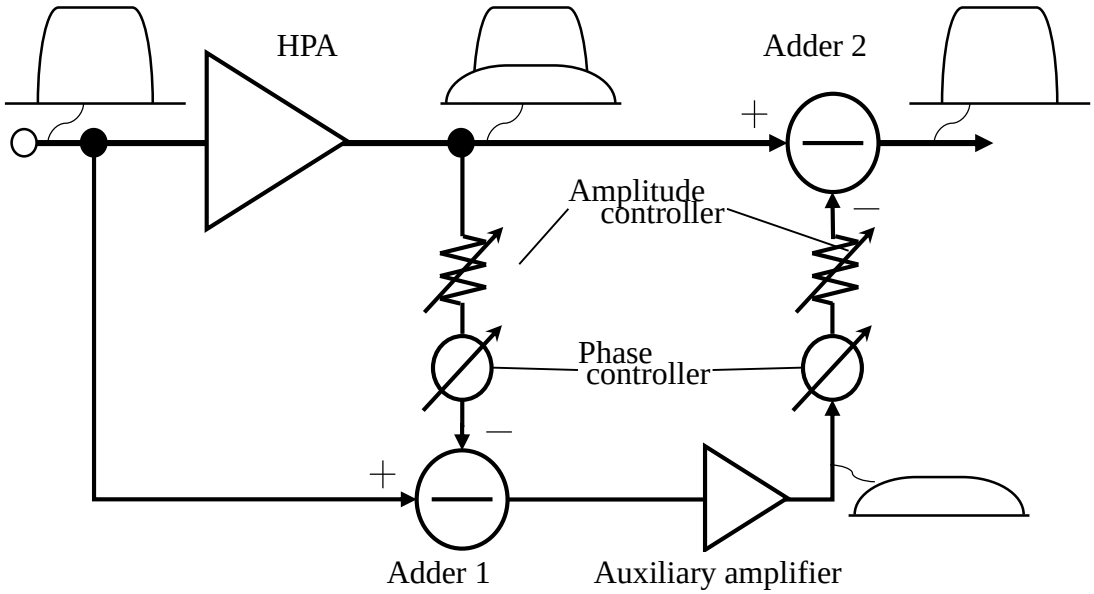

Fig. 2.2 Feedforward scheme.

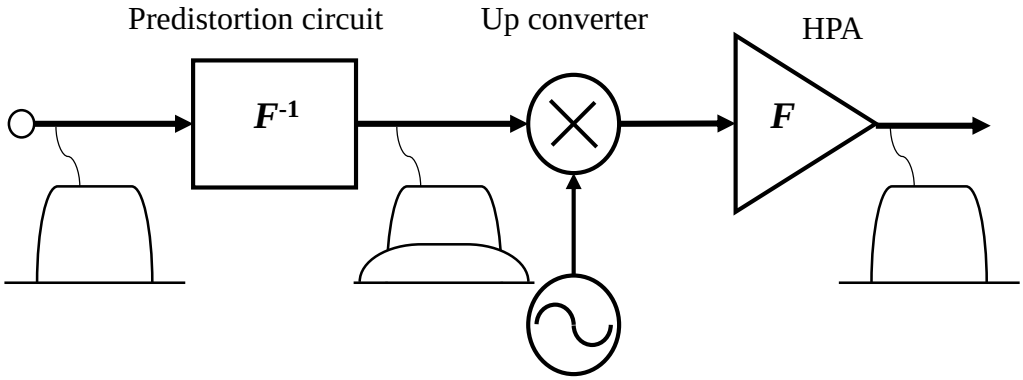

Fig. 2.3 Predistortion scheme.

Typical examples of an interference canceller that removes the CCI are shown in Fig. 2.4, where they are classified based on the method for generating the replica signal. The principle operation of an interference canceller is to produce a replica signal of the interference signal, and to cancel the actual interference signal involved in the received signal using this replica signal. The performance of an interference canceller is very sensitive to errors in the replica signal. In the study of interference cancellers, attention has been focused on how the replica signal can be produced accurately at the receiver. Fig. 2.5 shows the configuration of an FM interference canceller (FMIC) for the fixed digital microwave communication system, which suffers interference from FM signals [2.4]. Although a phase locked loop (PLL) has been used to generate a replica FM signal, this method has not been sufficiently improved as an interference canceller, because of the fundamental difference between FM signals and continuous waves. Next, as an interference canceller with very high performance, the Interference Cancelling Equalizer (ICE) was suggested for the PDC system, as shown in Fig. 2.6 [2.5]. It generates both a replica signal of the desired signal and a replica signal of the interference signal, which can cancel both ISI and CCI, respectively, with Maximum Likelihood Sequence Estimation (MLSE). The FMIC and ICE can generate a replica signal through the use of the fact that the interference signal is of a known modulation scheme. In contrast, an interference canceller that does not depend on the modulation scheme of the interference signal has been proposed, and it obtains a replica signal using a couple of antennas. Figure 2.7 shows the Vector Correlation Detection type Interference Canceller (VCDIC) [2.6]. The VCDIC can obtain a replica signal with an auxiliary antenna receiving the interference wave with the main antenna receiving the desired wave. Furthermore, the Extraction and Reinjection-type Interference Canceller (ERIC) was proposed as an interference canceller that can generate a replica signal even when a clear interference wave cannot be received using an auxiliary antenna [2.7]. As shown in Fig. 2.8, the signals received at two antennas, the main antenna and sub antenna, are controlled to adjust the amplitude and phase of the desired signal in one received signal to the same amplitude but reverse phase of the other desired signal. By adding both signals, the desired signal can be suppressed and the remaining interference signal can be obtained as a replica signal. Chapter 5 describes the performance estimation of the ERIC under fading conditions.

Apart from interference cancellers, modulation techniques that have an inherent interference compensation function are noted here. Spread-spectrum (SS) techniques are methods by which a signal generated with a particular bandwidth is spread in the frequency domain, resulting in a signal with a wider bandwidth [2.8]. An interference signal involved in the received signal is weakened in the inverse spread process at the demodulator. One method called direct sequence (DS) is employed in wireless LANs, IEEE802.11b. Another method called frequency hopping (FH) is employed in Bluetooth. Either communication system is operated in an unlicensed band in the 2.4 GHz band, which is called the industrial, scientific and medical (ISM) radio band. Communication devices

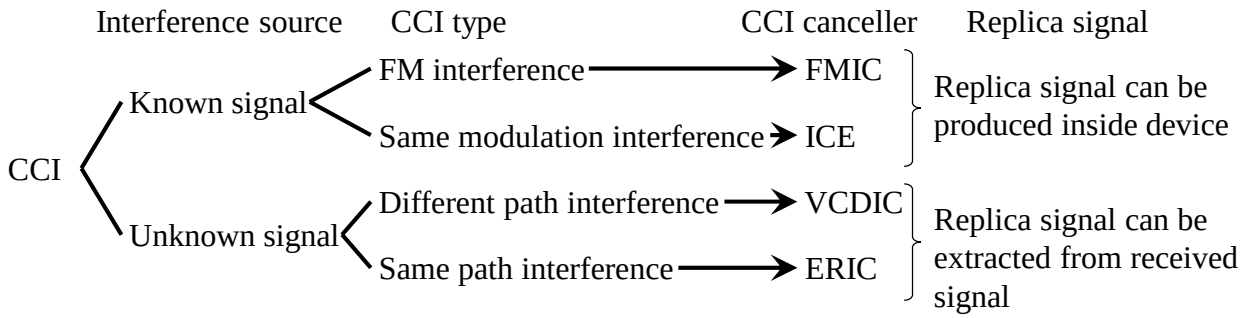

Fig. 2.4 CCI canceller classification.

operating in the ISM band must overcome any interference generated by ISM equipment. On the other hand, interleaving techniques are methods by which a signal is spread in the time domain. An interleaver combined with high-performance FEC is used for fixed microwave communication devices in order to recover the periodic degradation caused by radar interference [2.9].

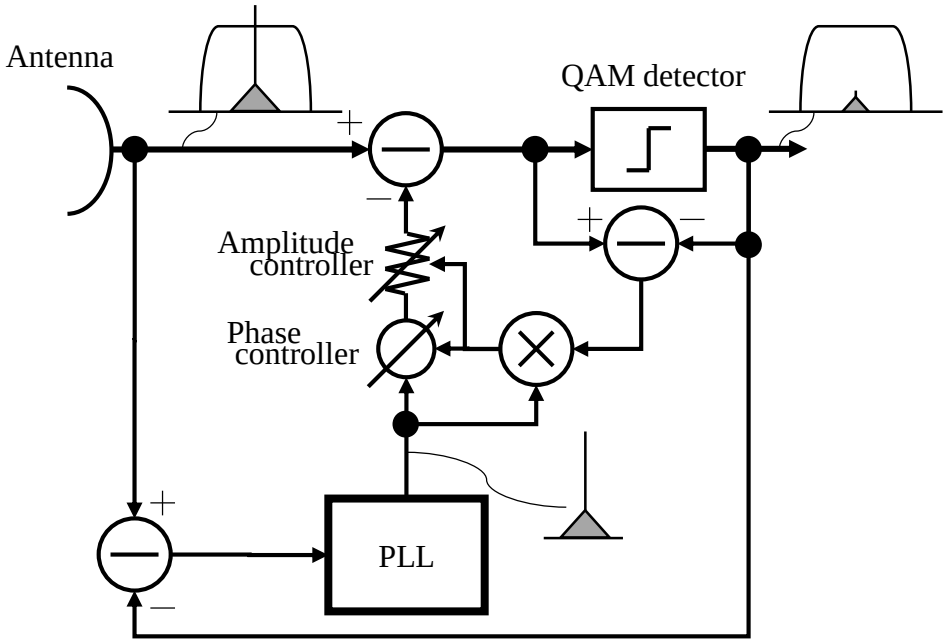

Fig. 2.5 FM interference canceller.

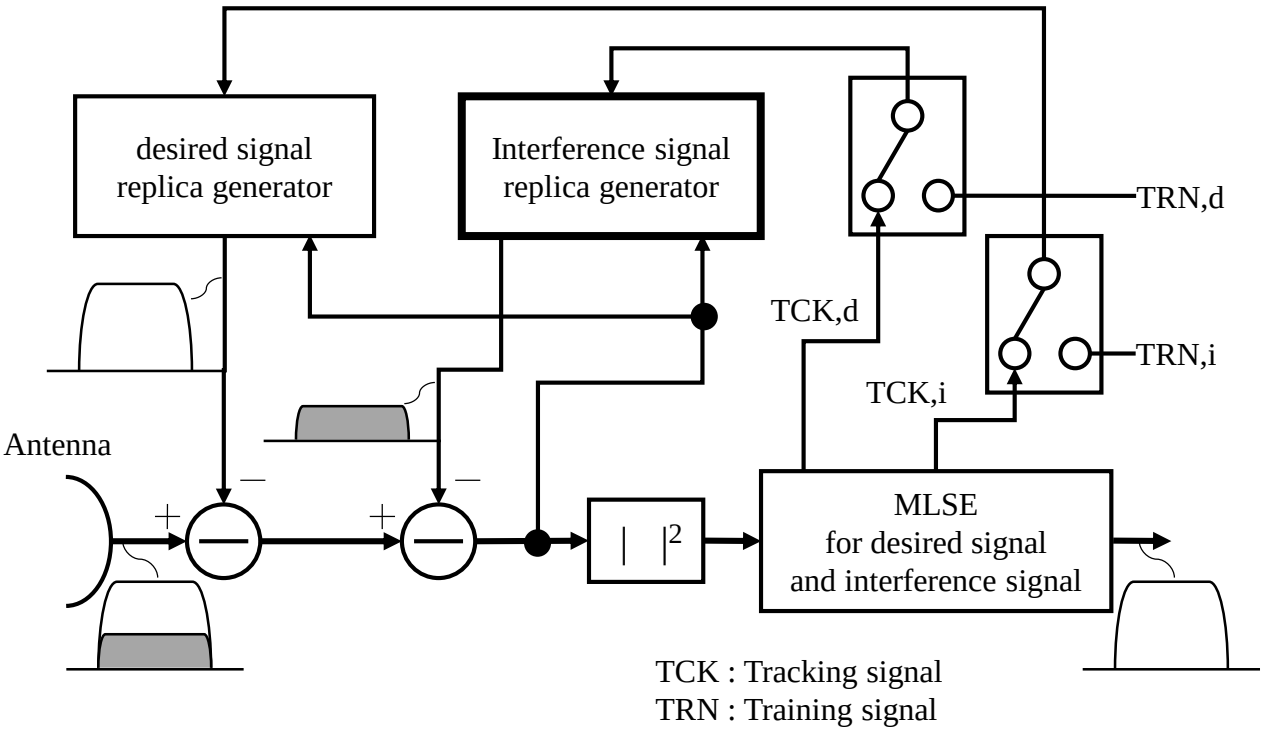

Fig. 2.6 Interference cancelling equalizer.

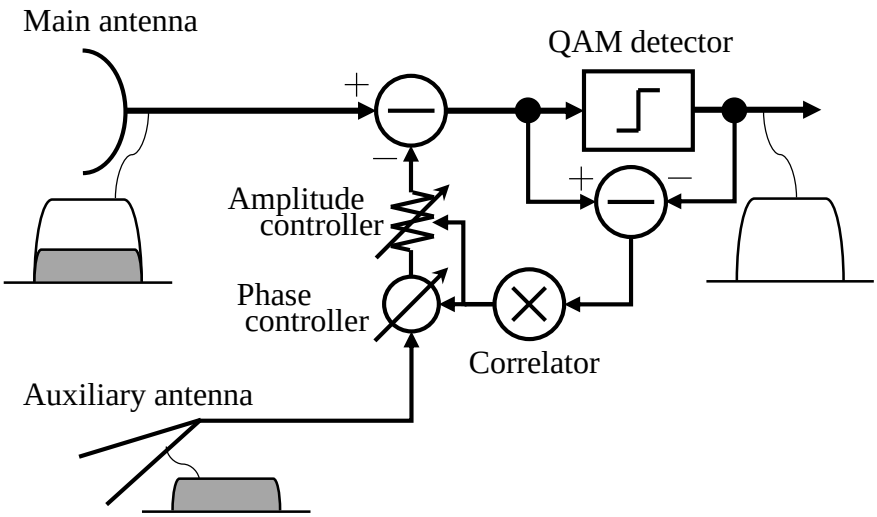

Fig. 2.7 Vector correlation detection type interference canceller.

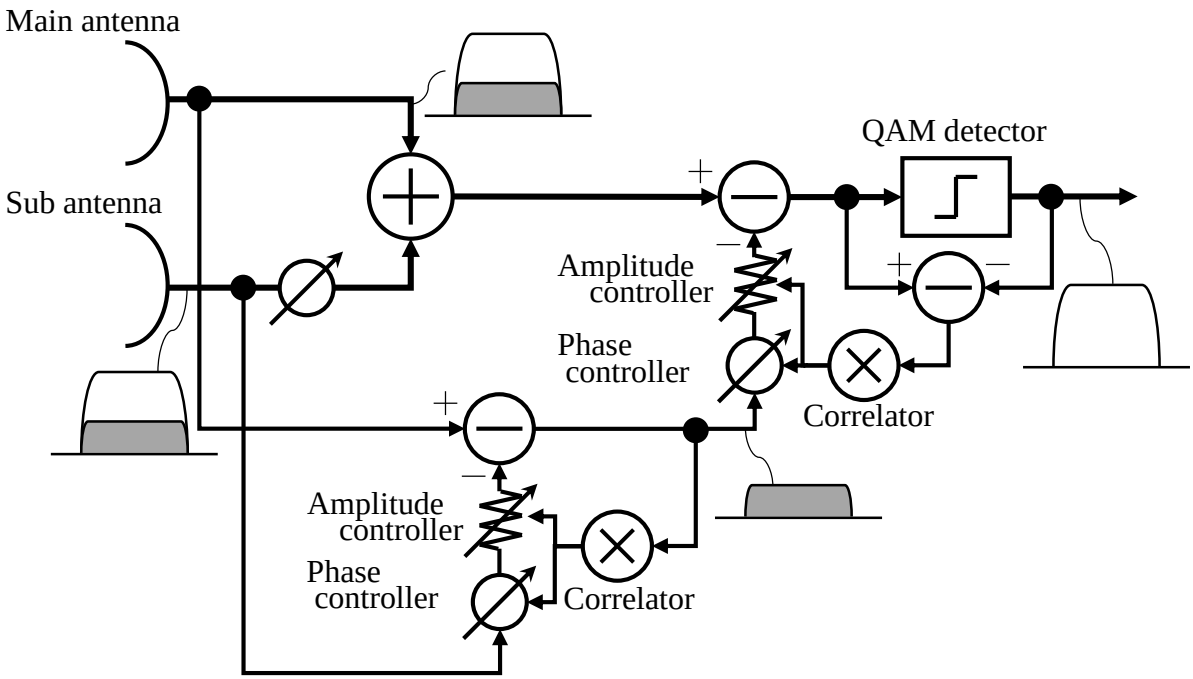

Fig. 2.8 Extraction and reinjection-type interference canceller.

2.3 Operating principle of OFDM transmission

This section describes the OFDM modulation scheme used in broadband wireless access systems [2.10]. In particular, the basic transmission technique necessary for the interference problems is discussed. The problem in broadband wireless transmission is that frequency selective fading due to multipaths deteriorates the transmission quality. As shown in Fig. 2.9, since many reflected waves are received, complicated frequency characteristics appear at the received signal. The received power spectra of a single carrier are shown in Fig. 2.10, and they have some valleys within the signal bandwidth. This deterioration is called frequency selective fading. The delay time profile is shown in Fig. 2.11. Each of the two measured locations is a relatively large indoor space in an exhibition hall. The delay spreads are 92 nsec and 149 nsec. Thus, in the case that a single carrier is applied to broadband transmission, a waveform equalizer is necessary to compensate for the deterioration in the transmission quality caused by the collapsed spectrum waveform. In contrast, in a multi-carrier case, because of a mere level decrease in each subcarrier, every carrier can be demodulated by individually increasing the carrier power level.

A basic block diagram of OFDM transmission which is a kind of multi-carrier transmission is shown in Fig. 2.12. The series of input data is input into the convolutional encoder and frequency interleaver, and they are mapped respectively at the mapping circuit on the signal constellation in Fig. 2.13. For example, for 16-QAM, every 4 bits of the series of input data are mapped to the complex number $d_k = a_k + jb_k$ (a_k, $b_k = \pm 1/\sqrt{10}$, $\pm 3/\sqrt{10}$) on the one point in the signal constellation. Next, these 48 points are input to the IFFT circuit, and the inverse fast Fourier transform of d_k is performed as the following equation,

$$x(n\Delta T) = \sum_{k=0}^{N-1} d_k \cdot \exp(j2\pi \frac{nk}{N}) \qquad (4.1).$$

This signal comprises 48 modulated signals of transmission data d_k and frequency $f_k = k/Ts$. Each modulated signal is called a subcarrier, and the frequency spacing becomes $1/Ts$. Term Ts is the length of an FFT block and sampling duration ΔT is Ts/N, where N (> 48) is the size of the FFT. Figure 2.14 shows the transmission spectrum waveform of the OFDM signal. The description regarding the pilot subcarriers for phase tracking is omitted. On the other hand, in the demodulation process the Fourier transform is performed at the FFT circuit, as the following equation,

$$d_k = \sum_{n=0}^{N-1} x(n\Delta T) \cdot \exp(-j2\pi \frac{nk}{N}) \qquad (4.2).$$

In this way, the transmission data are provided by demodulating each subcarrier orthogonally not to interfere with each other.

A guard interval is added to the output signal of the IFFT circuit of the transmitter. The guard interval of length Tg is part of the FFT block and it is added to the front of the FFT block of length Ts

with a cyclic nature. Then, the effect of the guard interval is shown in Fig. 2.15. Without the guard interval shown in Fig. 2.15(a), the wave mixed multipath suffers from ISI between the symbols. However, with the guard interval in Fig. 2.15(b), ISI is not included in the FFT block and the receiver can demodulate the signal without ISI by deleting the guard interval. The length of the guard interval is decided based on the delay time of the multipath in the assumed propagation environments. Chapter 6 describes a cell enhancer (CE), a radio repeater which is applied to achieve robustness in OFDM against ISI.

The fundamental OFDM transmission system combined with FEC is called coded OFDM (COFDM), and when it is combined with frequency interleaving it can well recover from frequency selective fading. Figure 2.16 shows a simplified example of frequency interleaving in the case of Depth = 4 and Length = 3. Consecutive errors occur by one notch on adjacent subcarriers due to frequency selective fading. However, when interleaving transmitted data in the frequency domain before IFFT processing at the transmitter and deinterleaving demodulated data after FFT processing at the receiver, these error data in succession can be considered separately. Convolutional coding and Viterbi decoding are used for FEC, and they have a high level of error correction ability to deal with random errors compared to a sequence of errors.

Next, coherent detection of an OFDM signal is briefly described. Figure 2.17 shows a burst format. There are two preset pattern signals at the beginning of each burst signal. One is a preamble signal that is used for automatic gain control (AGC), automatic frequency control (AFC), and timing synchronization, and the other is a training signal that is used for propagation channel estimation. First, the starting part of the preamble is operated for AGC, and the received signal power is adjusted to a fixed level. Second, AFC compensates for the phase shift during the repeated period of the preamble. Third, the symbol timing is decided from the peak timing of the correlation detection with the repeated pattern of the preamble. Fourth, the FFT processing divides the received training signal into subcarriers. By comparing them with the previously defined pattern, the distortion in the amplitude and phase due to multipath fading in the propagation channel are detected for each subcarrier. These quantitative evaluations of the distortion are used to equalize the subsequent data. Furthermore, tracking can be performed with not a training signal but the detection signal in order to continue equalizing the fluctuation in the propagation environment.

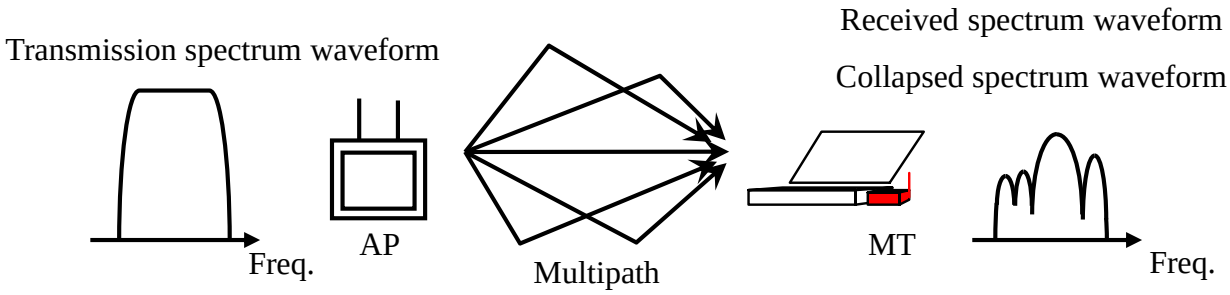

(a) Single carrier modulation

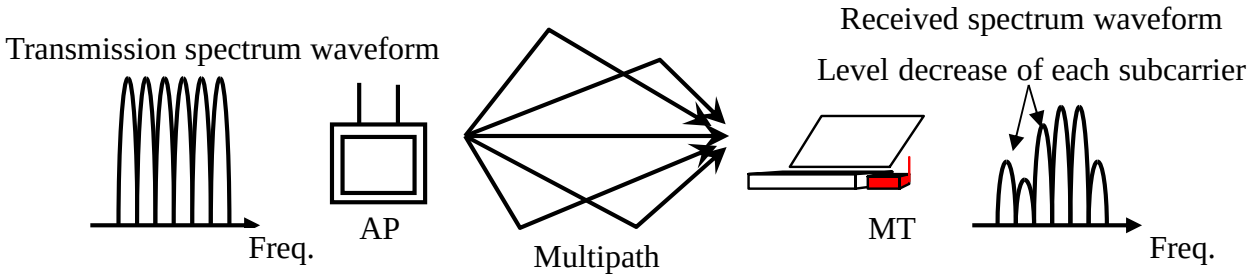

(b) Multi-carrier modulation

Fig. 2.9 Frequency selective fading induced deterioration in transmission quality due to multipaths.

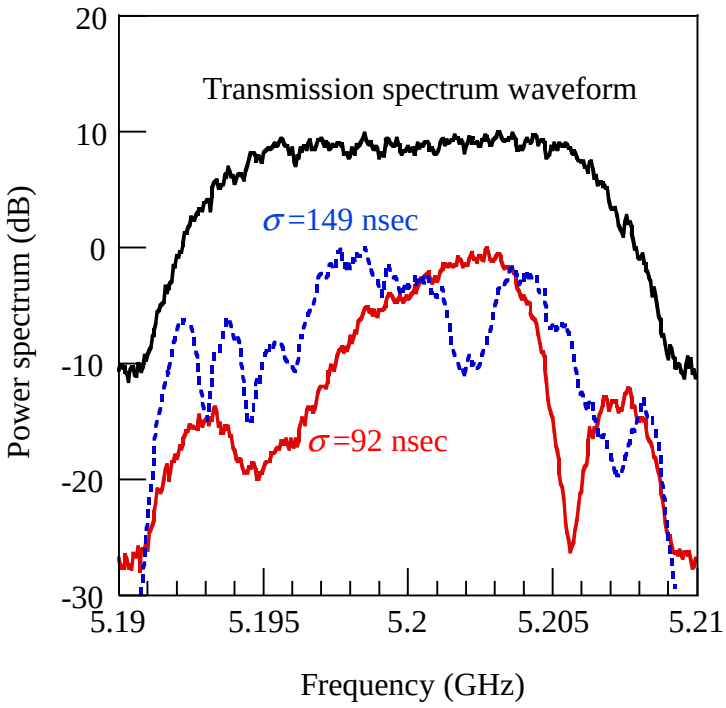

Fig. 2.10 Received power spectrum in real propagation channel.

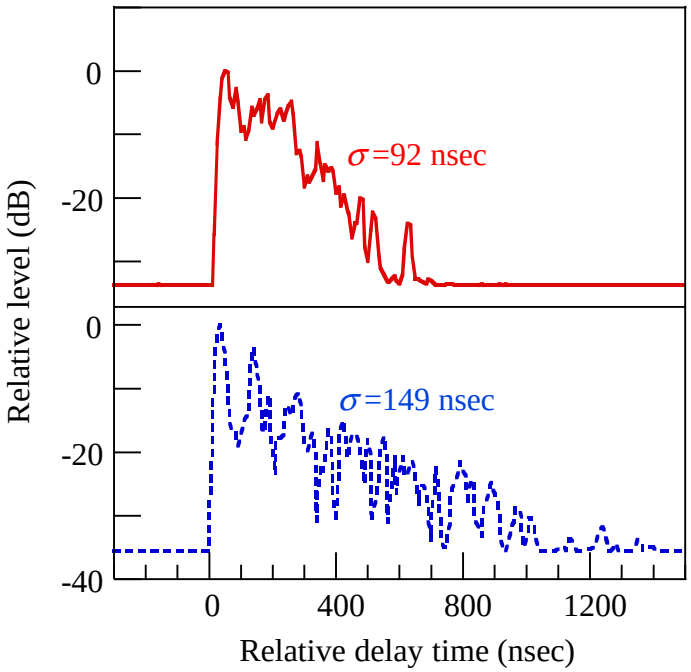

Fig. 2.11 Delay time profile in real propagation channel.

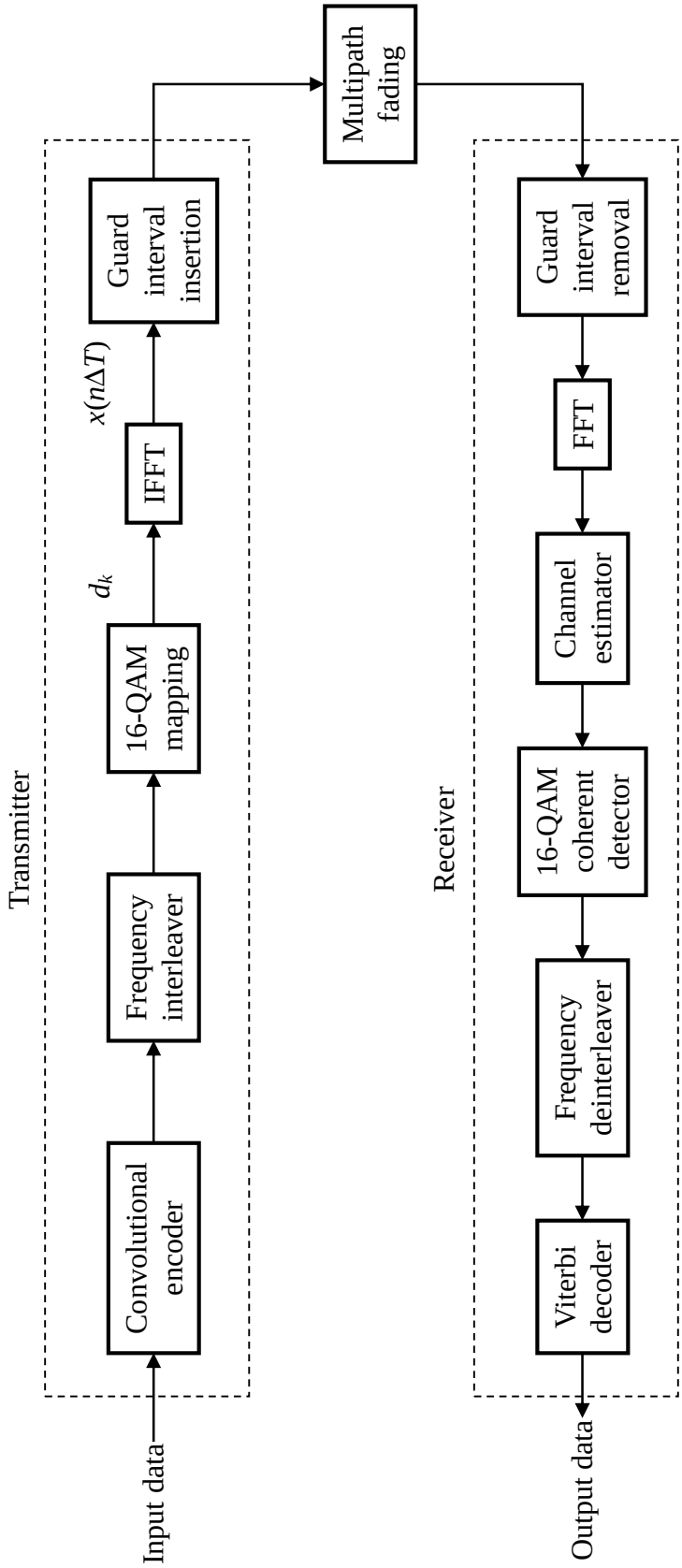

Fig. 2.12 Basic block diagram of OFDM transmission.

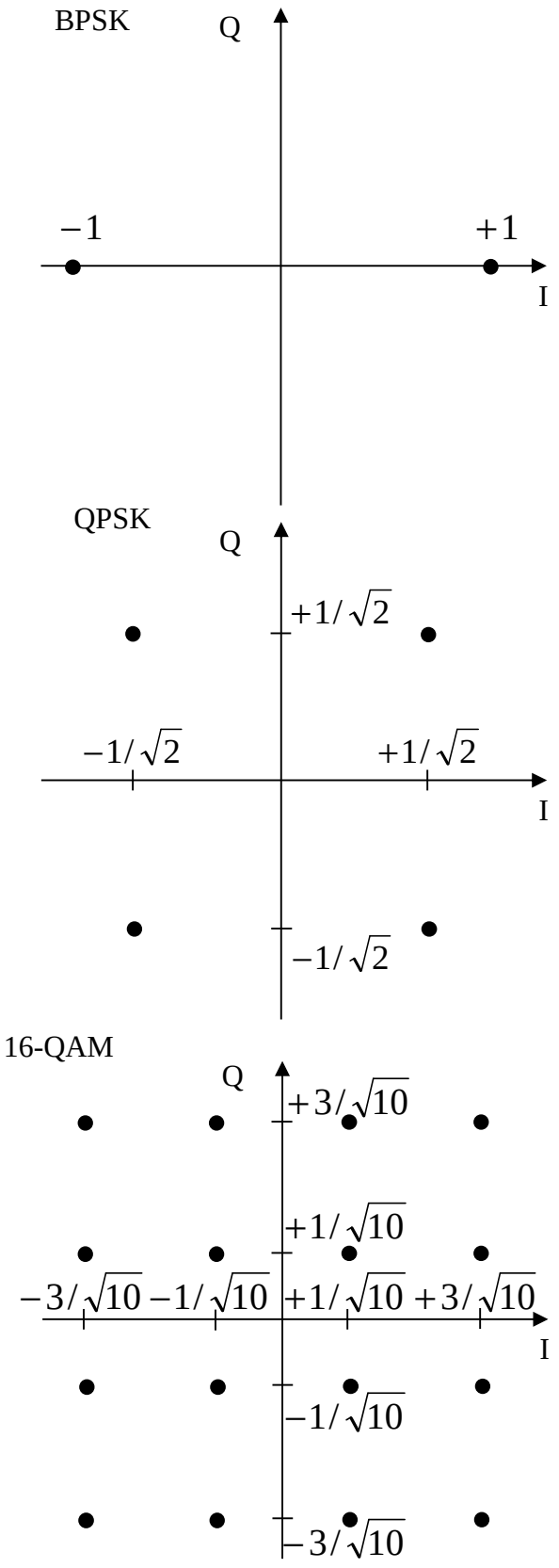

Fig. 2.13 Signal constellation.

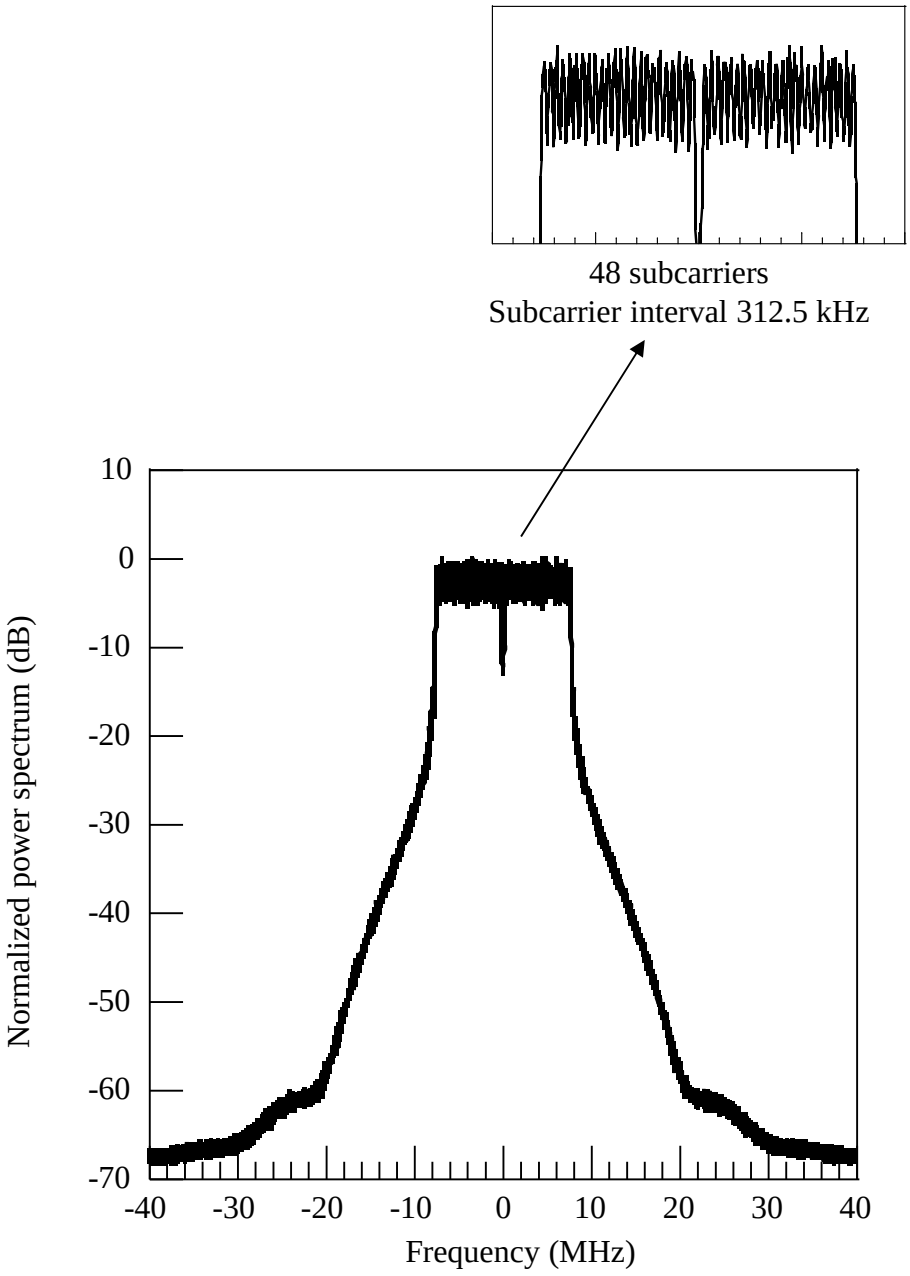

Fig. 2.14 Transmission spectrum waveform.

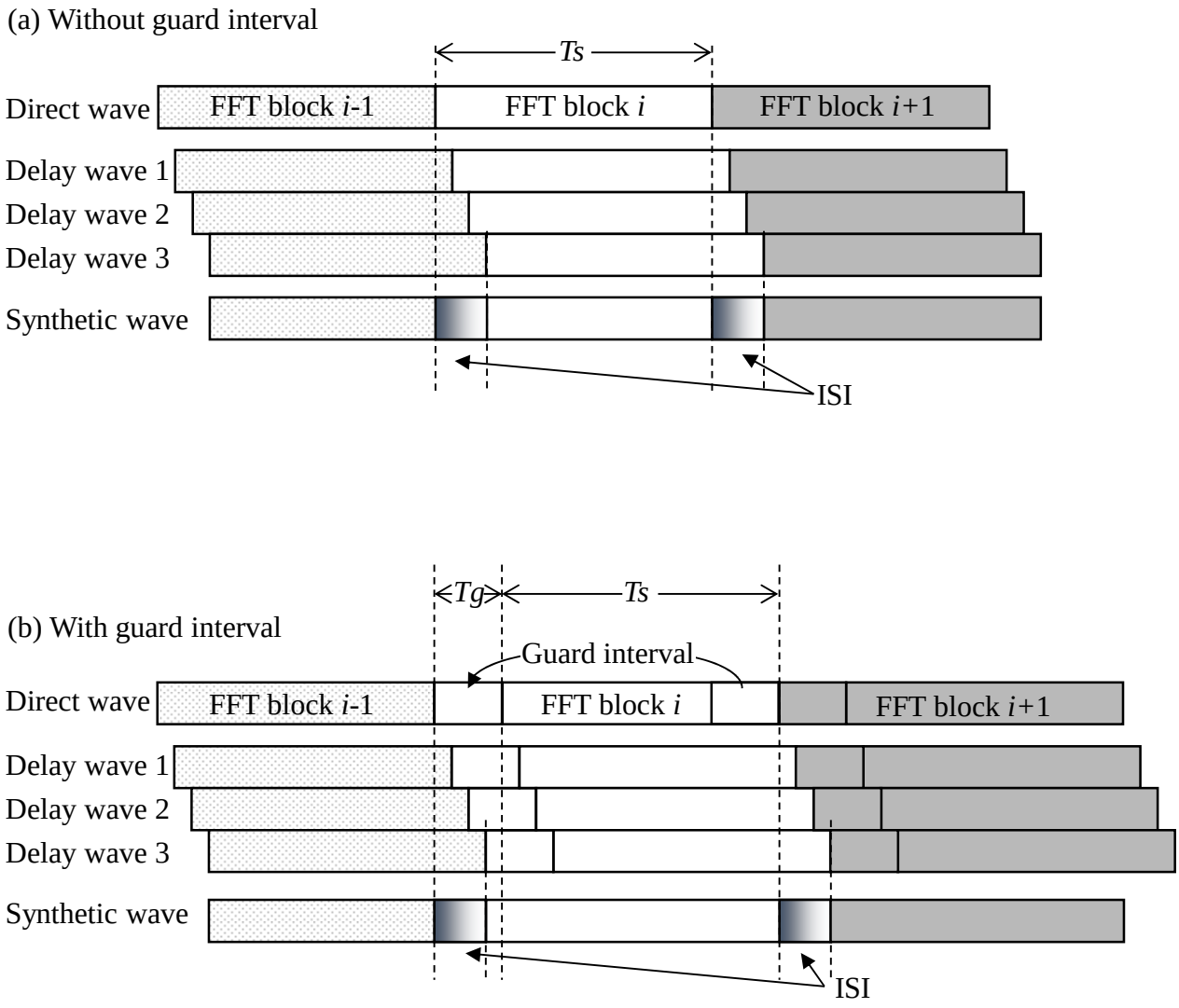

Fig. 2.15 Improvement effect of guard interval.

Fig. 2.16 Improvement effect of frequency interleaving.

Fig. 2.17 Burst format.

2.4 Multipath fading model and PER performance

Figure 2.18 shows an exponential delay profile model as a multipath fading model, which is employed under non-line-of–sight propagation conditions [2.11], [2.12]. Each path amplitude is independently fluctuated with a Rayleigh distribution, and the interval time between the delay waves is sampling time *T*. The average power of the nth delay wave is expressed as

$$Pn = (1 - \exp(-\Delta T / \sigma)) \cdot \exp(-n \cdot \Delta T / \sigma) \qquad n = 0,1,2,\cdots \qquad (4.3),$$

where σ is a parameter of the delay spread. The summation of the average power is normalized to 1. In this way, in the multipath fading model, the average power is *Pn*, the amplitude is Rayleigh distributed, and the phase is changed from 0 to 2π at random.

Figure 2.19 shows another multipath fading model when there is a stable direct wave. This is a synthetic wave that combines the direct wave with Rayleigh distributed multipath waves as shown in Fig. 2.18. The amplitude distribution is called a Rician distribution. The power ratio of the direct wave to the Rayleigh waves is referred to as the *k* factor. The normalization factor 1/(*k* +1) is multiplied by the direct wave and each delay wave so that the average power of the synthetic wave becomes 1. The delay spread, which changes by involving the direct wave, is expressed in the equation below, and it becomes smaller than delay spread σ without a direct wave.

$$\sigma' = \frac{\sqrt{2k+1}}{k+1}\sigma \qquad (4.4).$$

Then, the transmission performance in multipath fading environments is shown. Table 2.1 shows the main parameters for the simulation. The modulation scheme is 16-QAM, the coding rate is R = 3/4, and the transmission speed is 36 Mbps. The packet error rates (PERs) for the packet length of 54 bytes are analyzed. The PER performance in the case of multipath Rayleigh fading is shown in Fig. 2.20, which is calculated using delay spread σ as a parameter. The PER performance is the best for σ = 150 nsec. Figure 2.21 shows the relation of the delay spread for the PER performance when C/N = 22 dB. In the case of a large delay spread, the delay waves whose delay times are longer than the guard interval become ISI, and the PER performance is affected by the ISI. On the other hand, the PER performance deteriorates even when the delay spread is small. In this case, frequency selective fading approaches flat fading, and the number of subcarriers in which the power drops at the same time increases. The probability that the number of successive errors exceeds the depth of the frequency interleaving becomes higher, and because the errors cannot be scattered at random, the error correction capability is weakened.

The PER performance in the case of multipath Rician fading is shown in Fig. 2.22, which is calculated with the *k* factor of 3, 6, and 10 dB and delay spread σ' of 75, 60, and 42 nsec corresponding to delay spread σ of 100 ns in Eq. (4.4). It is apparent that the PER performance in the case of the Rician distribution improves beyond the PER performance in the case of a Rayleigh distribution. As the *k* factor becomes large, the PER performance improves and approaches the PER performance of an Additive White Gaussian Noise (AWGN) channel without multipath fading.

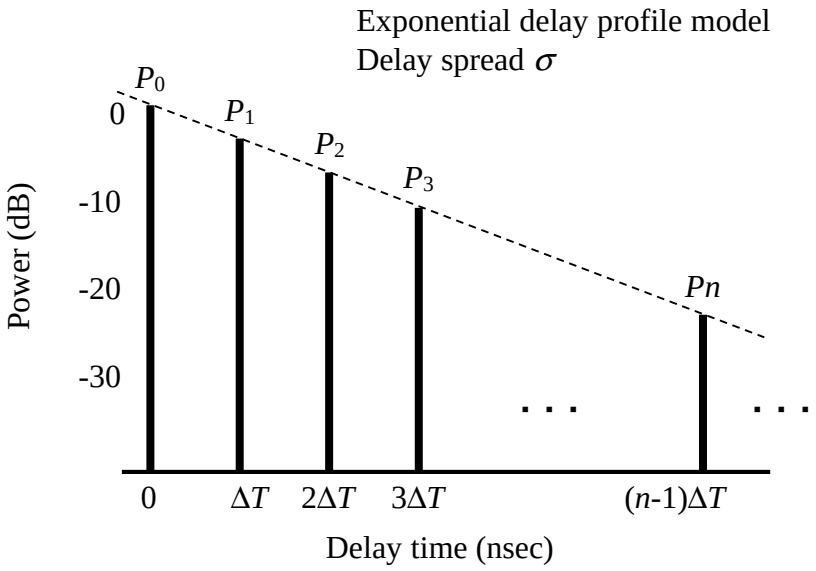

Fig. 2.18 Rayleigh multipath fading model.

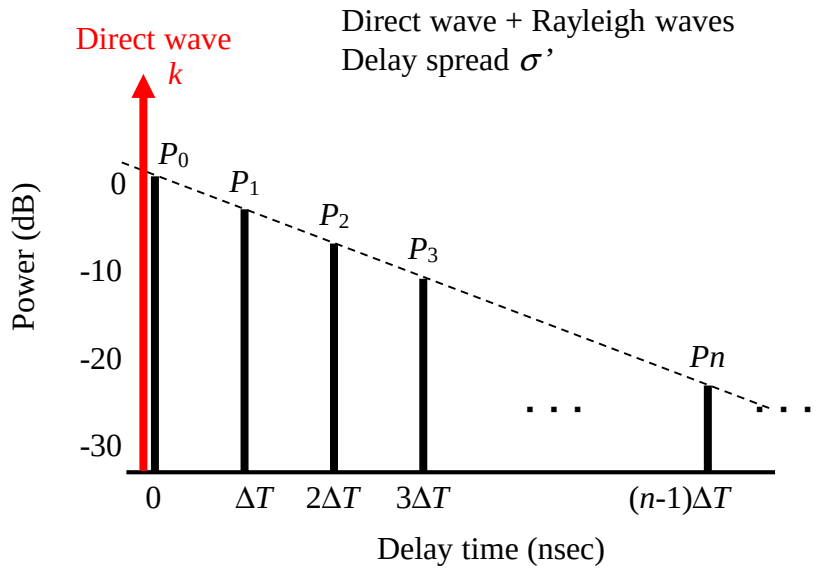

Fig. 2.19 Rician multipath fading model.

Table 2.1 Main parameters.

Modulation scheme	16QAM-COFDM
Demodulation method	Coherent detection
Coding rate	3/4
Transmission speed	36 Mbps
Packet length	54 bytes
Number of subcarriers	48
Subcarrier interval	312.5 kHz
FFT block length	3.2 μsec
Guard interval length	0.8 μsec
FFT size	64 points
Symbol rate	20 MHz
Multipath fading model	Rayleigh distribution Rice distribution

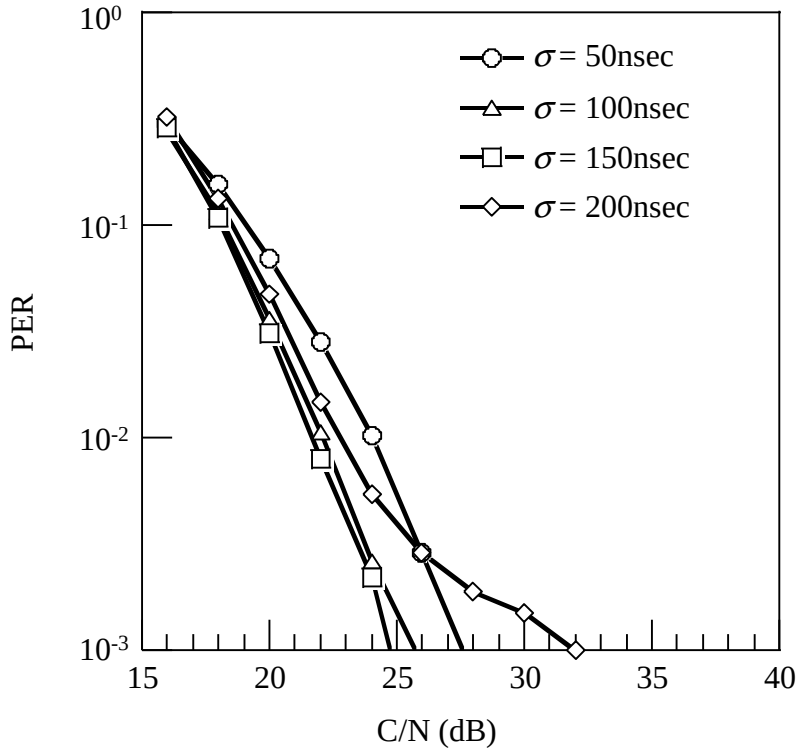

Fig. 2.20 PER performance using Rayleigh multipath fading model.

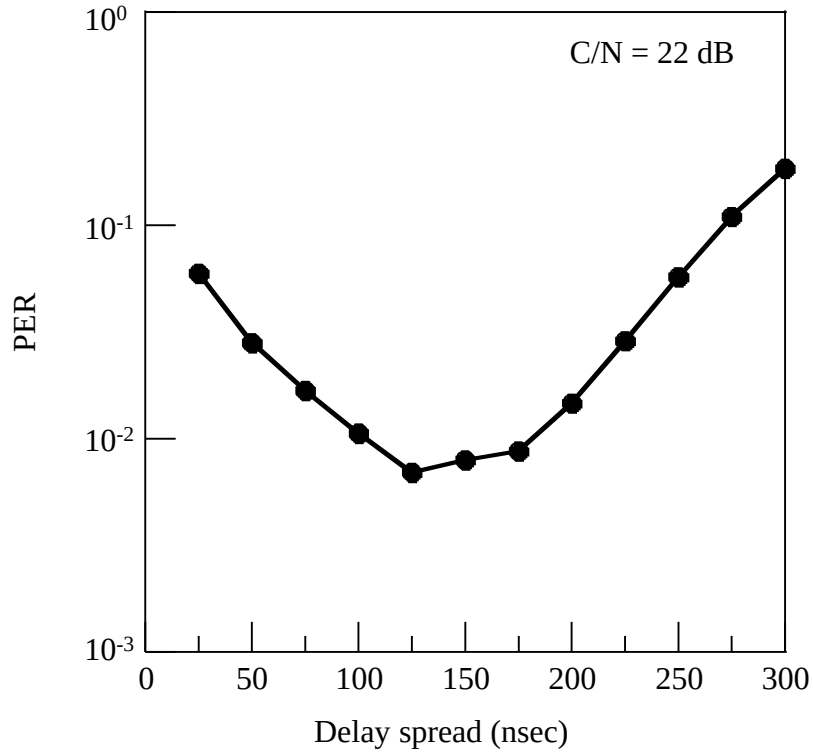

Fig. 2.21 PER vs. delay spread.

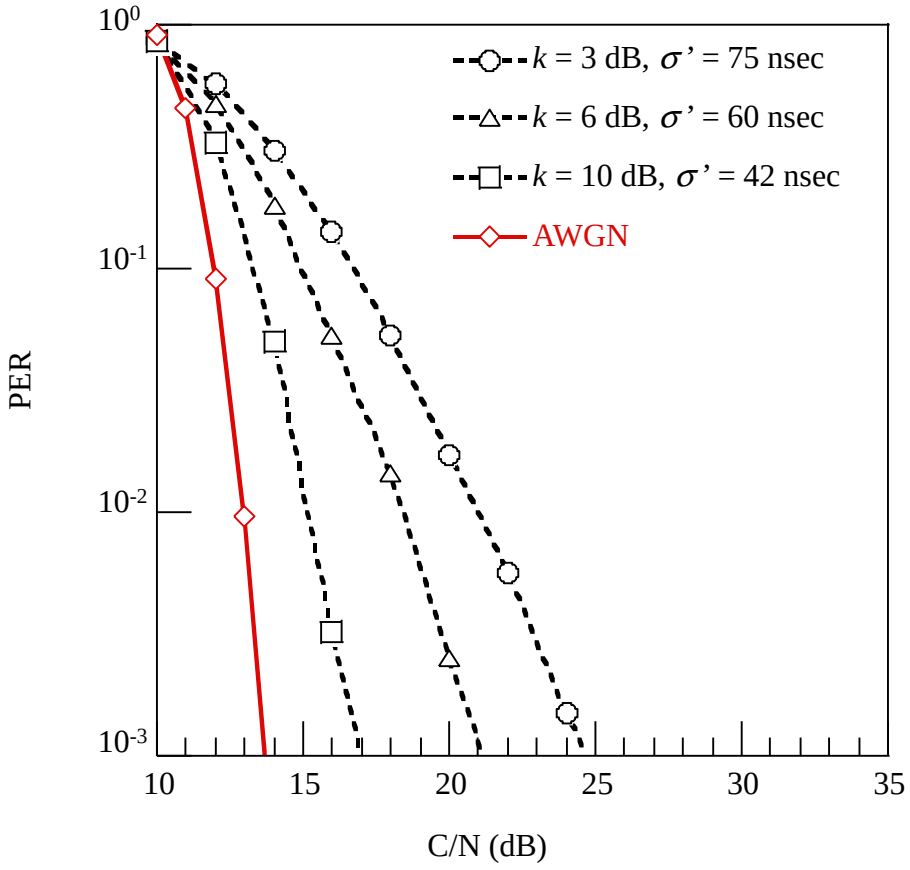

Fig. 2.22 PER performance using Rician multipath fading model.

References for chapter 2

[2.1] N. Pothecary, “Feedforward Linear Power Amplifier,” Artech House, Boston, London, 1999.

[2.2] T. Matsuoka, et al, “Compensation of Nonlinear Distortion during Transmission Based on the Adaptive Predistortion Method,” IEICE Trans. Electron., vol. E80-C, No. 6, pp.782-787, June 1997.

[2.3] T. Horiuchi, W. Yang, T. Ohtsuki and I. Sasase, “Performance evaluation of OFDM with a nonlinear distortion compensation technique using partial transmit sequence and predistortion,” IEICE Trans. Commun., vol. J85-B, No. 11, pp.1865-1873, Nov. 2002.

[2.4] J. Namiki, “FM Interference Elimination Systems for Digital Microwave Transmission,” IEICE Trans. Commun., vol. J64-B, No. 6, pp.505-512, June 1981.

[2.5] H. Yoshino and H. Suzuki, “Experimental Evaluation of Interference Canceling Equalizer (ICE) for a TDMA Mobile Communication,” IEICE Trans. Commun., vol. E84-B, No. 2, pp.228-237, Feb. 2001.

[2.6] H. Matsue and T. Murase, “Vector Correlation Detection Type Interference Canceller,” IEEE GCOM’87, vol.1, pp. 1233-1238, Nov. 1987.

[2.7] K. Watanabe, H. Matsue, and T. Murase, “Extraction and Reinjection-type Interference Canceller,” IEICE Trans. Commun., vol. J74-B-II, No. 9, pp.469-478, Sept. 1991.

[2.8] M. K. Simon, J. K. Omura, R. A. Scholtz and B. K. Levitt, “Spread spectrum communication handbook,” McGraw-Hill, 1994.

[2.9] S. Aikawa, T. Okuno, R. Ohmoto and M. Hatai, “Bit Interleaving Technique as a Radar Interference Canceler in Digital Microwave Radio Systems,” IEEE ICC'92, vol.3, pp.1482-1486, June 1992.

[2.10] R. van Nee and R. Prasad, “OFDM for Wireless Multimedia Communications,” Artech House Publishers, 2000.

[2.11] Rec. ITU-R P.1238-7, “Propagation data and prediction methods for the planning of indoor radiocommunication systems and radio local area networks in the frequency range 900 MHz to 100 GHz,” ITU-R recommendations, P Series, 2012.

[2.12] J. G. Proakis, “Digital Communications,” Third Edition, ch14, pp.795-797, McGraw-Hill, 1995.

Chapter 3

Linearized Constant Peak-Power Coded OFDM Transmission for Broadband Wireless Access Systems

3. Linearized Constant Peak-Power Coded OFDM Transmission for Broadband Wireless Access Systems

3.1 Introduction

OFDM is a suitable modulation technique for broadband wireless access systems because of its excellent robustness against frequency-selective fading [3.1], [3.2]. However, OFDM signals can suffer from intermodulation distortion among the subcarriers caused by the nonlinearity of the high-power amplifier (HPA) in the transmitter. This nonlinear distortion degrades own transmission quality, and since it causes the spectrum to expand significantly, the resulting out-of-band emission interferes with adjacent channels in the frequency band assigned to the specific system. In addition, the out-of-band emission becomes interference to other systems that use adjacent radio frequency bands. To illustrate this, in the 5-GHz band, interference to various radar systems and satellite communication systems that use 5-GHz feeder links must be considered as discussed in the ongoing standardization process [3.3]. As an example, when the number of subcarriers is 52 as standardized in some 5-GHz band systems [3.4], a peak-to-average power ratio (PAPR) ranges up to 17.16 dB. Thus, without any remedies, the power amplifier must operate with rather large backoff levels to alleviate the interference at the cost of power efficiency; otherwise, an excessively wide frequency guard-band must be placed between the systems.

To reduce the PAPR of OFDM signals, several techniques have been proposed such as clipping [3.5], complementary coding [3.6], two-branch combining [3.7]. On the other hand, predistorters can be effective in compensating nonlinear distortion. Over the past few years, experimental results of employing predistortion based on digital baseband processing have been reported [3.8]–[3.10]. Specifically, these papers reveal that a significant improvement is obtained by using the adaptive predistortion method with the addition of a feedback control loop. Furthermore, some applications of the predistortion method to OFDM signals have been examined [3.11], [3.12]. These nonlinear distortion compensation techniques can enhance their capability if they are combined with the PAPR reduction technique. However, to date, no feasible method for mobile radio equipment has been reported in this respect, though the out-of-band spectrum suppression is of great interest in practice.

Given the above facts, this paper proposes a nonlinear distortion compensation technique for OFDM signals. It incorporates a baseband predistortion with a constant peak-power OFDM (CP-OFDM) [3.13], which can reduce the PAPR while maintaining the linearity of the IFFT outputs. Its operating principle is described in Section 3.2. The out-of-band spectrum suppression offered by the proposed technique is investigated by a simulation using the model of a typical class-AB amplifier, and its performance is verified with experimental results in Section 3.3. Section 3.4 confirms that the transmission characteristic of the proposed technique is enhanced with bit interleaving, and verifies the validity of using the linearizer in terms of increased system capacity. Finally Section 3.5 concludes this chapter.

3.2 Operating Principle of the Proposed Nonlinear Distortion Compensation Technique

3.2.1 Overall Configuration

A block diagram of the baseband-equivalent system for the proposed OFDM transmission system is shown in Fig. 3.1. A constant peak-power circuit and baseband predistorter are added to an ordinary OFDM configuration. The constant peak-power circuit and the baseband predistorter are described in detail in the following sections.

This chapter adopts the related system parameters from 5-GHz-oriented specifications (for example, see [3.4]) as a practical example. Thus, convolutional codes incorporated with interleaving (see Fig. 3.1), are used for forward error correction (FEC). As the first modulation scheme, 16 quadrature amplitude modulation (16-QAM) is applied.

3.2.2 Constant Peak-Power Circuit

A block diagram of the constant peak-power circuit is shown in Fig. 3.2. The envelope peak, U_{pk}, of the IFFT output is detected at the block-by-block envelope peak detection circuit as follows:

$$U_{pk} = \mathrm{Max}\ [\ |u(k)|,\ k = 0,..., N_{FFT} - 1\ ]\ , \tag{3.1}$$

where $u(k)$ is the IFFT output and N_{FFT} is the FFT size. Next, the envelope amplitude of the input signals is reduced over the corresponding block and amplitude-reduced signals, $v(k)$, are yielded as

$$v(k) = u(k)\ A_{cp} / U_{pk}\ . \tag{3.2}$$

After this envelope-peak reduction process, envelope peak U_{pk}, of $v(k)$ is consequently changed to constant value, A_{cp}. This technique maintains the linearity of the IFFT outputs.

3.2.3 Baseband Predistorter

A block diagram of the baseband predistorter is shown in Fig. 3.3. At first the amplitude of the input baseband signal, (I_{in}, Q_{in}), is calculated as r. Amplitude r corresponds to an address of the table, and the complex coefficient, (C_i, C_q), is referred to from this table. Signal (I_{in}, Q_{in}) goes through complex multiplication with (C_i, C_q). As a result, signal (I_{out}, Q_{out}) possesses the inverse characteristics of the nonlinear distortion. If the AM-AM distortion and the AM-PM distortion of the target HPA are represented as $A(r)$, $\phi(r)$ respectively, the complex coefficient, (C_i, C_q), is calculated as follows:

$$C_i = A^{-1}(r) \cos[\ -\phi(A^{-1}(r))] / r \tag{3.3a}$$

$$C_q = A^{-1}(r) \sin[\ -\phi(A^{-1}(r))] / r \tag{3.3b}$$

where $A^{-1}(r)$ is the inverse characteristic of $A(r)$.

Next, the operating principle of the proposed nonlinear distortion compensation technique is explained. Figure 3.4 shows the nonlinear characteristics of the HPA, that is, $A(r)$, normalized by the saturation point; the gain is 1. The predistortion characteristic can be expressed by a curve

symmetrical to that of the nonlinear characteristics inverted around x = y, which is the same as the inverse characteristic, $A^{-1}(r)$. By multiplying the predistortion characteristic beforehand and providing the nonlinear distortion with the HPA later, the final characteristic becomes linearized. However, obviously from this figure, the input signal into the predistorter is limited to less than 1. OFDM signals with large PAPR readily exceed this upper limit. However, by integrating the above-mentioned CP-OFDM, this problem can be solved. That is to say, the CP-OFDM holds the peak of the signal amplitude to A_{cp} (≤ 1). Therefore, the input amplitude can be kept within the input range of the predistorter.

In this chapter, hereafter, the predistorter with constant peak-power circuit is simply referred to as the linearizer, and the OFDM transmission technique using the linearizer is referred to as the linearized constant peak-power (LCP)-COFDM. Its performance is investigated and compared with that of conventional Coded OFDM transmission (COFDM).

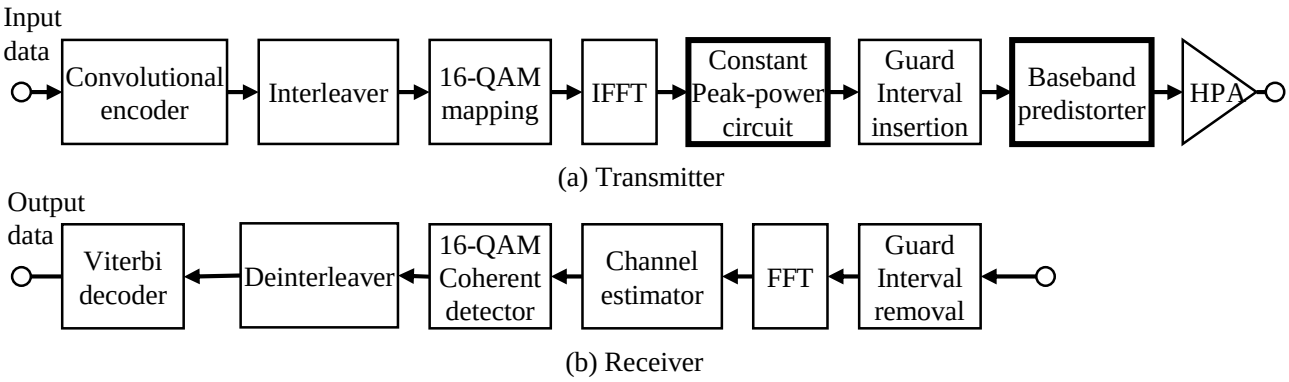

Fig. 3.1 Overall configuration of baseband-equivalent system for proposed OFDM transmission system.

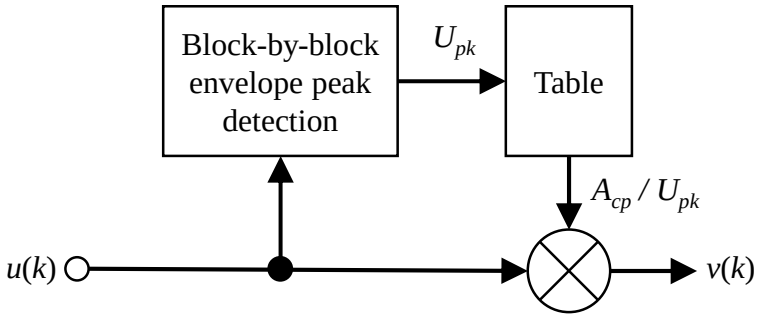

Fig. 3.2 Block diagram of constant peak-power circuit.

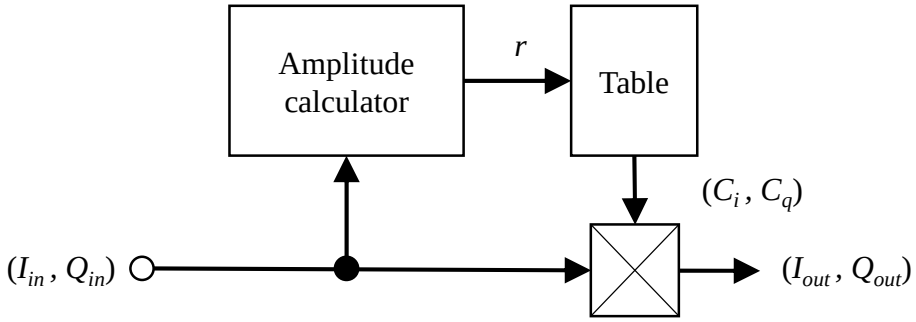

Fig. 3.3 Block diagram of baseband predistorter.

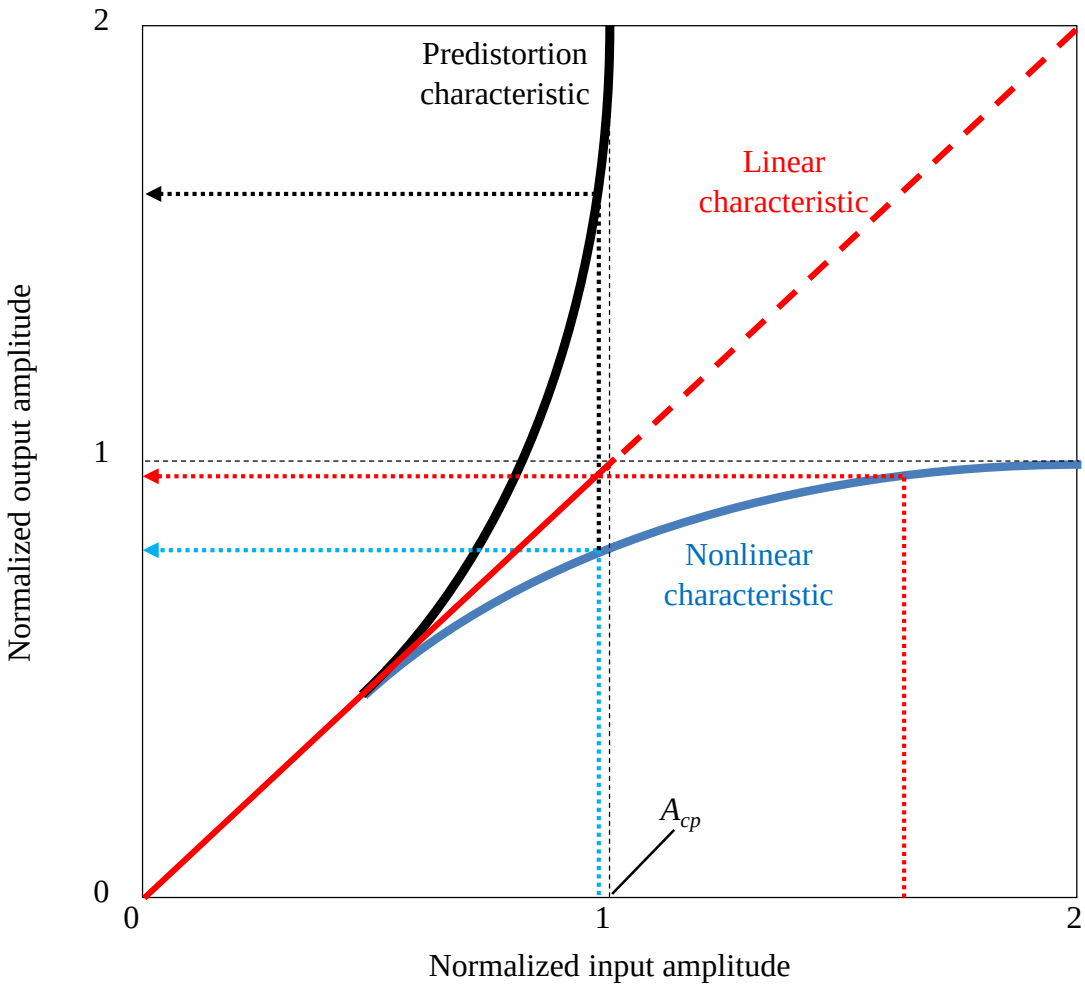

Fig. 3.4 Model of input and output amplitude characteristics.

3.3 Fundamental Verification of Nonlinear Distortion Compensation

3.3.1 Main parameters

The main parameters used in the simulation, listed in Table 3.1, are based on discussions and decisions in standardization bodies such as ETSI-BRAN, MMAC in Japan and IEEE 802.11 in the USA. The number of subcarriers is 52 including 4 pilot subcarriers in addition to 48 data subcarriers. The subcarrier frequency spacing is 0.3125 MHz. Since the center subcarrier is set to a null to avoid the influence of DC offset [3.4], the bandwidth of all 53 subcarriers (OFDM-bandwidth) is 16.5625 MHz. When a 64-point IFFT is used, the sampling rate after the guard interval insertion is 20 MHz (= 0.3125 MHz*64).

The simulation considers a model of an amplifier proposed as a typical class-AB amplifier in ETSI-BRAN [3.14]. This model is based on the measurements of RF Micro Device amplifier RF2146 and is expressed by the following equations,

$$u_{out} = M(|u_{in}|) \exp\{\boldsymbol{j} \arg[u_{in}]\} \tag{3.4}$$

$$M(|u_{in}|) = [c_1|u_{in}| + c_3|u_{in}|^3 + c_5|u_{in}|^5 + c_7|u_{in}|^7 + c_9|u_{in}|^9] * [1 - k_1 \exp(-k_2|u_{in}|)] \quad \text{for } |u_{in}| < 1.4294$$

$$= 0.9896 \angle -104.5387^\circ \quad \text{for } |u_{in}| > 1.4294, \tag{3.5}$$

where $c_1 ... c_9$, k_1, and k_2 are the model coefficients from Table 3.2. Furthermore, the predistortion characteristic for this amplifier is obtained as the 9-th polynomial approximation. Note that I assume that only the HPA has nonlinear characteristics.

3.3.2 Simulation Results

First of all, the distribution of the envelope peak, U_{pk}, of the IFFT output is investigated. The results are shown in Fig. 3.5 where the power of each subcarrier is normalized as 1. It has been already shown that the distribution in Fig. 3.5 can empirically be fitted using the beta-distribution written as the following function of α and β [3.13]:

$$P_d(U_{pk}) = \frac{(\alpha+\beta+1)!}{\alpha!\beta!}\left(\frac{U_{pk} - A_{\min}}{A_{\max} - A_{\min}}\right)^{\alpha}\left(\frac{A_{\max} - U_{pk}}{A_{\max} - A_{\min}}\right)^{\beta}, \tag{3.6}$$

where $A_{\max}$ is the maximum peak amplitude, and $A_{\min}$ is the minimum peak amplitude. The beta-distribution with α = 4 and β = 39 shows good agreement with the simulation results. By applying the CP-OFDM technique, the signal power changes according to parameter A_{cp} from Eq. (3.2). The output power of the CP-OFDM, P_{cp} can be expressed by the following equation,

$$P_{cp} = 10 \log [A_{cp}^2 N_{sc} / \overline{U_{pk}^2}], \tag{3.7}$$

where N_{sc} denotes the number of subcarriers and $\overline{U_{pk}^2}$ represents the averaged power. The relationship between A_{cp} and the output power normalized at the saturation point is shown in Fig. 3.6; the saturation point is normalized to 0 dB. The simulation results well agree with the ones obtained from Eq. (3.7).

From the above results, the output power P_{cp} increases with A_{cp}. On the other hand, it is clear from Fig. 3.4 that A_{cp} must be 1 or less for LCP-COFDM to ensure linearity. When A_{cp} = 1.0, LCP-COFDM yields an output power of -7.3 dB (N_{sc} / $\overline{U_{pk}^{\ 2}}$ = 52/274).

Based on this result, the power spectrum of LCP-COFDM is compared to the case of the output backoff (OBO) = 7.3 dB without employing the linearizer. The simulation results are depicted in Fig. 3.7. I also confirmed by simulation that, when only the constant peak-power circuit is employed is almost equal to that of COFDM with OBO = 7.3 dB. Conversely when only the predistorter is applied without the constant peak-power circuit, it is impossible to completely eliminate the nonlinear distortion for the reason mentioned in subsection 3.2.3. If it is assumed that the channel spacing (CSP) equals 20 MHz in Fig. 3.7, the radiation power at the adjacent channel is improved by approximately 12 dB when using the linearizer. In addition, the adjacent channel interference (ACI) power ratio calculated by using the OFDM-bandwidth is shown in Fig. 3.8. It is obvious that LCP-COFDM significantly reduces the out of band interference. As an example, at the center of the adjacent channels, it improves ACI by approximately 13 dB when compared with COFDM with OBO = 7 dB. In order to suppress the out-of-band emission that extends to the adjacent channel, the broadband signal must be result at the baseband predistorter with a sampling rate four time or more that of the guard interval insertion, 20 MHz, to avoid the influence of aliasing noise. Note that it is not necessary to use four fold FFT; LCP-COFDM offers lower processing speed requirements if a technique such as interpolation filtering is used.

3.3.3 Experimental Results

This subsection describes the experimental results gained using a commercially available HPA, a C-band power GaAs FET (NEZ4450-4DD). A block diagram of the LCP-COFDM used in the experiments is shown in Fig. 3.9. Note that the baseband signals in LCP-COFDM were calculated by computer. The RF center frequency was tuned to 5.2 GHz and a scale model operating at a quarter of the specified sampling frequency was used due to the limited processing speed of the experimental equipment.

Figure 3.10 shows the power spectrum of COFDM and Fig. 3.11 shows the power spectrum of LCP-COFDM. Their output powers were set to equal each other. When the CSP is 5 MHz, the radiation power in an adjacent channel is improved by about 10 dB when employing the linearizer; improvement in terms of ACI is approximately 10-dB. It should be mentioned that the noise floor of LCP-COFDM increases due to imperfection in modeling the amplifier. If necessary, this a smaller value of A_{cp} can be used at the cost of the resulting OBO.

Table 3.1 Main parameters.

Data rate	24 Mbps
Modulation	16-QAM-OFDM
Coding rate	1/2
Number of subcarriers	52 (including 4 pilots)
Subcarrier frequency spacing	0.3125 MHz
OFDM-bandwidth	16.5625 MHz
FFT size	64 points
Guard interval (GI)	16 points
Sampling rate of GI insertion	20 MHz
Packet length	64 bytes
Amplifier	Class-AB model
Multipath fading	Exponential decaying Rayleigh fading (τ_{rms} = 150 nsec)

Table 3.2 Model coefficients for class-AB amplifier.

Coefficient	Value
c_1	-0.00650 –j 1.0014
c_3	0.5951 –j 0.1062
c_5	-0.9624 +j 0.3565
c_7	0.4304 –j 0.1390
c_9	-0.0561 +j 0.0141
k_1	0.1
K_2	9

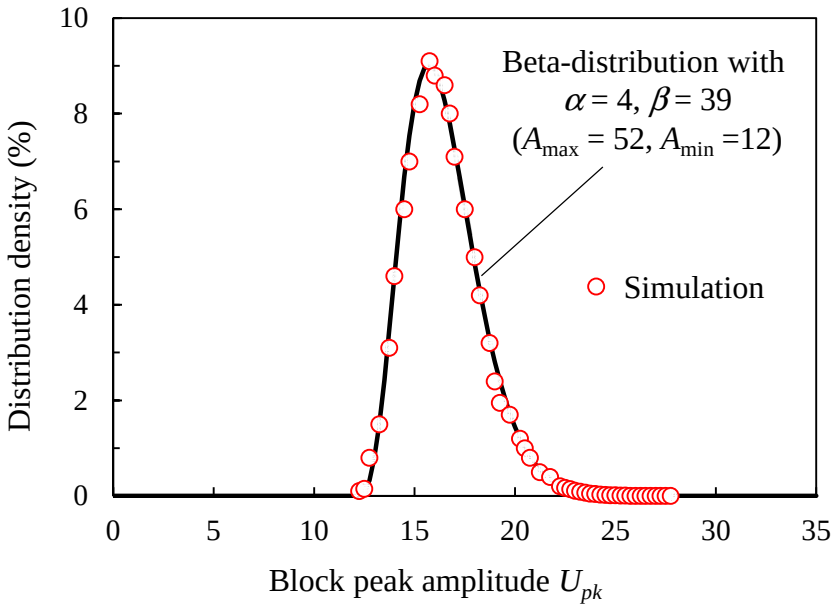

Fig. 3.5 Peak amplitude distribution density.

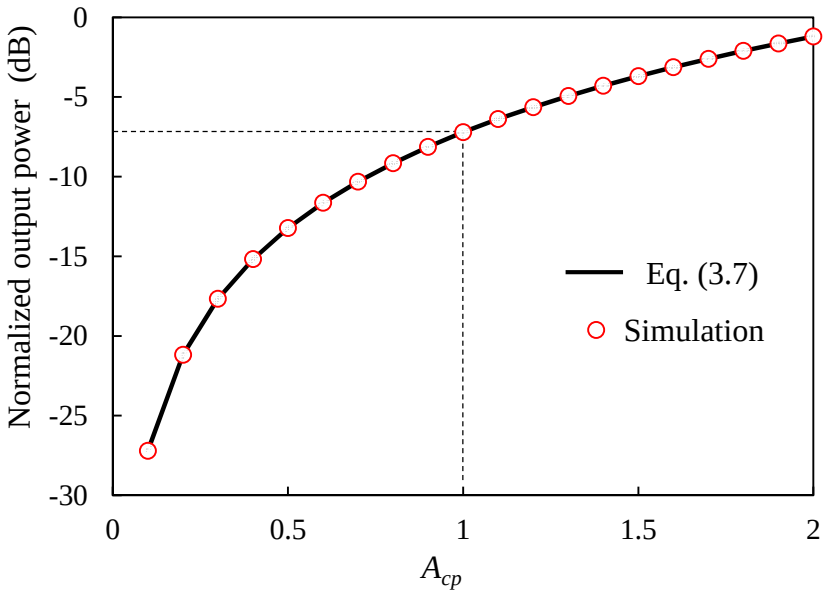

Fig. 3.6 Normalized output power vs. A_{cp}.

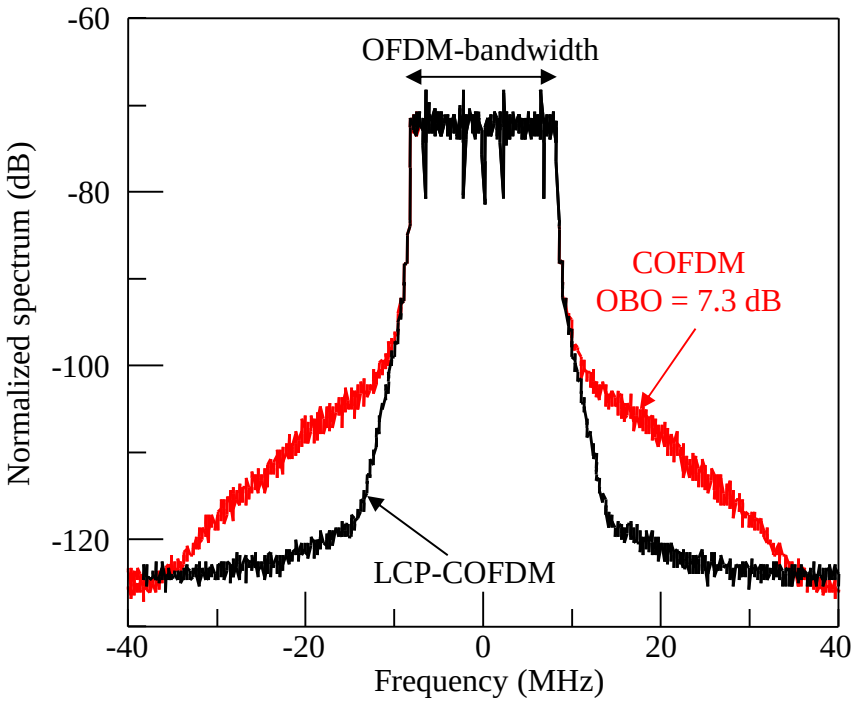

Fig. 3.7 Power spectrum with nonlinear distortion compensation (16-QAM, Class-AB model amplifier).

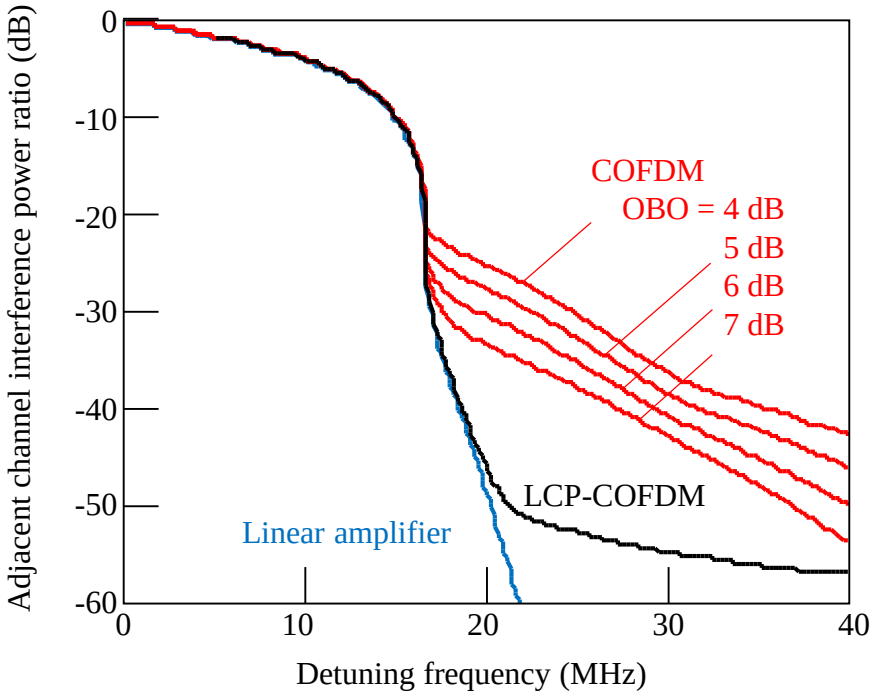

Fig. 3.8 Adjacent channel interference characteristics.

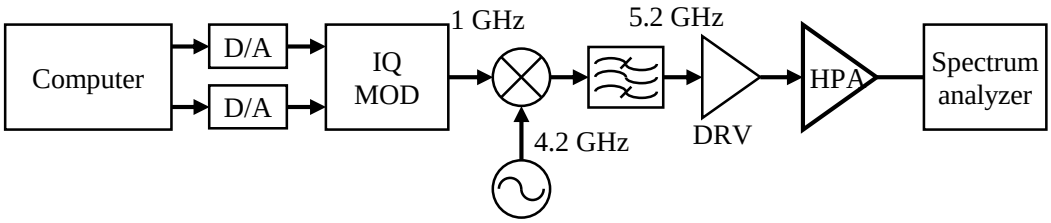

Fig. 3.9 Block diagram of LCP-COFDM.

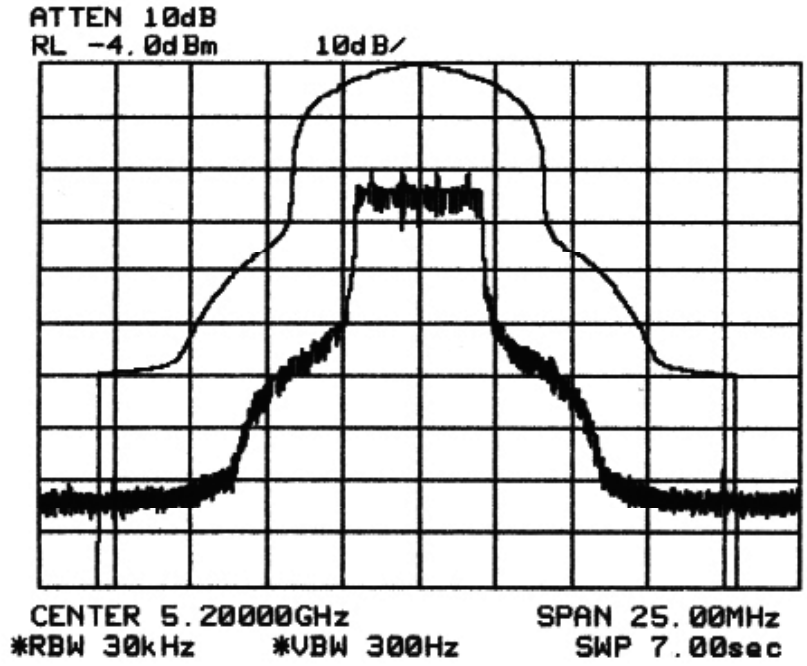

Fig. 3.10 Power spectrum of COFDM (OBO = 7.3 dB).

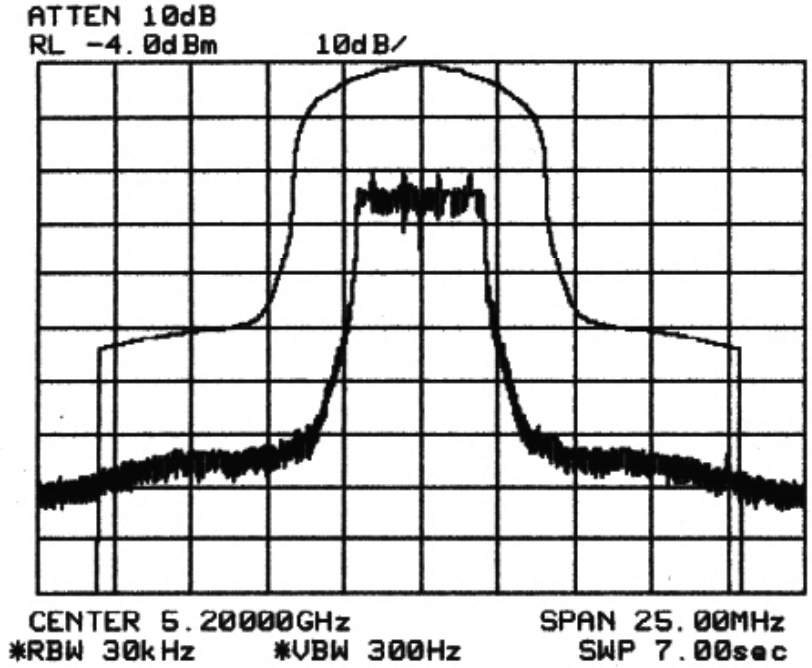

Fig. 3.11 Power spectrum of LCP-COFDM (OBO = 7.3 dB, A_{cp} = 1).

3.4 Performance Evaluation

3.4.1 Fundamental PER Performance

This subsection clarifies the fundamental packet error rate (PER) performance of LCP-COFDM under multipath fading channels. The following simulations assume Rayleigh fading with an exponentially-decaying power profile [3.13]; the delay interval is the sampling duration Ts as shown in Fig. 3.12, and the profile can be expressed by the following equation,

$$P_n = P_0 \exp(- n\, T_s / \tau_{rms}),\ n = 0,..., N_p - 1, \qquad (3.8)$$

where P_0 is a normalized constant and τ_{rms} is a root-mean-square delay spread. N_p denotes a number of paths (N_p = 30 in my simulations). The probability density function of the magnitude of each path is given as Rayleigh distribution and the functions are statistically independent. In the simulations, τ_{rms} of 150 nsec is used as a representative value typical of large hall-like environments.

For comparison, PERs with no linearizer are also examined as a function of OBO. The simulations consider coherent detection for 16-QAM and carrier recovery, symbol synchronization and channel estimation are assumed to be ideal. For FEC, convolutional coding and Viterbi decoding (Constraint length, K =7) with a coding rate of 1/2 are applied together with bit interleaving. The simulation results are shown in Fig. 3.13. For LCP-COFDM, although nonlinear distortion is almost completely eliminated, there is some degradation from the ideal PER performance. This is because CP-OFDM incurs some transmission power penalty, since it reduces the signal amplitude according to the peak amplitude of the corresponding block as can be seen in Eq. (3.2).

3.4.2 Improvement with Bit Interleaving

To enhance the ability of LCP-COFDM to alleviate the power penalty inherent to CP-OFDM, the interleaving size can be increased to 2 or more OFDM blocks. In general, the interleaving size is set to one OFDM block length to randomize the errors caused by the frequency-selective fading that occur over several consecutive subcarriers [3.15]. By employing the interleaving size of several OFDM blocks, the burst error in a specific power-reduced CP-OFDM block can be scattered over several blocks. The simulation results shown in Fig. 3.14 verify the effect of increasing bit interleaving size. The interleaving matrixes examined, defined as (depth, length) are (12, 16), (24, 16), and (36, 16), correspond to the interleaving size of 1, 2 and 3 OFDM blocks. As shown in Fig. 3.14, the interleaving size of 3 OFDM blocks achieves almost the same PER performance as that obtained with a linear amplifier; that is, 3-block-size interleaving is sufficient. As an example, 3-block-size interleaving achieves a 1.5 dB improvement compared to 1-block-size interleaving at a PER of 1 %.

Figure 3.15 summarizes the total degradation incurred in achieving a PER of 1 %; note that standardization bodies use 1-% PER as a criterion value in performance comparisons. The total degradation values were calculated by adding the OBO to the degradation in required E_b/N_0 against

that of the linear-amplifier at the maximum output power level (i.e., OBO = 0 dB) [3.16]. For example, in the case of COFDM of OBO = 5 dB with 3-OFDM-block interleaving, the lowest value becomes 6.1 dB. On the other hand, LCP-COFDM cannot reduce the OBO lower than 7.3 dB while maintaining the linearity. However, if the nonlinear distortion can be allowed to some degree, LCP-COFDM can increase the output power of the amplifier by setting the parameter A_{cp} over 1, and obtain the lowest total degradation of 4.9 dB when OBO = 3.8 dB (A_{cp} = 1.6).

3.4.3 ACI Examination

PER performance with ACI is evaluated by simulation. The desired channel is assumed to suffer from interference from the two adjacent channels on the both sides. Note that the CSP of 20 MHz is used as in Section 3.3, and every transmitter is assumed to have the same condition. The simulation results with 3-block interleaving are shown in Fig. 3.16, where D/U represents the power ratio of the desired channel to one of the adjacent interfering channels. Since LCP-COFDM causes very small ACI (see Fig. 3.8), the PER performance in terms of ACI substantially surpasses that of COFDM. Figure 3.17 shows the required D/U required to achieve a PER of 1 % versus OBO. As shown in Fig. 3.17, when OBO = 7.3 dB (i.e., A_{cp} = 1), LCP-COFDM offers the required D/U of -28 dB with 3-block interleaving. COFDM, on the other hand, needs an OBO of 20 dB or more to achieve such D/U values.

As a specific example, LCP-COFDM improves the required D/U by 14 dB compared to COFDM at OBO = 7 dB. In this case, given the propagation distance characteristic expressed as d2.9 power decay [3.17], LCP-COFDM allows the distance between the desired station and adjacent interfering station to be reduced to one third that in the COFDM case. Thus, it can be said that proposed technique is very effective in allowing a system to accommodate a larger number of users with more stations.

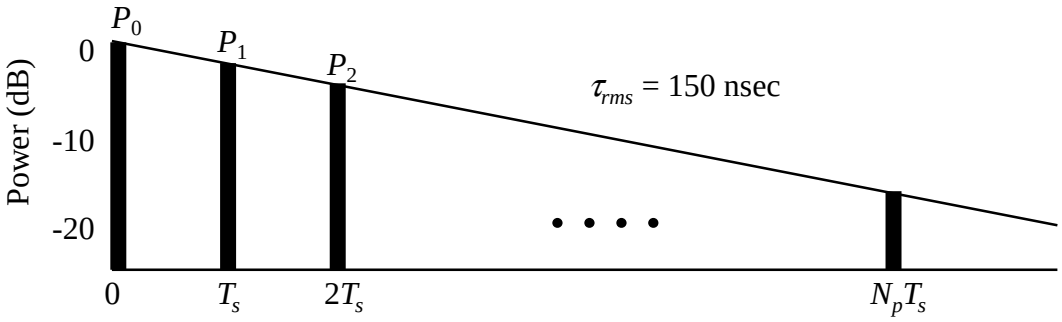

Fig. 3.12 Exponentially-decaying power profile.

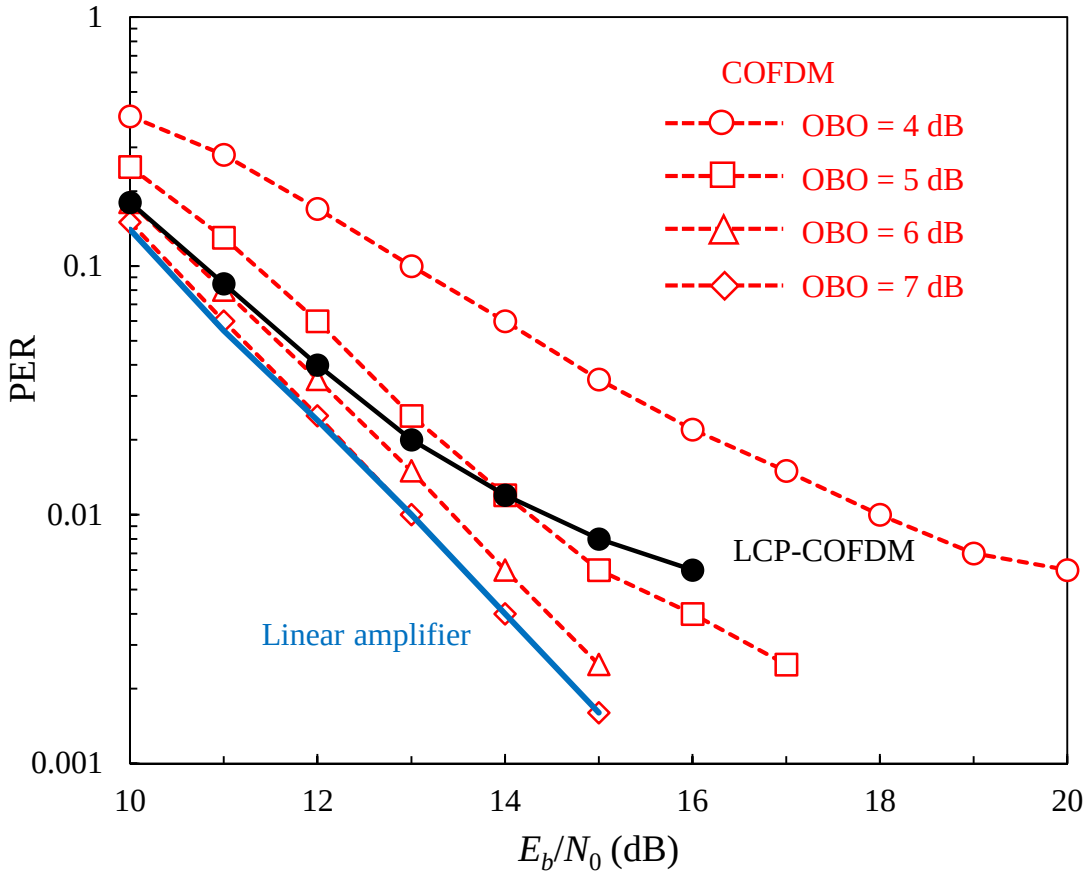

Fig. 3.13 PER vs. E_b/N_0.(16-QAM, Class-AB model amplifier).

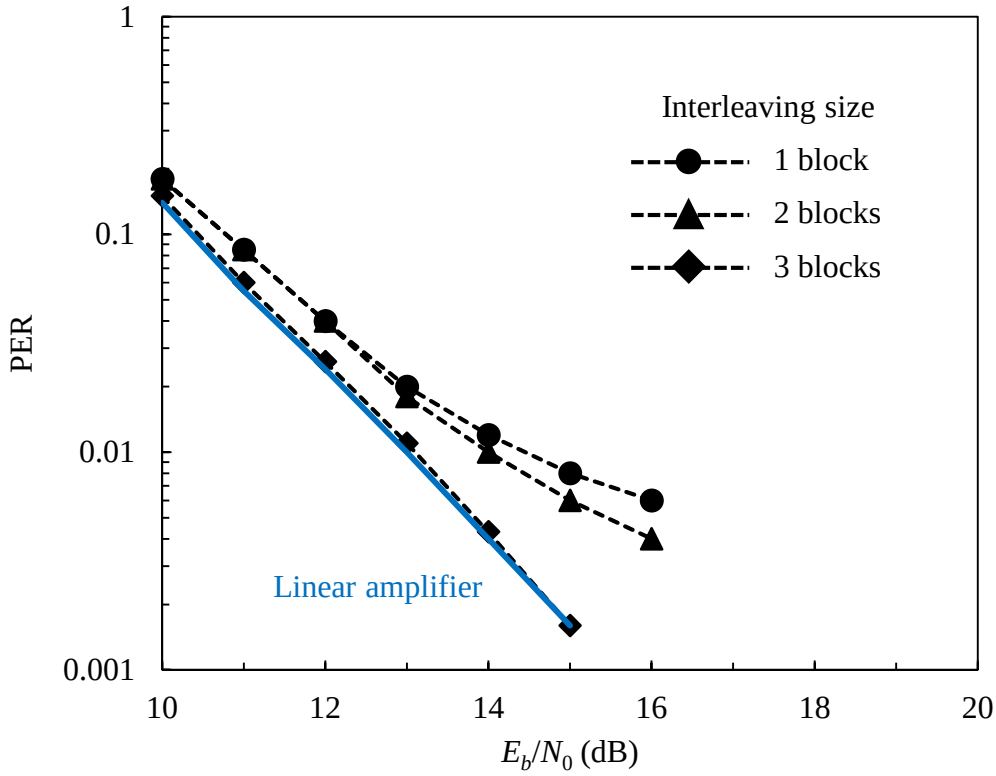

Fig. 3.14 PER performance of LCP-COFDM for various sized interleaving (16-QAM, Class-AB model amplifier).

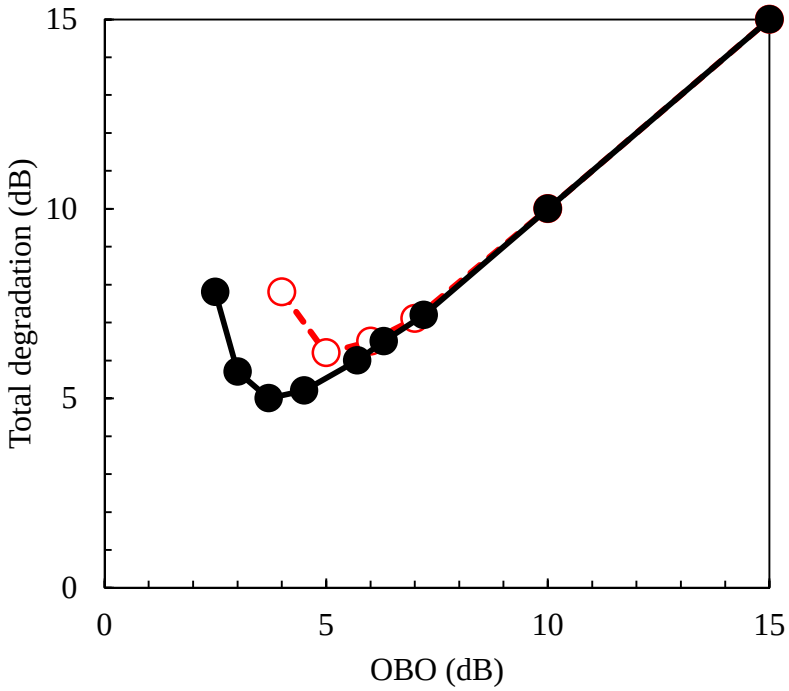

Fig. 3.15 Total degradation with PER = 1% (16-QAM, Class-AB model amplifier, 3-block-size interleaving).

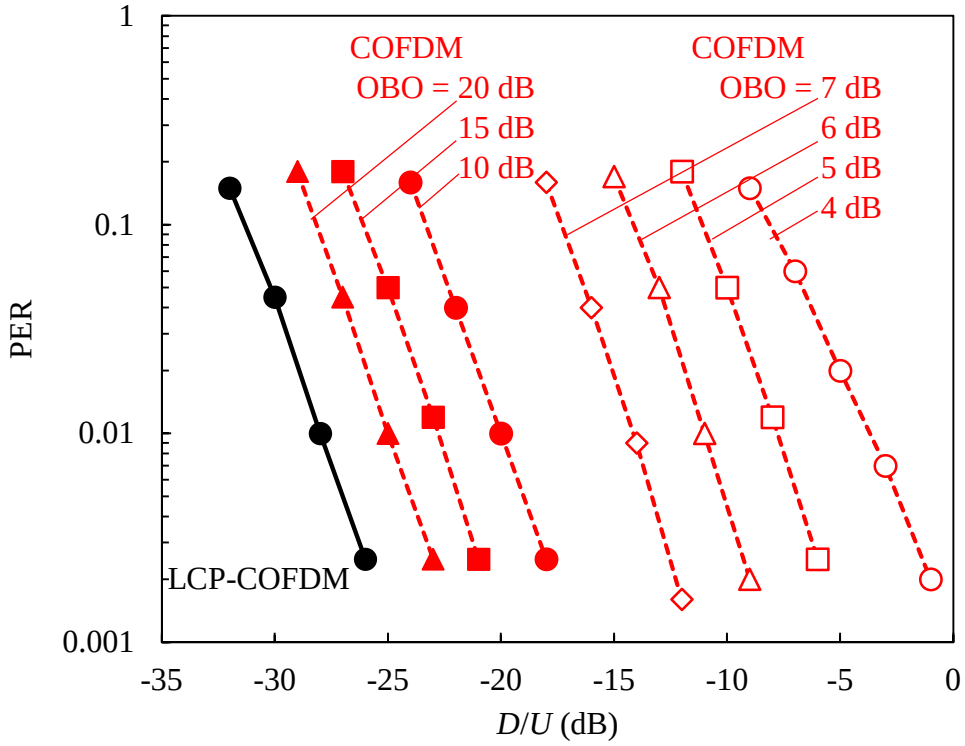

Fig. 3.16 PER performance with ACI
(16-QAM, Class-AB model amplifier, 3-block-size interleaving).

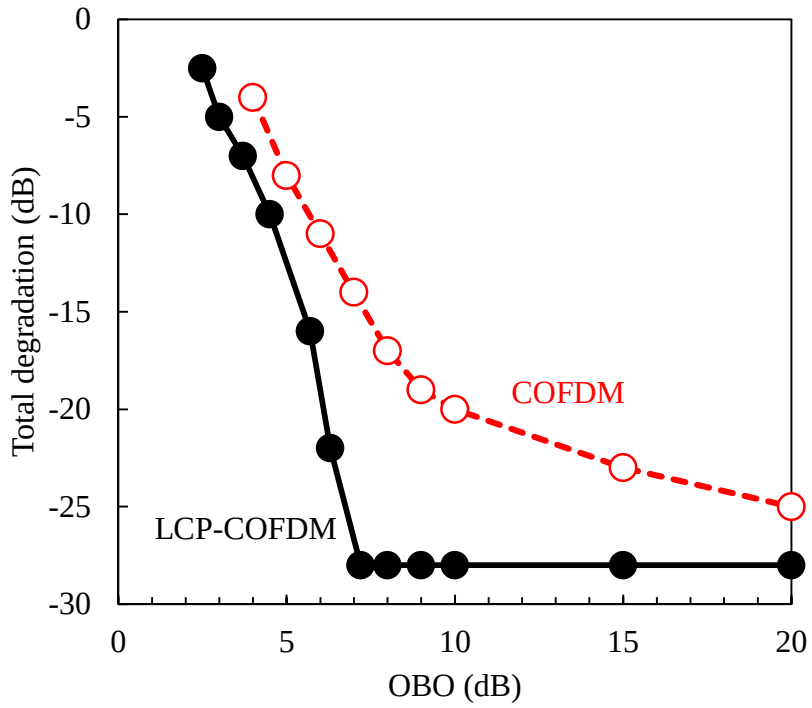

Fig. 3.16 PER performance with ACI
(16-QAM, Class-AB model amplifier, 3-block-size interleaving).

3.5 Conclusion

This chapter proposed LCP-COFDM as a novel technique for compensating nonlinear distortion in broadband wireless OFDM systems. This technique incorporates the baseband predistortion with the CP-OFDM technique. The CP-OFDM technique can reduce the PAPR while maintaining linearity of the IFFT outputs. By using this feature, the baseband predistorter fully compensates the nonlinear distortion. This chapter presented simulation and experimental results that validate the proposed method.

The OFDM has been used by mobile communication systems such as WiMAX and LTE as well as wireless LAN. The linearizer combing PAPR reduction techniques with baseband predistorter is always implemented at these devices, and it continues to being improved in terms of performance and implementation [3.18]-[3.20].

References for chapter 3

[3.1] IEEE 802.11a-1999: “IEEE Standard for Telecommunications and Information Exchange between Systems - LAN/MAN Specific Requirements - Part 11: Wireless Medium Access Control (MAC) and physical layer (PHY) specifications: High Speed Physical Layer in the 5 GHz band”.

[3.2] ETSI. BRAN, “HIPERLAN Type 2; physical (phy) layer. Technical Specification ETSI TS 101 475 V1.2.2 (2001-02),” ETSI, Feb. 2001.

[3.3] Amendment of the Commission’s Rules to Provide for Operation of Unlicensed NII devices in the 5 GHz Frequency Range, FCC 97-5, Jan. 1997.

[3.4] IEEE Std. 802.11 - 2012: IEEE Standards for Information Technology -- Telecommunications and Information Exchange between Systems -- Local and Metropolitan Area Network -- Specific Requirements -- Part 11: Wireless LAN Medium Access Control (MAC) and Physical Layer (PHY) Specifications, March 2012.

[3.5] X. Li and L. J. Cimini, Jr., “Effects of Clipping and Filtering on the Performance of OFDM,” IEEE VTC’97, pp.1634-1638, May 1997.

[3.6] R. D. J. van Nee, “OFDM Codes for Peak-to-Average Power Reduction and Error Correction,” IEEE GCOM’96, pp.740-744, 1996.

[3.7] R. Dinis, P. Montezuma, and A. Gusmao, “Performance trade-offs with quasi-linearly amplified OFDM through a two-branch combining technique,” IEEE VTC’96, pp.899-903, May 1996.

[3.8] A. S. Wright, and W. G. Durtler, “Experimental Performance of an Adaptive Digital Linearized Power Amplifier,” IEEE MTT-S Digest, pp.1105-1108, 1992.

[3.9] T. Matsuoka, et al, “Compensation of Nonlinear Distortion during Transmission Based on the Adaptive Predistortion Method,” IEICE Trans. Electron., vol. E80-C, No. 6, pp.782-787, June 1997.

[3.10] T. Maniwa, T. Hasegawa and Y. Tozawa, “A Study of Base-band Pre-distortion Linearizer for W-CDMA Mobile Station,” IEICE Comm. Soc. Conf., B-5-150, Oct. 1998.

[3.11] M. G. Di Benedetto and P. Mandarini, “An Application of MMSE Predistortion to OFDM Systems,” IEEE Trans. on Commun., vol. 44, No. 11, pp.1417-1420, Nov. 1996.

[3.12] W. G. Jeon, K. H. Chang and Y. S. Cho, “An Adaptive Data Predistorter for Compensation of Nonlinear Distortion in OFDM Systems,” IEEE Trans. on Commun., vol. 45, No. 10, pp.1167-1171, Oct. 1997.

[3.13] Y. Matsumoto, N. Mochizuki, and M. Umehira, “A Novel Peak Power Reduction Technique for Broadband Microcellular OFDM Systems,” IEICE Technical Report, RCS97-143, pp.103-108, Oct. 1997.

[3.14] M. Johansson and T. Potscher, “Input on power amplifier models,” ETSI BRAN document, 3ERI073B.

[3.15] D. Hayashi, “Effects of time interleaving for mobile reception on OFDM,” IEICE Comm. Soc. Conf., B-5-21, Sept. 1998.

[3.16] M. Friese, “On the degradation of OFDM-signals due to peak-clipping in optimally predistoted power amplifier,” IEEE GCOM’98, vol. 2, pp.939-944, Nov. 1998.
[3.17] J. Airs, “Comparative Indoor RF Channel Soundings at 2, 5 & 17 GHz,” Wireless Personal Communications, vol. 3, No. 4, pp.353-363, Dec. 1996.
[3.18] T. Horiuchi, W. Yang, T. Ohtsuki and I. Sasase, “Performance evaluation of OFDM with a nonlinear distortion compensation technique using partial transmit sequence and predistortion,” IEICE Trans. Commun., vol. J85-B, No. 11, pp.1865-1873, Nov. 2002.
[3.19] N. Aizawa, O. Muta, Y. Akaiwa, M. Sawahashi, “Effect of peak power suppression and adaptive predistortion on power amplification of an OFCDM signal,” IEEE VTC 2005-Spring, vol. 3, pp. 1783-1787, May 2005.
[3.20] M. C. Paredes Paredes and M. J. Fernandez-Getino Garcia, “Energy efficient peak power reduction in OFDM with amplitude predistortion aided by orthogonal pilots,” IEEE Trans. on Consumer Electronics, vol. 5, Issue 1, pp.45-53, Feb. 2013.

Chapter 4

Co-channel Interference Reduction Effect at High Elevation Base Station Using Beam Tilt and Orthogonal Polarization

4. Co-channel Interference Reduction Effect at High Elevation Base Station Using Beam Tilt and Orthogonal Polarization

4.1 Introduction

The number of subscribers to the personal handy-phone system (PHS) [4.1], which was developed and successfully implemented in Japan as a wireless personal communication service (PCS), has continued to increase beyond 80 million mostly in middle South American, African, and Asian countries especially China [4.2]. PHS supplies not only public wireless services but also wireless local loop (WLL) and fixed wireless access (FWA) systems [4.3], and has recently been applied to new services such as logistics [4.4] and ETC [4.5].

In a PHS system with a street microcell [4.6], all base station (BS) antennas are installed at locations lower than the surrounding buildings. The buildings form a radio zone called a street microcell along the street. As a fundamental concept in PHS design, the street microcell does not assume the occurrence of co-channel interference (CCI) between BSs. This is because the buildings act as obstacles and as a result increase the propagation loss compared to that of elevated BSs because of the low BS height. Attention should be paid to the fact that commercial PHS with a street microcell basically uses vertically polarized antennas; therefore, the polarization of the CCI waves is mainly vertical as reported in [4.7]. One of the disadvantages of the PHS street microcell is that numerous BSs are needed to cover all service areas and installing many BSs is costly. When I construct commercial systems, I frequently face a rather exceptional situation in conjunction with the expansion of PHS service areas. PHS adopts a cell architecture called a mixed cell architecture [4.8] in which both microcells and macrocells co-exist in the same geographical area using high-elevation BS antennas to form circular macrocells, even though constructing high elevation BSs is contrary to the original PHS design principle.

In a PHS system with a macrocell, BS antennas with an omni-directional radiation pattern and high gain such as collinear antennas are usually mounted at a high location such as the rooftop of a building to cover a wide area with circular radio zones as shown in Fig. 4.1. Such an elevated BS antenna experiences severe CCI from other surrounding BS antennas. This is because the propagation loss of the CCI decreases and no obstacles exist at the level of the BS receiving the interference (hereafter interference receiving base station (IRBS)) to block the CCI when the antennas of the IRBS are mounted at high locations such as a rooftop. As a consequence of these situations, an IRBS in a PHS system set on a rooftop cannot find an available time slot in the time division multiple access/time-division duplex (TDMA/TDD) scheme by employing autonomous distributed control and they cannot transmit control channel (CCH) signals because all the time slots are frequently occupied by the CCI with higher levels than the carrier sense level of PHS.

It is well known that the easiest and most economical method to suppress CCI is the beam down-tilt technique [4.9]-[4.13]. This technique, which generates nulls in the horizontal plane, is often used to reduce the CCI and was adopted in many BS antennas in both cellular and

microcellular wireless communication systems throughout the world. Another method to reduce CCI for high-elevated BSs in a macrocell is the autonomous decentralized synchronization technique [4.14], [4.15], which synchronizes time slots in TDMA/TDD between BSs to lower the CCI and increase the channel capacity. Unfortunately, these techniques offer only limited success and a more effective approach is still needed. As an alternative method to suppress the CCI, adaptive array antennas were newly proposed and shown to suppress the CCI for elevated PHS BSs [4.7]. However, the adaptive array antennas used in this configuration are rather expensive compared to the conventional BS antennas for commercial systems.

The adoption of horizontally polarized diversity antennas with beam tilt is another method to reduce the CCI further. This method provides both polarization orthogonal to that of the CCI waves and beam tilt effects. When horizontally polarized diversity antennas that have a high peak gain comparable to that of collinear antennas are used for such a high elevation BS, the following items should be studied or clarified: the CCI reduction effect, and the radio zone length (RZL) with respect to the inclination angle of the mobile antenna based on measurements. These two research topics are of great significance to the design and development of commercial microcell systems. To the best knowledge of the authors, there is no report that shows the CCI reduction effect based on empirical data when the three techniques, i.e., beam tilt, use of orthogonal-polarization, and a combined technique of beam tilt / orthogonal-polarization, are employed for BS antennas.

This chapter addresses the problem of the CCI generated in a mixed cell architecture in PHS that adopts the TDMA/TDD scheme by using horizontally polarized omni-directional array antennas in a height-diversity configuration that permits PHS BS antennas established at high elevations to form a macrocell and cover a wide area with circular radio zones. In association with the CCI reduction technique using horizontally polarized diversity antennas for IRBSs, the concept of a polarization arrangement for the BS antennas in a mixed cell architecture is introduced. I developed a dielectric-loaded slotted-cylinder antenna (DSCA) array antenna that has a horizontally polarized omni-directional radiation pattern with a high gain that is comparable to that of a collinear antenna. I applied it to dual-polarized omni-directional diversity antennas to compensate for the deterioration in the received signal due to a mismatch in the polarization direction between the base station antenna and mobile station antenna [4.16]. In this chapter, the DSCA array is applied to horizontally polarized omni-directional array antennas in a height-diversity configuration to reduce the CCI. The measurements conducted in a suburban area clarify the change in the distribution of interfering BSs (IBSs) and the reduction effect in the CCI for three techniques: beam tilt, the use of horizontally polarized antennas, and a combination of the beam tilt and horizontally polarized antennas. The impact of the inclination angle of the mobile antenna on the RZL of the DSCA array is shown based on measurements on an urban street.

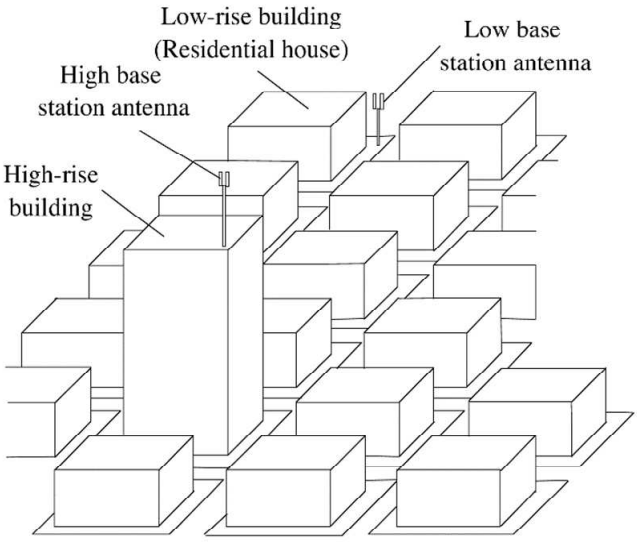

Fig. 4.1 Co-channel interference between high base station and low base station antennas in TDMA/TDD system.

Section 4.2 describes the CCI reduction technique that employs horizontally polarized antennas with beam tilt for the IRBS and a polarization arrangement of BS antennas in a mixed cell architecture. It also describes a method for estimating the RZL with respect to the inclination angle of the mobile antenna. In Section 4.3, the measurement results of the CCI reduction effect achieved by the DSCA array antenna are shown for comparison to that of a collinear antenna. Section 4.4 shows the RZL variations in the DSCA array and collinear antennas with respect to the inclination angle of the mobile antenna. Section 4.5 discusses the results from this study and future work. Finally, our conclusions are presented in Section 4.6.

4.2 CCI Reduction Technique, Polarization Arrangement in Mixed Cell Architecture, and RZL Estimation Method

4.2.1 CCI Reduction Technique and Polarization Arrangement in Mixed Cell Architecture

The CCI reduction technique using polarization orthogonal to that of the CCI waves and a high and low base station antenna arrangement sharing vertical and horizontal polarization are shown in Fig. 4.2. In the mixed cell architecture considered in this study, which is contrary to the current architecture, an IRBS at a high elevation separately uses horizontally polarized omni-directional

antennas with/without beam tilt to cover a circular radio zone to form macrocells. It is expected that horizontally polarized diversity antennas with beam tilt will most effectively reduce the CCI level due to the combined effect of both the horizontal polarization and beam tilt.

Polarization diversity is the most effective solution to compensate for the deterioration in the received signal due to a mismatch in the polarization direction between the BS antenna and mobile station antenna, and dual-polarized antennas were proposed to minimize the degradation in the received signal strength for both PHS BS antennas in high [4.16] and low elevation BSs [4.17]. It should be emphasized that this chapter investigates the IRBS set on a rooftop in propagation environments in which the polarization diversity technique cannot be applied because of the following reasons: Severe CCI as described in [4.7]; because the diversity branch of a vertically polarized antenna of a dual-polarized diversity antenna receives high-level vertically polarized CCI waves; because an available time slot cannot be found in TDMA / TDD; and because a link cannot be established between the BS and user terminals no matter how the other branch, a horizontally polarized antenna, lowers the CCI level.

4.2.2 RZL Estimation Method

It has been generally believed that the RZL should be estimated with respect to only the angle at which polarization matching between the BS and mobile antennas is satisfied. Since mobile handy-phones equipped with whip antennas or built-in antennas are inclined at various angles when people use them, the received signal level at the BS also degrades due to a mismatch in the polarization direction between the BS antenna and mobile station antenna [4.18]. It is of more significance to resolve the degradation in the received signal level caused by a mismatch in the polarization direction between the BS antenna and mobile station antenna rather than the degradation in the gain of the radiation patterns caused by user proximity or the absorption of radiation power by the human body. The degradation of the former is greater than that of the latter [4.19]. It was also reported that the average inclination angle based on a statistical distribution of the handy-phones in use is approximately 60˚ as shown in Fig. 4.3 [4.20]. In this chapter, I compare RZLs based on two aspects: one is the averaging value when the mobile antennas are slanted from 0˚ to 90˚, and the other is with respect to the specific value when the mobile antennas are slanted at 60˚ as described in [4.20].

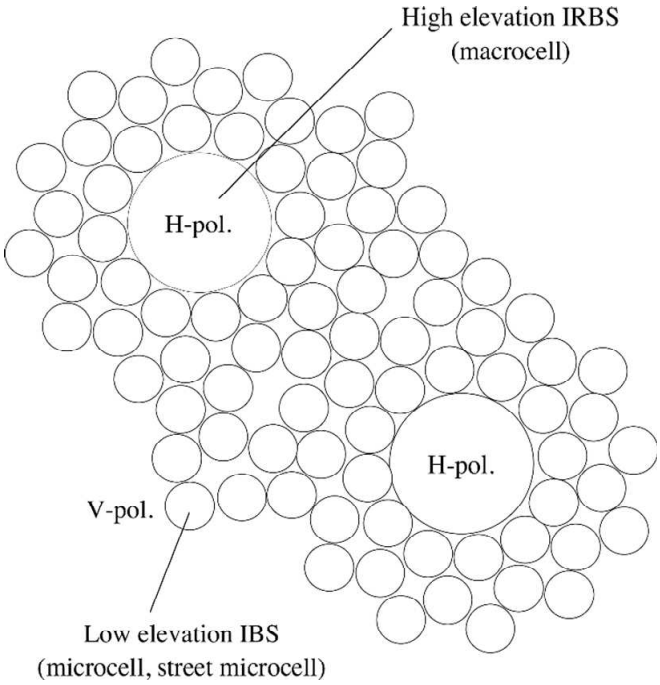

Fig. 4.2 High and low base station antenna arrangement sharing vertical and horizontal polarization.

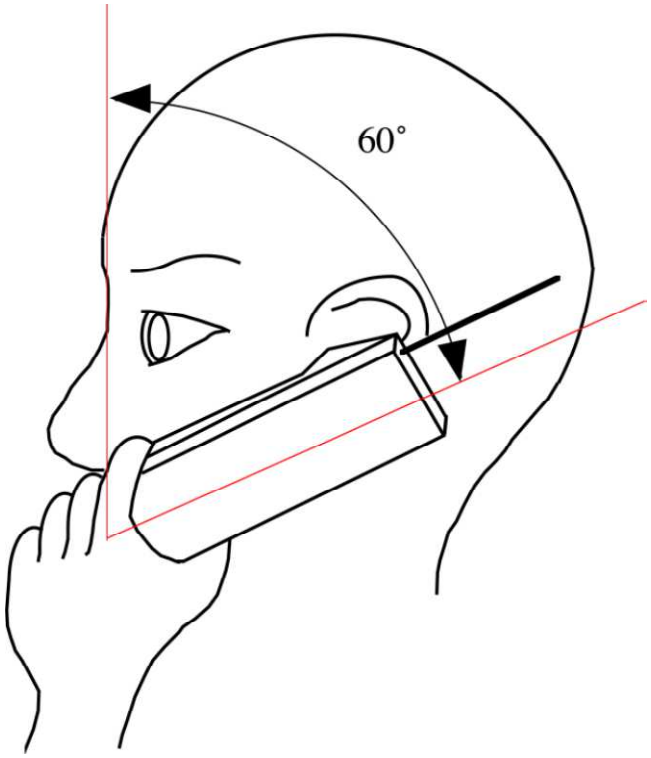

Fig. 4.3 Typical inclination angle of handy phone while talking.

4.3 Interference Reduction Effect

4.3.1 Measurement Scenario

The measuring point is on the rooftop of a 16 m-high building in the vicinity of a railway station in suburban commercial and residential areas. There are no obstacles around the building at the IRBS antenna level. The view from the rooftop is shown in Fig. 4.4. The IBS antennas are collinear antennas with no-beam tilt, have the peak gain of 8 dBi, the transmit power of 20 mW, and transmit a vertically polarized wave. It should be noted that all CCI waves are vertically polarized. The collinear antennas are set on power or telegraph poles at the height of approximately 7 m to 8 m above ground level. I chose the measurement sites where the CCI is the most severe, i.e., where the antenna height is higher than the rooftop levels of two-story residential houses. Therefore, the condition of the antenna height is inconsistent with the street-microcell design; however, the measured results are considered to be the worst estimation of the CCI. The IBSs are distributed widely in locations that straddle suburban areas in the cities of Kyoto, Mukou, and Nagaoka-kyou in Japan as shown in the maps (Figs. 4.10 and 4.11). The CCI levels were measured for the top branch of the diversity branches and diversity reception was not applied. The control channel (CCH) signal at 1.916 GHz is used for CCI level measurements. A measurement receiver (PHS Measuring receiver ML5661A, Anritsu Corporation, Japan) was used to receive the CCH signals. A block diagram of the CCI measurement equipment is shown in Fig. 4.5. In this study, the effects of interference reduction were statistically estimated using cumulative distribution curves of the received CCI levels for each IRBS antenna configuration. I did not analyze the details of each propagation path between individual IBS antennas and the IRBS antenna on the rooftop. I also did not confirm line-of-sight (LOS) propagation conditions between each IBS antenna and the IRBS antenna.

I developed a DSCA array antenna that has a horizontally polarized omni-directional radiation pattern with a high gain that is comparable to that of a collinear antenna and applied it to dual-polarized omni-directional diversity antennas [4.16]. The peak gain is approximately 8 dBi, and is comparable to that of the conventional 4-element collinear antennas. The down-tilt angle is approximately 15˚. It should be noted that these array antennas are designed for the commercial 1.9 GHz band in this measurement. The specifications of the DSCA prototype and conventional collinear antenna are summarized in Table 4.1. In this study, I applied the DSCA array to horizontally polarized omni-directional antennas with a high gain at elevated PHS BSs mounted on rooftops of buildings to form a circular radio zone. Conventional collinear antennas without beam tilt (V_antennas), conventional collinear antennas with beam tilt (V_tilt_antennas), DSCA array antennas without beam tilt (H_antennas), and DSCA array antennas with beam tilt (H_tilt_antennas), were used to measure the CCI levels. The radiation patterns for V_antennas, V_tilt_antennas, H_antennas, and H_tilt_antennas are shown in Figs. 4.6, 4.7, 4.8, and 4.9, respectively.

4.3.2 Distribution of Interfering BSs

The changes in distribution of the IBS antennas are mapped in Figs. 4.10 and 4.11. I should note that the total number of IBSs is 48 and signals from all the BSs are certainly received by at least one of four antenna configurations. Since the minimum received signal sensitivity level of the measurement receiver is approximately 20 dBμV, the IBSs for which the CCI levels are less than 20 dBμV are not shown in the figures. Figures 4.10 and 4.11 show that the distribution areas and the number of IBS antennas become progressively smaller corresponding to the order of V_antennas, V_tilt_antennas and H_antennas, H_tilt_antennas. The CCIs from the IBS antennas installed in street microcells in the urban area around the JR Kyoto Station are not received at all due to blocking by a group of high-rise buildings, while the CCI from the IBS established on the famous Kiyo-mizu Temple in the mountainous Higashi-yama district as indicated by the arrow in Fig. 4.10 is received at an exceptionally high level because the measuring point and the temple are unintentionally in LOS propagation. The relationship between the received CCI levels versus the distances between the IRBS and the IBSs are shown in Fig. 4.12. The changes in the numbers of visible IBSs, the IBSs among the visible IBSs at which the CCI levels received by the IRBSs are higher than the carrier sense level of 26.5 dBμV, and the farthest distance of the IBS from the measuring point for the four types of antenna configurations are summarized in Table 4.2. The distribution areas, the number of IBSs, and the received CCI level become progressively smaller corresponding to the order of V_antenna, V_tilt_antenna and H_antenna, H_tilt_antenna. Considering the farthest distance of 9400 m from the IBS at the temple as an exception, the farthest distance of 1500 m from the IRBS to an IBS when using the H_tilt_antenna is approximately less than 23% of those of when using the V_tilt_antenna and V_antenna. It is clear that the H_tilt_antenna effectively decreases the CCI compared to the H_antenna and V_tilt_antenna. However, it is interesting to compare the difference in the CCI reduction effect between the V_tilt_antenna and H_antenna. The numbers of visible IBSs and IBSs at which the received CCI level is greater than the carrier sense level are decreased from 32 (66.7%) and 27 (56.3%) to 23 (47.9%) and 17 (35.4%) for the V_tilt_antenna and H_antenna, respectively. The farthest distances from the measuring point to an IBS are decreased from 6500 m to 2116 m for the V_tilt_antenna and H_antenna, respectively. These results show that the H_antenna is superior to the V_tilt_antenna in decreasing the CCI.

4.3.3 Interference Reduction Effect

The cumulative distribution curves of the received CCI levels for the four types of antenna configurations are shown in Fig. 4.13. It should be noted that the invisible IBSs in Figs. 4.10 and 4.11, defined for those with received CCH levels of less than 20 dBμV (the minimum received sensitivity level of the measurement receivers), are newly included as samples to each cumulative distribution. Therefore, the total number of samples in each cumulative distribution should be 48 as described in Section 4.3.2. All the received CCI levels of the invisible IRBSs are assumed to be

constant at 20 dBμV assuming the worst case of CCI. The CCI reduction effects are estimated at 80% probability of the cumulative distribution curves of the CCI because the measured data are valid and used for the estimation. The beam-tilt technique reduces the CCI level by approximately 10 dB for both the V_tilt_antenna and H_tilt_antenna. The use of horizontal polarization reduces the CCI level by approximately 13 dB for both the H_tilt_antenna and H_antenna. I confirm that the polarization effect is superior to the beam-tilt effect in reducing the CCI, and when only the beam-tilt technique is employed the CCI is insufficiently suppressed. The combined technique of the beam tilt and horizontal polarization reduces the CCI level by approximately 23 dB for the H_tilt_antenna. The CCI reduction effect when employing the H_antenna is only approximately 3 dB greater than that for the V_tilt_antenna, while the farthest distance from the measuring point to the interfering BS when using the H_antenna is approximately 23% of that when using the V_tilt_antenna as explained in Section 4.3.2. I confirm again that that the H_antenna is superior the V_tilt_antenna with respect to reducing the CCI. I note that the measurements on the CCI reduction effect were conducted in suburban or residential areas; however, I also confirmed the effect in dense urban areas in Osaka City by adopting the technique to BS antennas in commercial operation.

Fig. 4.4 View toward Fushimi-district shown in Figs. 4.10 and 4.11 from the rooftop at which co-channel interference was measured.

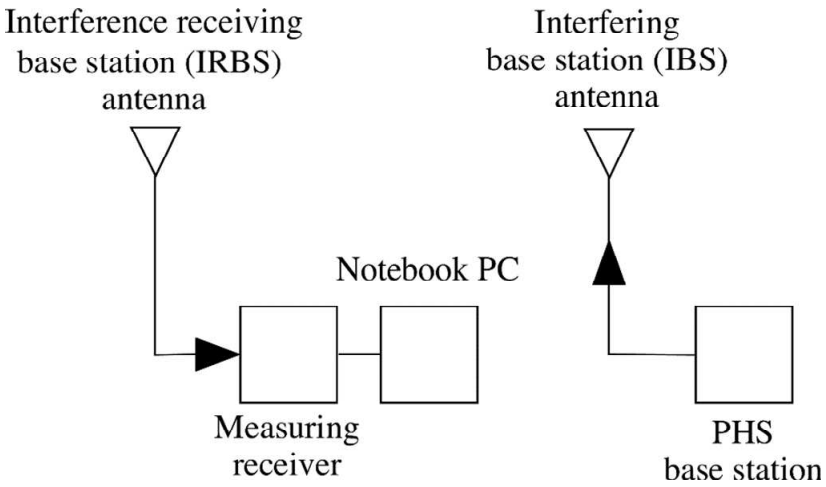

Fig. 4.5 Block diagram of CCI measurement equipment.

Table 4.1 Specifications of DSCA prototype and conventional collinear antenna.

	DSCA	Collinear
Diameter of Radome	22 mm	17 mm
Number of Elements	4	4
Gain	8 dBi	8 dBi
Polarization	Horizontal	Vertical
Down-Tilt Angle	15˚ / 0˚	15˚ / 0˚
Radiation Pattern	Omni	Omni

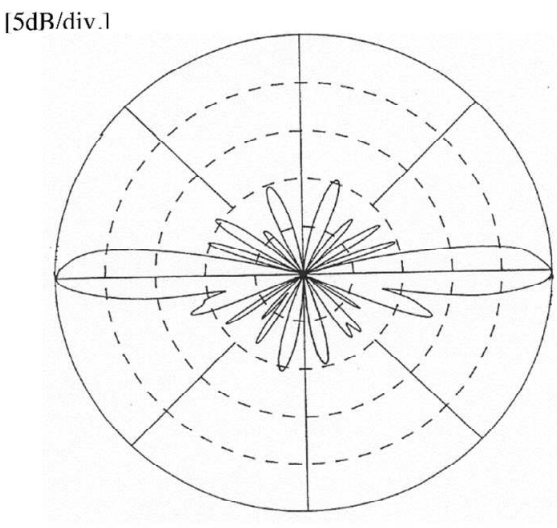

(a) Vertical plane

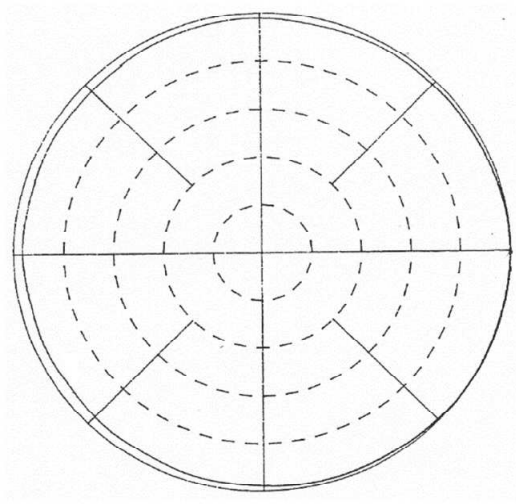

(b) Horizontal plane

Fig. 4.6 Measured radiation patterns of collinear antennas (V_antennas).

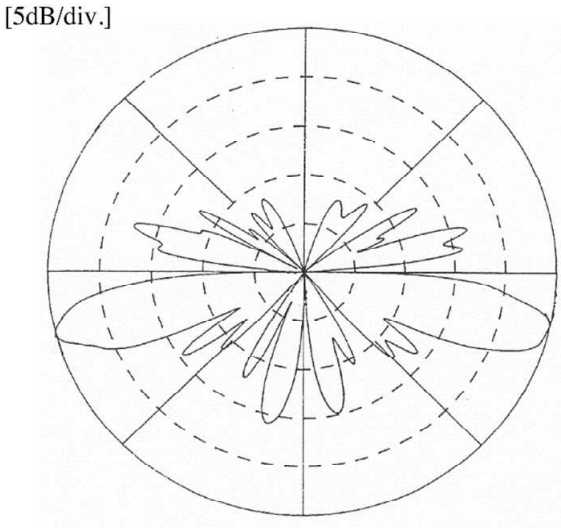

(a) Vertical plane

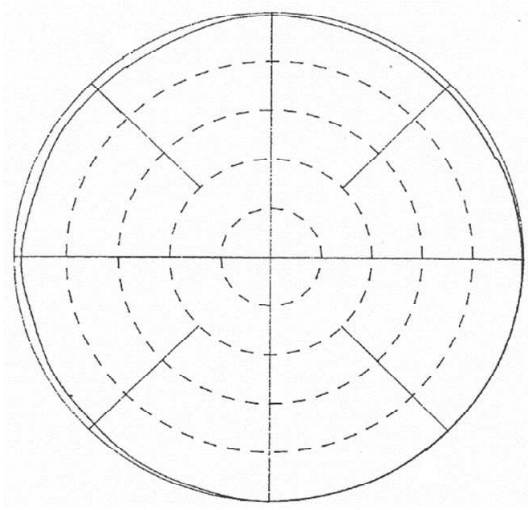

(b) Conical plane

Fig. 4.7 Measured radiation patterns of collinear antenna with beam tilt (V_tilt_antennas).

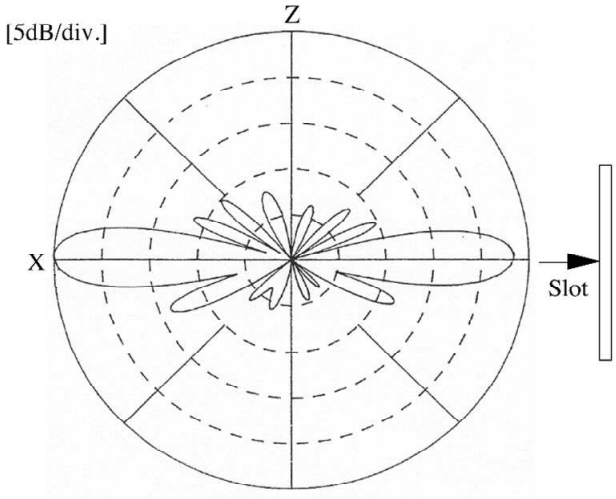

(a) Vertical plane

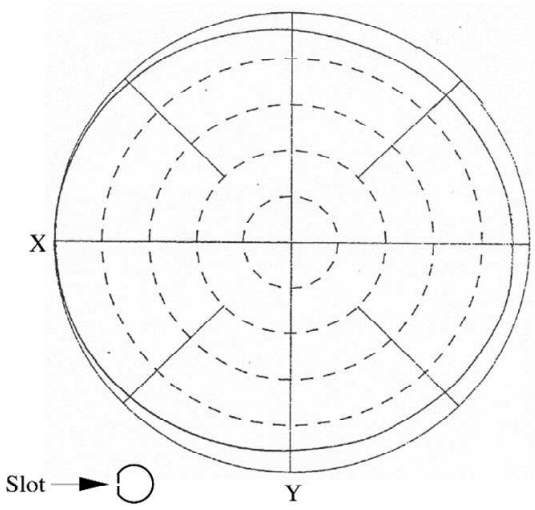

(b) Horizontal plane

Fig. 4.8 Measured radiation patterns of the four-element DSCA array (H_antennas).

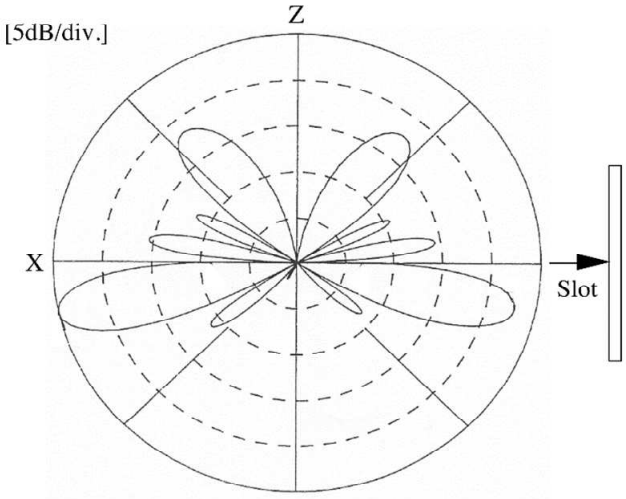

(a) Vertical plane

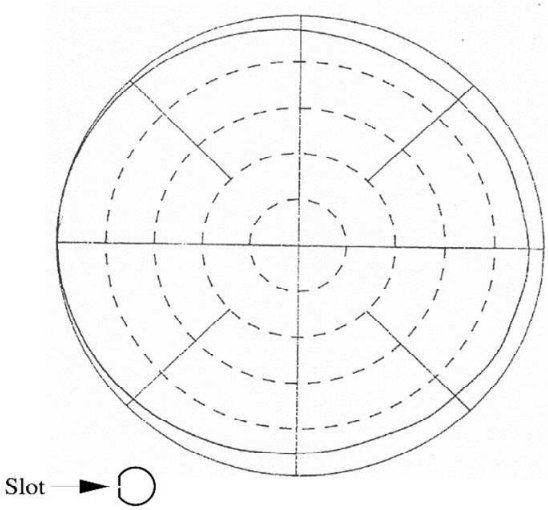

(b) Conical plane

Fig. 4.9 Measured radiation patterns of the four-element DSCA array with beam tilt (H_tilt_antennas).

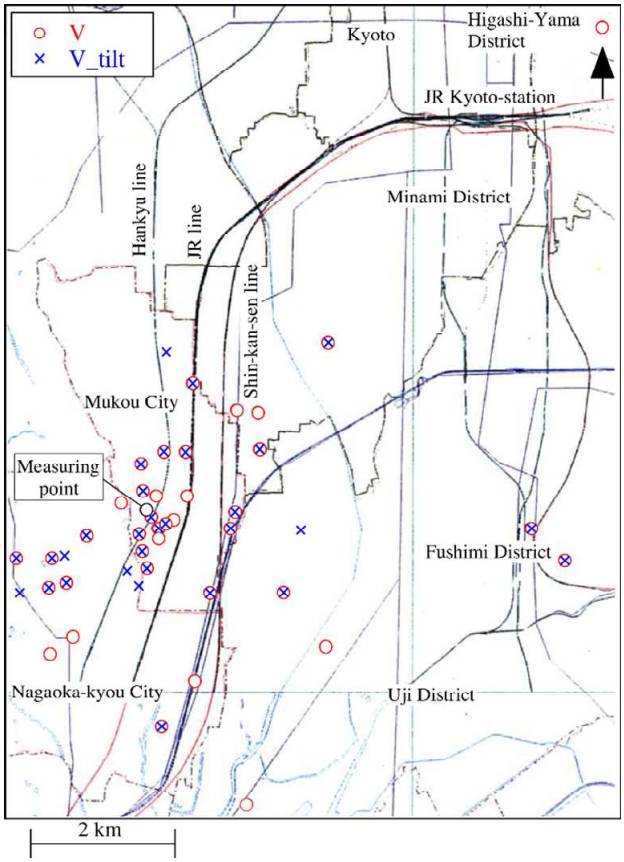

Fig. 4.10 Distribution of IBSs when IRBS antennas are V__antennas and V_tilt_antennas.

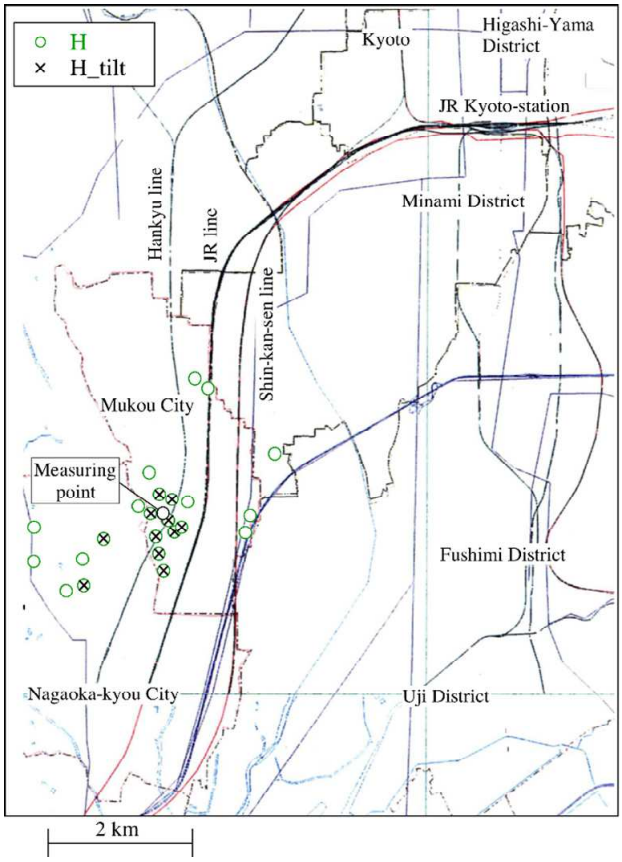

Fig. 4.11 Distribution of IBSs when IRBS antennas are H_antennas and H_tilt_antennas.

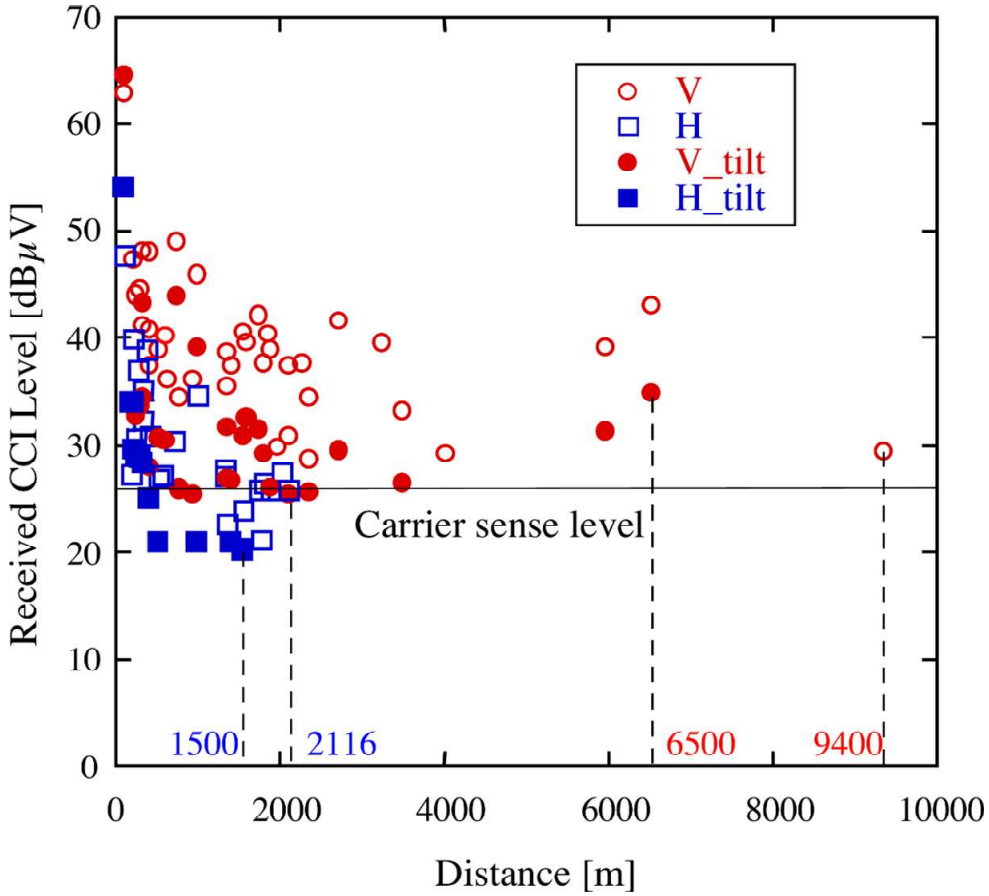

Fig. 4.12 Received CCI level versus distance of IBSs.

Table 4.2 Numbers of IBSs and the farthest distance to IBSs.

Antenna Configuration	Number of Visible IBSs*[1]	Number of IBSs Where Received CCI Level Is Greater than Carrier Sense Level*[2] [%]	Farthest Distances to IBSs [m]
V	38 (79.2 %)	38 (79.2 %)	6500 (9400)
V_tilt	32 (66.7 %)	27 (56.3 %)	6500
H	23 (47.9 %)	17 (35.4 %)	2116
H_tilt	11 (22.9 %)	6 (12.5 %)	1500

*[1]Total number of IBSs established in locations that straddle suburban areas is 48.
*[2]Carrier sense level is 26.5 dBμV.

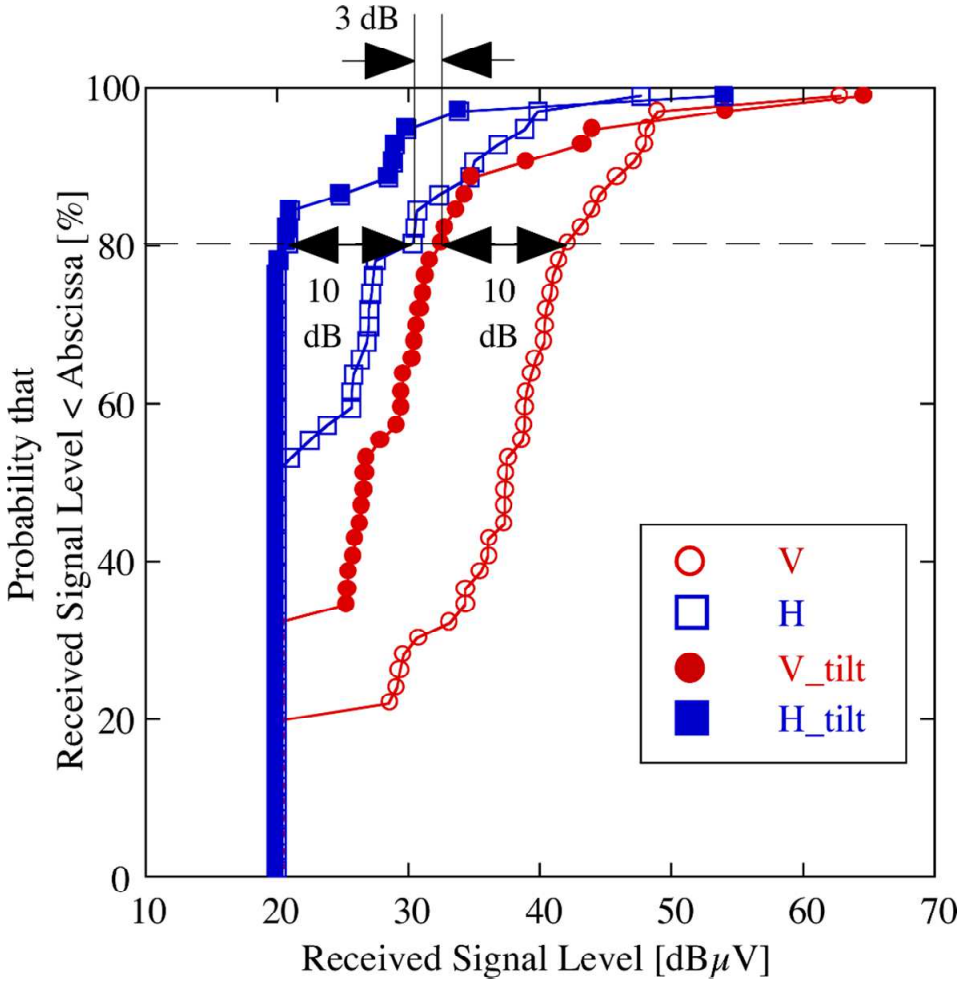

Fig. 4.13 Cumulative distribution of the received CCI level.

4.4 Radio Zone Length Measurement

4.4.1 Measurement Scenario

Measurement Scenario. The measurements of the RZLs for the four types of height-diversity antenna configurations were conducted on Yone-ga-hama street in an urban area in Yokosuka city. Figure 4.14 shows a scenario for measuring the RZLs on this urban street and the definition of the inclination angle in LOS environments. Figure 4.15 shows the view from the location of the base station antenna. A map of the area surrounding the BS antennas and measurement routes in LOS environments are shown in Fig. 4.16. The transmitting mobile antenna, a sleeve antenna at the height of 1.6 m, with the transmitting power of 25.85 dBm was mounted on a cart. The cart moved along the sidewalk of the 25-m wide street on the opposite side from a 30 m-high building in the LOS environments to determine the RZL. The receiving BS antennas were set on the rooftop of the building, and measurement receivers (Measuring Receiver ML524B, Frequency Converter MH669B, Anritsu Corporation, Japan) were used to receive the signals. The received signal levels were processed using selection diversity and the regression fitting curves were calculated. A block diagram of the RZL measurement equipment is shown in Fig. 4.17. The length of the LOS route was approximately 630 m. The measured frequency was 2.2 GHz. The proposed horizontally polarized diversity antennas were compared to regular collinear diversity antennas. The sleeve antenna representing the mobile antenna was inclined in the Z-X plane in LOS as depicted in Fig. 4.14(b). Approximately 6300 median values of the received signal were considered. One median value for every 0.1 m is calculated so that the original received signal over a 1 m (±0.5 m) interval was sampled at 100 kHz.

4.4.2 Radio Zone Length

The received signal levels for V_antenna / H_antenna and V_tilt_antenna / H_tilt_antenna are shown in Figs. 4.18 and 4.19, respectively. The received signal levels for a collinear antenna with no beam tilt for 0˚ and 90˚ are shown in Fig. 4.18 and are the same as those in Fig. 4.12 in [4.16]. In PHS, the acceptable propagation loss is designed to be 99 dB not accounting for antenna gains for personal and BS antennas. The transmitting power for this measurement is 25.85 dBm (138.85 dBμV) and results in 39.85 dBμV as the threshold. The RZLs are defined such that the regression fitting lines of the received signal level of the BS antennas exceed the threshold level of the system, 39.85 dBμV, when the mobile antenna moved away from the BS antenna. Note that the RZLs are normalized by the RZL of the V_antenna (vertical mobile antenna), i.e., 939 m, and are expressed as the RZL ration (RZLR) in percent. The RZLRs of both the V_tilt_antenna / V_antenna and H_tilt_antenna / H_antenna versus the inclination angle of the mobile antenna are shown in Fig. 4.20. The RZLRs for the four types of diversity antennas are summarized in Table 4.3. The parameters of the regression fitting lines for Figs. 4.18 and 4.19 are summarized in Table 4.4. The equation for the

regression fitting lines of the received signal levels is of the form.

$$RSL = A - B \cdot \log(d). \quad (4.1)$$

where RSL is the received signal level in dBμV, A is the constant, B is the attenuation coefficient, and *d* is the distance in meters. The threshold level at the end of the radio zone of the system is 39.85 dBμV. The purpose of this study is not to find the break point and a regression fitting line beyond the break point. The distance to the break point is given by an approximate equation using a two-ray model as follows:

$$Rb = 4\, ht\, hr / \lambda. \quad (4.2)$$

In this RZL measurement, *ht* = 30 m, *hr* = 1.6 m, λ = 0.136 m, and *f* = 2.2 GHz. Therefore, *Rb* = 1412 m and the RZL values are before the break point.

At approximately 12% (111 m) of the RZLR, I observed that the received signal levels of both the V_ tilt_antenna and H_tilt_antenna shown in Fig. 4.19 are increased compared to those for both antennas without beam tilt shown in Fig. 4.18. The RZLR corresponds to the maximum distance at which the beams intersect the road in the measurement routes. Figure 4.20 shows that the RZLRs of the V_tilt_antenna / V_antenna are decreased by approximately 30 and 73%, respectively, when the mobile antennas are inclined from 0˚ to 90˚, while the RZLRs of the H_tilt_antenna / H_antenna are increased by approximately 37 and 26%, respectively, when the mobile antennas are inclined from 0˚ to 90˚. The average RZLRs for the H_antenna / H_tilt_antenna are 66.6 and 62.8% and approximately 1.1 and 1.6 fold greater than those for the V_antenna / V_tilt_antenna, respectively. It was reported that the average inclination angle distribution of a handy-phone in use is approximately 60˚ [4.20]. The RZLRs at a 60˚ inclination of the mobile antennas for the H_antenna / H_tilt_antenna are 78.3 and 70.7% and approximately 1.6 and 1.9 fold greater than those for the V_antenna / V_tilt_antenna, respectively. The variations in the RZL have not been taken into account in the system design up to now. I conclude from Fig. 4.20 that the H_antenna / H_tilt_antenna is superior to the V_antenna / V_tilt_antenna if I take into account that users do not hold the handset in a strictly vertical position but declined at various angles.

The RZL measurements were conducted in LOS environments in this study. It should be noted that the RZLs in non-line-of-sight (NLOS) environments are short compared to those in LOS environments in microcell systems with a high-elevation BS both when collinear diversity and polarization-diversity antennas are applied to the BS [4.16].

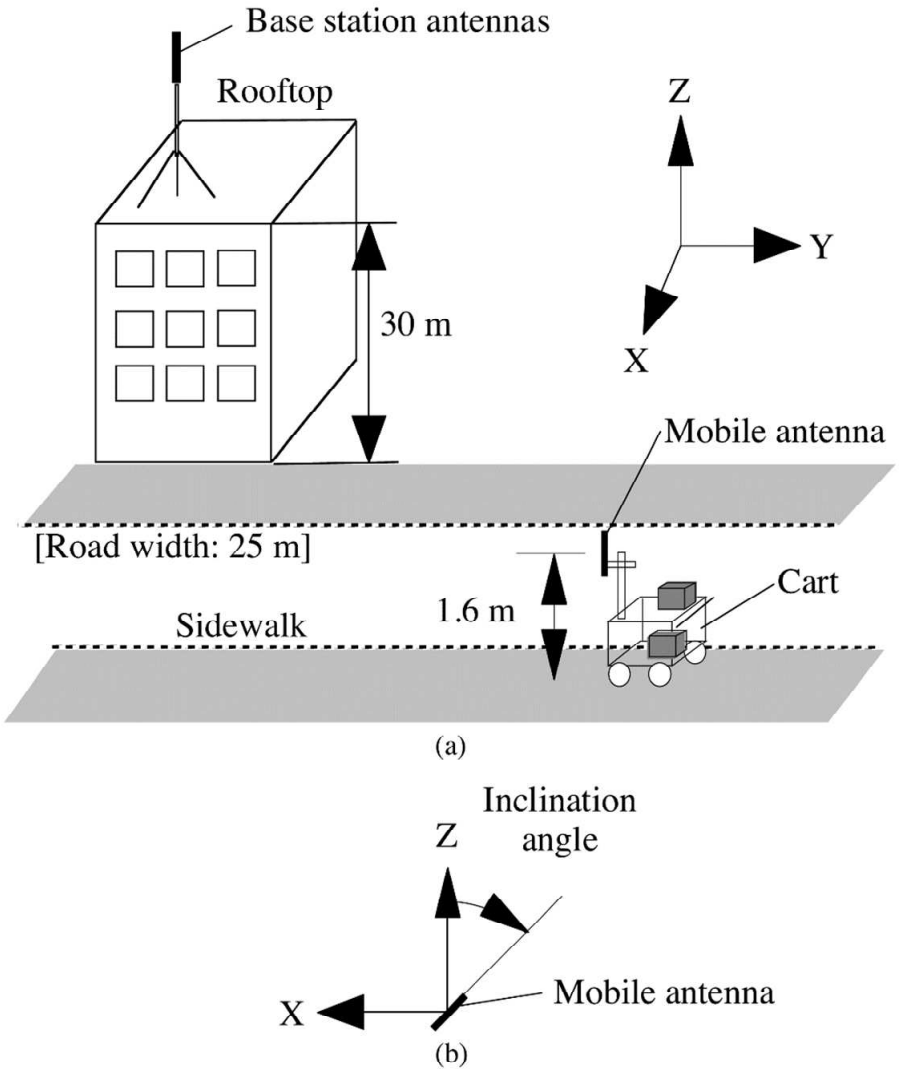

Fig. 4.14 Scenario of RZL measurement in an urban street.
(a) Measurement scenario. (b) Definition of inclination angle.

Fig. 4.15 View from the rooftop where the RZL was measured.

Fig. 4.16 Map of measurement route.

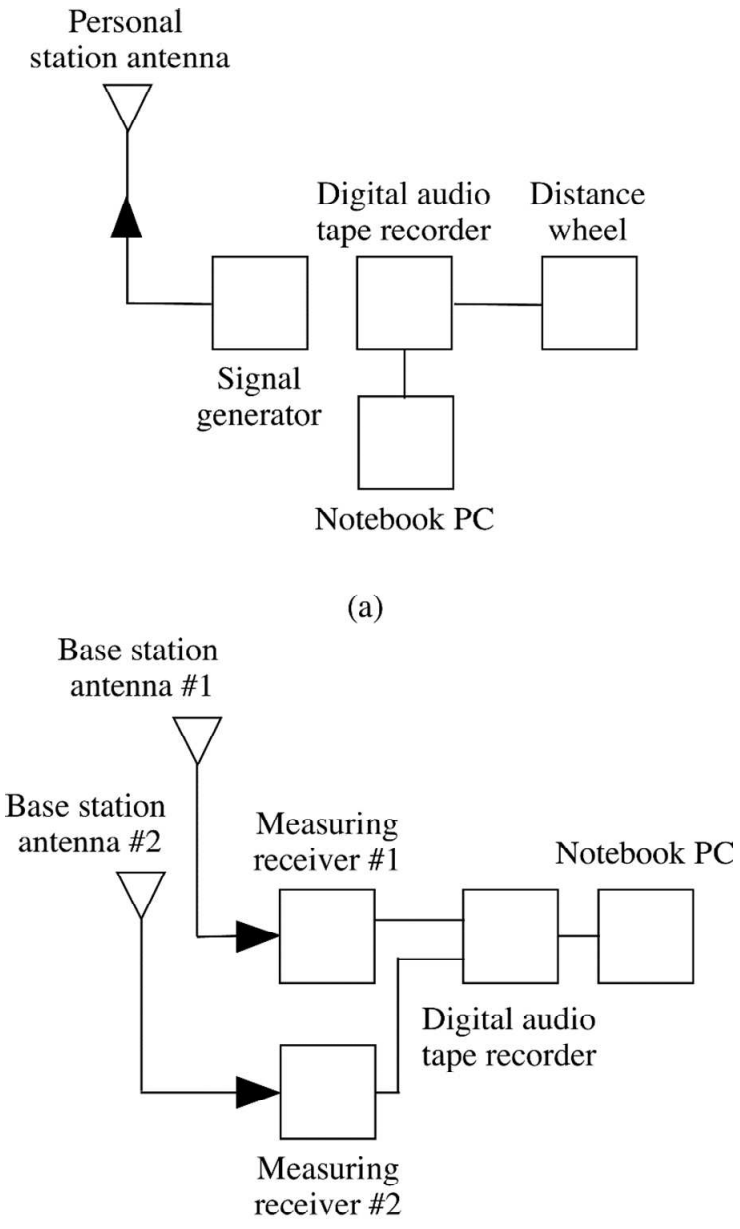

Fig. 4.17 Block diagram of RZL measurement equipment.
(a) Personal station. (b) Base station.

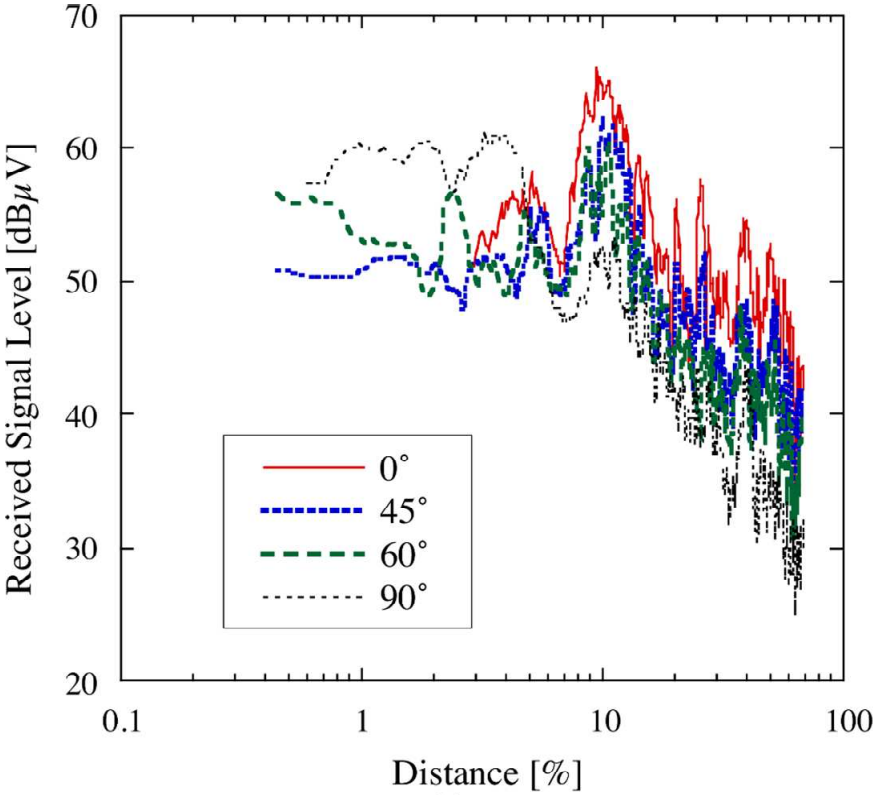

(a) Collinear with no beam tilt (V_antenna)

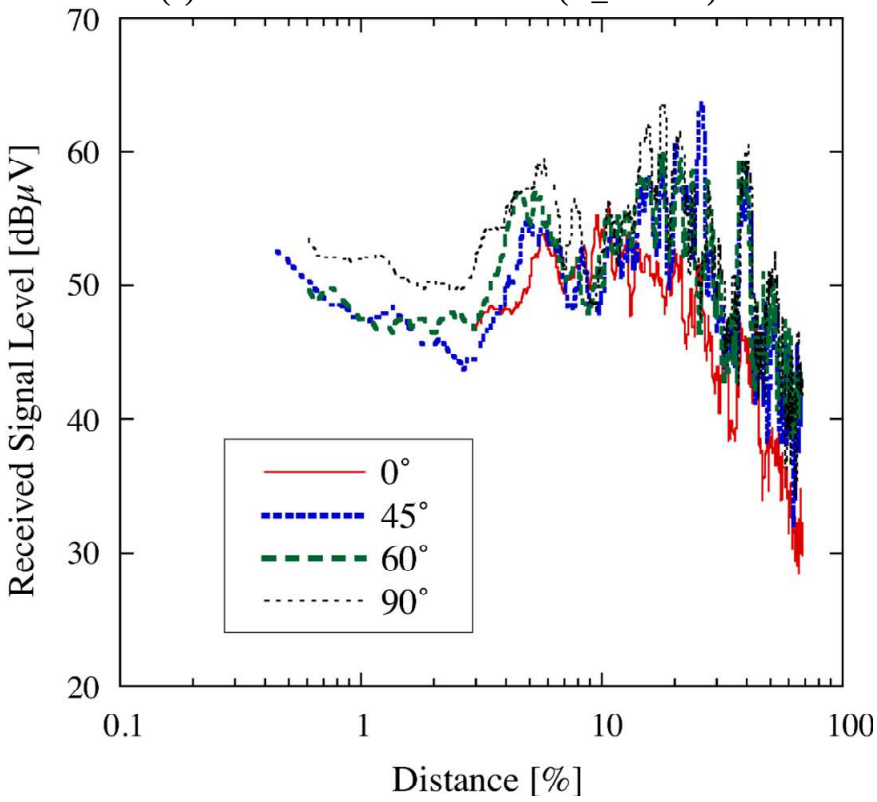

(b) DSCA array with no beam tilt (H_antenna)

Fig. 4.18 Received-signal level.

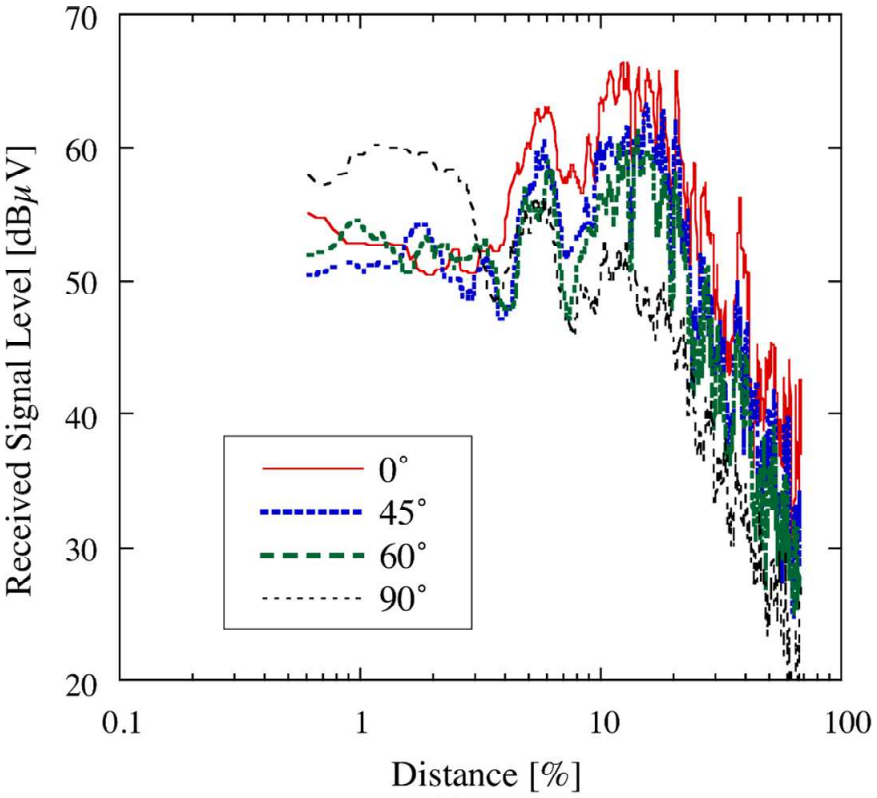

(a) Collinear with no beam tilt (V_antenna)

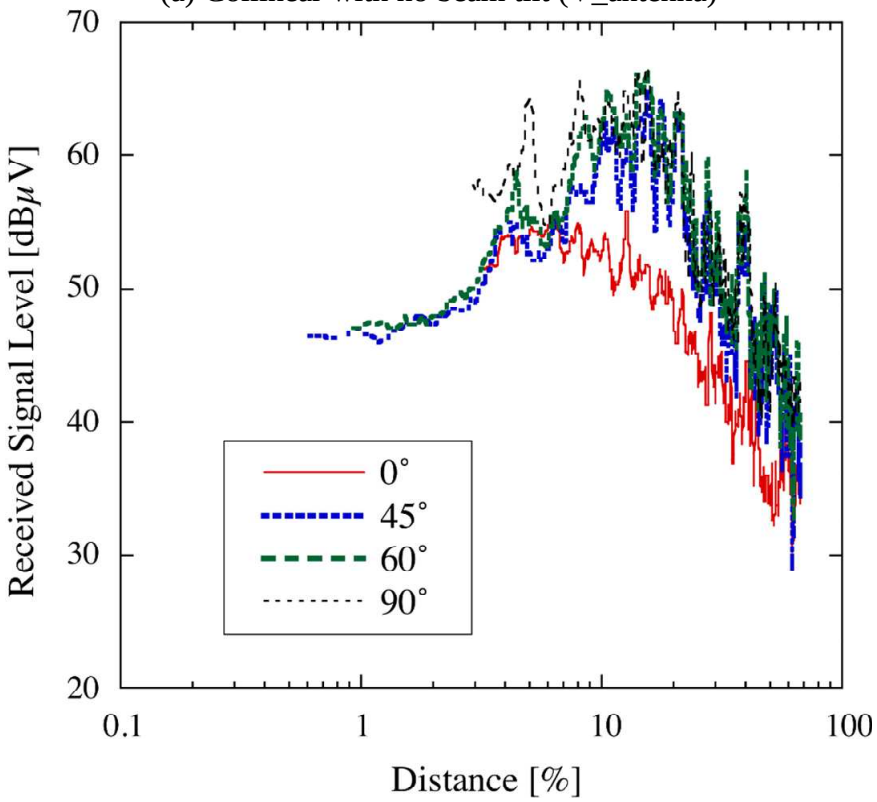

(b) DSCA array with no beam tilt (H_antenna)

Fig. 4.19 Received-signal level.

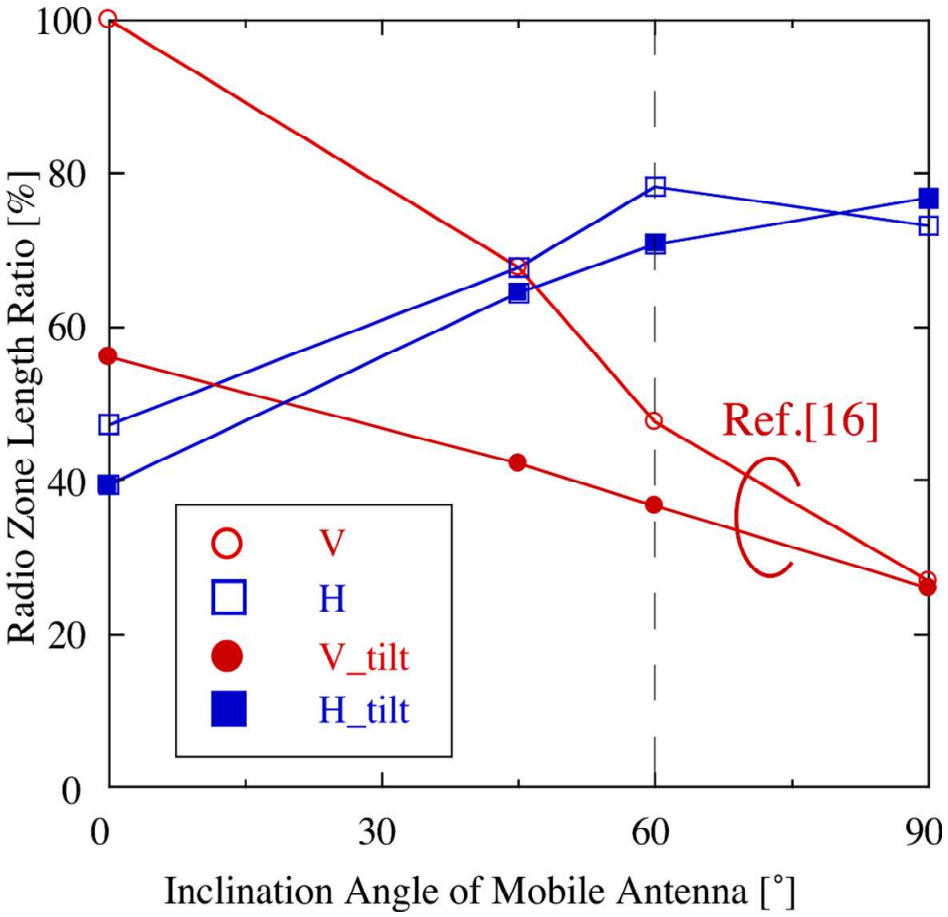

Fig. 4.20 RZLR versus inclination angle of mobile antenna.

Table 4.3 RZLR for four types of diversity antennas.

Diversity Antenna Configuration	Average RZLR [%]	RZLR at 60˚ [%]
V	60.5	47.6
V_tilt	40.2	36.7
H	66.6	78.3
H_tilt	62.8	70.7

Table 4.4 Parameters of regression fitting lines.

(a) V_antenna

Angle[˚]	A	B	Range of Regression Fitting		RZL [m]
			d_1 [m]	d_2 [m]	
0	112.55	24.456	300	630	939
45	86.69	16.708	300	630	636
60	108.52	25.908	300	630	447
90	98.945	24.622	400	630	251

(b) V_tilt_antenna

Angle[˚]	A	B	Range of Regression Fitting		RZL [m]
			d_1 [m]	d_2 [m]	
0	152.81	41.521	200	630	525
45	152.62	43.412	200	630	396
60	153.38	44.744	200	630	345
90	147.71	45.221	200	630	243

(c) H_antenna

Angle[˚]	A	B	Range of Regression Fitting		RZL [m]
			d_1 [m]	d_2 [m]	
0	197.58	59.61	400	630	443
45	124.33	30.13	400	630	637
60	120.69	28.20	400	630	736
90	144.35	36.83	400	630	688

(d) H_tilt_antenna

Angle[˚]	A	B	Range of Regression Fitting		RZL [m]
			d_1 [m]	d_2 [m]	
0	111.12	27.74	200	630	371
45	135.04	34.22	200	630	605
60	138.66	35.01	200	630	664
90	125.22	29.88	200	630	720

4.5 Discussion

The two measurements of the CCI reduction level in Section 4.3 and the RZLs in Section 4.4 show that the DSCA diversity antennas with a beam tilt reduce the CCI level and simultaneously achieve greater RZLs compared to those for collinear antennas. The measurements also demonstrate that the concepts behind the CCI reduction technique for IRBSs set at high elevations using horizontally polarized diversity antennas with beam tilt and a polarization arrangement of BS antennas in a mixed cell architecture function in an orderly fashion in an actual PHS scenario. I developed DSCA array antennas and applied them to the two types of diversity antennas in my chapter: dual-polarized omni-directional diversity antennas [4.16] and the horizontally polarized omni-directional diversity antennas. The reason for using two different types of diversity antennas is that the selection of the diversity antenna configuration depends on the CCI level at the site where the BSs are installed or supposed to be installed. The dual-polarized omni-directional diversity antennas are preferable for the IRBSs where the CCI levels are so low that the IRBS can find an available time slot in the TDMA / TDD scheme and establish a link between the BS and user terminals, while the horizontally polarized omni-directional diversity antennas must be applied to the IRBSs where the CCI levels are too high to find an available time slot in the TDMA / TDD scheme and fail to establish a link between the BS and user terminals.

PHS is not the only wireless mobile system employing the TDD scheme. WiMAX, TD-LTE, TD-SCDMA, and iBurst employ this technology. TDD systems will continue to play a key role and be applied to various wireless systems both now and in the future. Also, the applicability of the CCI reduction technique does not depend on the transmission scheme such as TDD or FDD. Although I investigated the technique only in a mixed-cell PHS environment, clearly this technique using beam tilt and orthogonal polarization is also applicable to systems comprising conventional microcells or macrocells without mixed-cell structures and reduces the CCI level between adjacent cells.

It has not been made clear which radio wave polarization vertical or horizontal exhibits better characteristics in land mobile communication environments. There have been few studies on the issue. The path gain versus distance characteristics for both vertically and horizontally polarized waves is analyzed based on a two-ray model [4.21]. This analysis does not take into account the reflected waves from building walls and therefore is insufficient grounds to explain the advantage of the polarization in multi-path environments such as street microcells. In this chapter, I describe the RZL characteristics for both vertically and horizontally polarized omni-directional diversity BS antennas when the vertically polarized omni-directional mobile antenna was inclined. However, these results do not exactly compare the advantage in polarization between vertically and horizontally polarized waves, because the mobile antenna is a vertically polarized omni-directional antenna. Horizontally polarized omni-directional mobile antennas should be used for horizontally polarized omni-directional diversity BS antennas. The superiority in polarization of radio waves in

land mobile communication systems remains as an important research issue to be addressed in future study.

4.6 Conclusion

This chapter addressed the problem of CCI generated in a mixed cell architecture in PHS adopting the TDMA / TDD scheme by employing horizontally polarized omni-directional diversity antennas that permit the PHS BS antennas established at high elevations to reduce the level of the CCI. In association with the CCI reduction technique using the horizontally polarized diversity antennas in IRBSs, the concept of polarization arrangement of the BS antennas in a mixed cell architecture was introduced. The polarizations in this type of architecture are assigned such that the IRBSs at high elevations separately use horizontally polarized omni-directional antennas with/without beam tilt and the low elevation IBSs use vertically polarized omni-directional antennas with/without beam tilt.

I applied a dielectric-loaded slotted-cylinder antenna (DSCA) to horizontally polarized omni-directional array antennas in a height-diversity configuration with a high gain comparable to that of collinear antennas to reduce the CCI. The measurements of the CCI reduction effect conducted in a suburban area clarified that the DSCA array antennas with beam tilt greatly reduce the CCI level by approximately 23 dB due to the combined effects of both the beam tilt and polarization orthogonal to that of the CCI waves or horizontal polarization. At the same time, the RZL measurements conducted on an urban street identified that the DSCA diversity antennas simultaneously achieve higher RZLs compared to those of collinear antennas. The average RZLRs with respect to the inclination angle of mobile antennas for horizontally polarized omni-directional diversity antennas without/with beam tilt are 66.6 and 62.8%, and greater than those of collinear antennas without/with beam tilt, 60.5 and 40.2%, respectively.

It is concluded that horizontally polarized diversity antennas are superior to vertically polarized diversity antennas or collinear antennas if I take into account that the users do not use handsets in a strictly vertically hand held position but decline the units to various angles. It was demonstrated through measurement that the concepts of the CCI reduction technique for IRBSs set at high elevations using horizontally polarized diversity antennas with beam tilt and a polarization arrangement of BS antennas in a mixed cell architecture are valid and applicable to actual PHS scenarios.

References for chapter 4

[4.1] J. E. Padgett, C. G. Gunther, and T. Hattori, “Overview of wireless personal communications,” IEEE Commun. Mag. Conf., vol. 33, pp. 28-41, Jan. 1995.

[4.2] S. Yan and L. Shiming, “The development analysis of PHS in China,” International Conference on Communications and Mobile Computing, vol. 1, pp. 485-490, Yunnan, Jan. 2009.

[4.3] O. Momtahan and H. Hashemi, “A comparative evaluation of DECT, PACS, and PHS standards for wireless local loop applications,” IEEE Communications Magazine, vol. 39, pp. 156-163, May 2001.

[4.4] Y. Kawahara, H. Hosaka, and K. Sakata, “Positioning system using PHS and a radio beacon for logistics,” Proc. of International Conference on Automation and Logistics, pp. 92-95, Qingdao, Sept. 2008.

[4.5] H. Wang and Q. Chen, “Discussion of ETC online system based on PHS,” Proc. of International Conference on Service Systems and Services Management, vol. 2, pp. 964-965, Chongqing, June 2005.

[4.6] S. Kozono and A. Taguchi, “Mobile propagation loss and delay spread characteristics with a low base station antenna on an urban road,” IEEE Trans. on Vehicular Technology, vol. 42, no. 1, pp. 103-109, Jan. 1993.

[4.7] K. Nishimori, K. Cho, Y. Takatori, and T. Hori, “Two base station configuration using an adaptive array at elevated locations for microcell systems,” IEICE Trans. Commun., vol. E83-B, No. 8, pp. 1688-1696, August 2000.

[4.8] G. V. Tsoulos, M. A. Beach, and S. C. Swales, “Application of adaptive antenna technology to third generation mixed cell radio architectures,” IEEE VTC’94, vol. 1, pp. 615-619, Stockholm, June 1994.

[4.9] K. Fujimoto and J. R. James, Mobile Antenna Systems Handbook, Boston: Artech House, 1994, pp. 137-140.

[4.10] J. Niemelä and J. Lempiäinen, “Impact of mechanical antenna downtilt on performance of WCDMA cellular network,” IEEE VTC 2004-Spring, vol. 4, pp. 2091-2095, Milan, May 2004.

[4.11] M. Pettersen, L. E. Bråten, and A. G. Spilling, “Automatic antenna tilt control for capacity enhancement in UMTS FDD,” IEEE VTC 2004-Fall, vol. 1, pp. 280-284, Los Angeles, Sept. 2004.

[4.12] M. Garcia-Lozano and S. Ruiz, “Effects of downtilting on RRM parameters,” IEEE PIMRC'04, vol. 3, pp. 2166-2170, Barcelona, Sept. 2004.

[4.13] I. Siomina, “P-CPICh power and antenna tilt optimization in UMTS networks,” Proc. of advanced industrial conference on telecommunications/service assurance with partial and intermittent resources conference/e-learning on telecommunications workshop (AICT/SAPIR/ELETE-2005), pp. 268-273, Lisbon, July 2005.

[4.14] Y. Akaiwa, H. Andoh, and T. Kohama, “Autonomous decentralized inter-base-station

synchronization for TDMA microcellular systems," IEEE VTC'91, pp. 257-262, St. Louis, May 1991.
[4.15] S. Ariyavisitakul, R. C. Lau, and H. W. Arnold, "Network synchronization of radio ports in wireless personal communications," IEE Electronics Letters, vol. 28, No. 25, pp. 2312-2314, Dec. 1992.
[4.16] A. Ando, A. Kondo, and S. Kubota, "A study of radio zone length of dual-polarized omnidirectional antennas mounted on rooftop for personal handy-phone system," IEEE Trans. on Vehicular Technology, vol. 57, no. 1, pp. 2-10, Jan. 2008.
[4.17] K. Cho, T. Hori, and K. Kagoshima, "Effectiveness of four-branch height and polarization diversity configuration for street microcell," IEEE Trans. on Antennas and Propagation, vol. AP-46, No. 6, pp. 776-781, June 1998.
[4.18] T. Taga and K. Tsunekawa, "Performance analysis of a built-in planar inverted F antenna for 800 MHz band portable radio units," IEEE Journal on Selected Areas in Communications, vol. SAC-5, No. 5, pp. 921-929, June 1987.
[4.19] A. Ando, Y. Honma, and K. Kagoshima, "An electromagnetically coupled microstrip antenna with a rotatable patch," Proc. on the IEEE Int. Symp. on Antennas Propagation (IEEE AP-S), vol. 1, pp. 18-23, New Port Beach, June 1995.
[4.20] T. Taga and K. Tsunekawa, "A built-in antenna for 800 MHz band portable radio units," Proc. Int. Symp. Ant. Propagat. (ISAP), pp. 425-428, Kyoto, August 1985.
[4.21] H. L. Bertoni, Radio Propagation for Modern Wireless Systems, Upper Saddle River: Prentice Hall, 2000, pp. 96-98.

Chapter 5

Estimation Method for Extraction and Reinjection-Type Interference Canceller

5. Estimation Method for Extraction and Reinjection-Type Interference Canceller

5.1 Introduction

As radio communication systems advance, the number of users simultaneously using the same frequency band in the same area will steadily increase. As a result, interference has become a key problem in maintaining a high level of quality. Using an interference canceller can clear interference positively. This technology has been pursued mainly in the fields of microwave and satellite communication systems, and many interference cancellers has been developed [5.1]-[5.5].

Interference cancellation technique is applied for the next generation mobile communications system (5G). Multi–antenna Interference Rejection Combining (IRC) and Massive Multiple-Input Multiple-Output (MIMO) are studied in order to increase the number of users who use mobile Internet access [5.6], [5.7].

An Extraction and reinjection-type interference canceller (ERIC) has been previously proposed which has more advantages than other cancellers from the view point of applicability under various interference conditions [5.4]. The ERIC extracts interference signals from received signals, and cancels interference using these extracted signals. Therefore, it compensates for interference without obtaining a clean reference signal and without regard to the band of the interference signal. However, to what degree the ERIC can cancel the interference when fading occurs has not yet been determined due to fluctuations in the power level of the extracted interference signal. In order to determine the applicability of ERIC, it is necessary to clarify its performance level for interference cancellation under these conditions.

This chapter proposes a method for estimating ERIC's performance. Next, this canceller is divided into interference extraction and interference cancellation parts, and calculated performance results are confirmed through experiments. Finally, I estimate the degree of improvement in interference cancellation when using this device under fading conditions. In general, interference becomes a severe problem when power ratio D/U degrades because the received power of the desired signal drops to a level below its steady state even though the interference signal remains constant. Due to this, in this chapter I assume that under flat fading conditions, the amplitude and phase of the received signal varies uniformly in-band regardless of the signal's frequency characteristics.

5.2 Theoretical Investigation for Interference Cancelling

Figure 5.1 shows the analytical model of this canceller. One desired signal and one interference signal are received at both the main antenna and sub antenna. In addition, thermal noise is present in each received signal. Thus, signal $\boldsymbol{X}_{\mathbf{m}}$ received at the main antenna and $\boldsymbol{X}_{\mathbf{s}}$ received at the sub antenna are expressed as

$$\boldsymbol{X}_{\mathbf{m}} = \boldsymbol{D}_{\mathbf{m}} + \boldsymbol{U}_{\mathbf{m}} + \boldsymbol{N}_{\mathbf{m}}, \tag{5.1}$$

$$\boldsymbol{X}_{\mathbf{s}} = \boldsymbol{D}_{\mathbf{s}} + \boldsymbol{U}_{\mathbf{s}} + \boldsymbol{N}_{\mathbf{s}}, \tag{5.2}$$

Where $\boldsymbol{D}_{\mathbf{m}}$ and $\boldsymbol{D}_{\mathbf{s}}$ are the desired signals, $\boldsymbol{U}_{\mathbf{m}}$ and $\boldsymbol{U}_{\mathbf{s}}$ are the interference signals, $\boldsymbol{N}_{\mathbf{m}}$ and $\boldsymbol{N}_{\mathbf{s}}$ are the thermal noise components. For signals with a broadband, multiple variable amplitude-and-phase circuits will be required in both the interference extraction part and the interference cancellation part due to such signals' frequency characteristics. Without such characteristics, the maximum effect for interference cancellation in using multiple variable amplitude-and-phase circuits is equal to using just one of these circuits. This chapter treats the case where only one of these circuits exists in each part.

Even though ERIC can universally applied to various digital modulation schemes, signal frequency characteristics, as previously stated in the Introduction, do not need to be considered because of flat fading. Therefore, I express each signal in the following equations using carrier angular frequency ω as:

$$\boldsymbol{D}_{\mathbf{m}} = D_{\mathrm{m}} \exp[\, \boldsymbol{j}(\omega t + \theta_{\mathrm{m}})], \tag{5.3}$$

$$\boldsymbol{D}_{\mathbf{s}} = D_{\mathrm{s}} \exp[\, \boldsymbol{j}(\omega t + \theta_{\mathrm{s}})], \tag{5.4}$$

$$\boldsymbol{U}_{\mathbf{m}} = U_{\mathrm{m}} \exp[\, \boldsymbol{j}(\omega t + \phi_{\mathrm{m}})], \tag{5.5}$$

$$\boldsymbol{U}_{\mathbf{s}} = U_{\mathrm{s}} \exp[\, \boldsymbol{j}(\omega t + \phi_{\mathrm{s}})], \tag{5.6}$$

where D_{m}, D_{s}, U_{m} and U_{s} are the amplitudes, and θ_{m}, θ_{s}, ϕ_{m} and ϕ_{s} are the phase of each signal.

An in-phase space diversity (SD) combiner combines received signals $\boldsymbol{X}_{\mathbf{m}}$ and $\boldsymbol{X}_{\mathbf{s}}$ so that the two signals are in-phase and the combined power is a maximum for phase Ψ of the phase shifter. The phase shift of the SD combiner is given as

$$\Psi = \mathrm{Arg}(\boldsymbol{X}_{\mathbf{m}}) - \mathrm{Arg}(\boldsymbol{X}_{\mathbf{s}}). \tag{5.7}$$

The combined signal $\boldsymbol{X}_{\mathbf{sd}}$ is

$$\begin{aligned} \boldsymbol{X}_{\mathbf{sd}} &= \boldsymbol{X}_{\mathbf{m}} + \boldsymbol{X}_{\mathbf{s}} \exp[\, \boldsymbol{j}\Psi] \\ &= \boldsymbol{D}_{\mathbf{sd}} + \boldsymbol{U}_{\mathbf{sd}} + \boldsymbol{N}_{\mathbf{sd}}, \end{aligned} \tag{5.8}$$

where $\boldsymbol{X}_{\mathbf{sd}}$ consists of the desired signal, $\boldsymbol{D}_{\mathbf{sd}}$; the interference signal, $\boldsymbol{U}_{\mathbf{sd}}$; and thermal noise $\boldsymbol{N}_{\mathbf{sd}}$.

$\boldsymbol{X}_{\mathbf{m}}$ and $\boldsymbol{X}_{\mathbf{s}}$ branch prior to the SD combiner and are input into the interference extraction part. $\boldsymbol{X}_{\mathbf{s}}$ is multiplied by a complex weight, $\boldsymbol{C}$, and is added to the $\boldsymbol{X}_{\mathbf{m}}$. The resulting output signal, $\boldsymbol{Y}_{\mathbf{ex}}$ is written as

$$\boldsymbol{Y}_{\mathbf{ex}} = \boldsymbol{X}_{\mathbf{m}} - \boldsymbol{C}\, \boldsymbol{X}_{\mathbf{s}}. \tag{5.9}$$

The optimum weight, $\boldsymbol{C}_{\mathrm{opt}}$, can be determined by detecting the correlation between $\boldsymbol{Y}_{\mathbf{ex}}$ and $\boldsymbol{X}_{\mathbf{s}}$, as described in detail in the Appendix at the end of this chapter,

$$\boldsymbol{C}_{\mathrm{opt}} = \frac{D_{\mathrm{m}} D_{\mathrm{s}} \exp[\boldsymbol{j}(\theta_{\mathrm{m}} - \theta_{\mathrm{s}})] + U_{\mathrm{m}} U_{\mathrm{s}} \exp[\boldsymbol{j}(\varphi_{\mathrm{m}} - \varphi_{\mathrm{s}})]}{D_{\mathrm{s}}^{\,2} + U_{\mathrm{s}}^{\,2} + N_{\mathrm{s}}^{\,2}}. \tag{5.10}$$

The output signal of the interference extraction part, $\boldsymbol{Y}_{\mathbf{ex}}$, is rewritten as

$$\begin{aligned} \boldsymbol{Y}_{\mathbf{ex}} &= \boldsymbol{D}_{\mathbf{m}} + \boldsymbol{U}_{\mathbf{m}} + \boldsymbol{N}_{\mathbf{m}} - \boldsymbol{C}_{\mathrm{opt}} (\boldsymbol{D}_{\mathbf{s}} + \boldsymbol{U}_{\mathbf{s}} + \boldsymbol{N}_{\mathbf{s}}) \\ &= \boldsymbol{D}_{\mathbf{ex}} + \boldsymbol{U}_{\mathbf{ex}} + \boldsymbol{N}_{\mathbf{ex}}, \end{aligned} \tag{5.11}$$

where $\boldsymbol{D}_{\mathbf{ex}}$ is the desired signal, $\boldsymbol{U}_{\mathbf{sd}}$ is the interference signal, and $\boldsymbol{N}_{\mathbf{sd}}$ is the thermal noise.

Using these terms, I define *extraction UDNR* as

$$extraction\,UDNR = \frac{U_{ex}^{\ 2}}{D_{ex}^{\ 2} + N_{ex}^{\ 2}}, \tag{5.12}$$

which expresses the numerical value of the interference extraction effect. The ERIC's interference-canceling performance level is sensitive to the power of the interference signal at the output of the interference extraction part, that is, extraction UDNR as a parameter for evaluating the performance.

Next the output signal of the SD combiner, $\boldsymbol{X_{sd}}$, and the output signal of the interference extraction part, $\boldsymbol{Y_{ex}}$, are input into the interference cancellation part. Then remaining desired signal $\boldsymbol{D_{ex}}$ is assumed to be noise because it becomes a degrading factor in the interference cancellation. Therefore, $\boldsymbol{Y_{ex}}$ changes to $\boldsymbol{X_{ex}}$, i.e.,

$$\begin{aligned} \boldsymbol{Y_{ex}} &= \boldsymbol{D_{ex}} + \boldsymbol{U_{ex}} + \boldsymbol{N_{ex}} \\ &= \boldsymbol{X_{ex}} = \boldsymbol{U_{ex}} + \boldsymbol{N_{ex}}', \end{aligned} \tag{5.13}$$

where

$$\boldsymbol{N_{ex}}' = \boldsymbol{D_{ex}} + \boldsymbol{N_{ex}}.$$

In the interference cancellation part, $\boldsymbol{X_{ex}}$ is multiplied by complex weight $\boldsymbol{W}$ and added to $\boldsymbol{X_{sd}}$. Consequently, the output signal is given as

$$\begin{aligned} \boldsymbol{Y_c} &= \boldsymbol{X_{sd}} - \boldsymbol{W}\,\boldsymbol{X_{ex}} \\ &= \boldsymbol{D_c} + \boldsymbol{U_c} + \boldsymbol{N_c}, \end{aligned} \tag{5.14}$$

where $\boldsymbol{D_c}$ is the desired signal, $\boldsymbol{U_c}$ is the interference signal, and $\boldsymbol{N_c}$ is the thermal noise. Similarly to Eq. (5.10), $\boldsymbol{W}_{opt}$ is expressed as

$$\boldsymbol{W}_{opt} = \frac{U_{sd}U_{ex}\exp[\boldsymbol{j}(\phi_{sd} - \phi_{ex})]}{U_{ex}^{\ 2} + N_{ex}'^{2}}, \tag{5.15}$$

where ϕ_{sd} is the phase of interference signal $\boldsymbol{U_{sd}}$ and ϕ_{ex} is the phase of interference signal $\boldsymbol{U_{ex}}$.

I define an improvement factor, α, which indicates the difference in power rate $D/(U+N)$ with and without this canceller,

$$\alpha \equiv \frac{D_c^{\ 2}}{U_c^{\ 2} + N_c^{\ 2}} \Bigg/ \frac{D_{sd}^{\ 2}}{U_{sd}^{\ 2} + N_{sd}^{\ 2}}. \tag{5.16}$$

The factor α can be calculated and expressed as

$$\alpha = \left\{ 1 - \frac{1}{\left(U_{ex}^{\ 2}/N_{ex}'^{2}\right)^{-2} + 1} \frac{1}{\left(U_{sd}^{\ 2}/N_{sd}^{\ 2}\right)^{-2} + 1} \right\}^{-1}. \tag{5.17}$$

Thus, I can estimate the improvement in interference cancellation for the ERIC by using this derived improvement factor, α. From Eq. (5.12) and Eq. (5.13), α is dependent on the *extraction UDNR*.

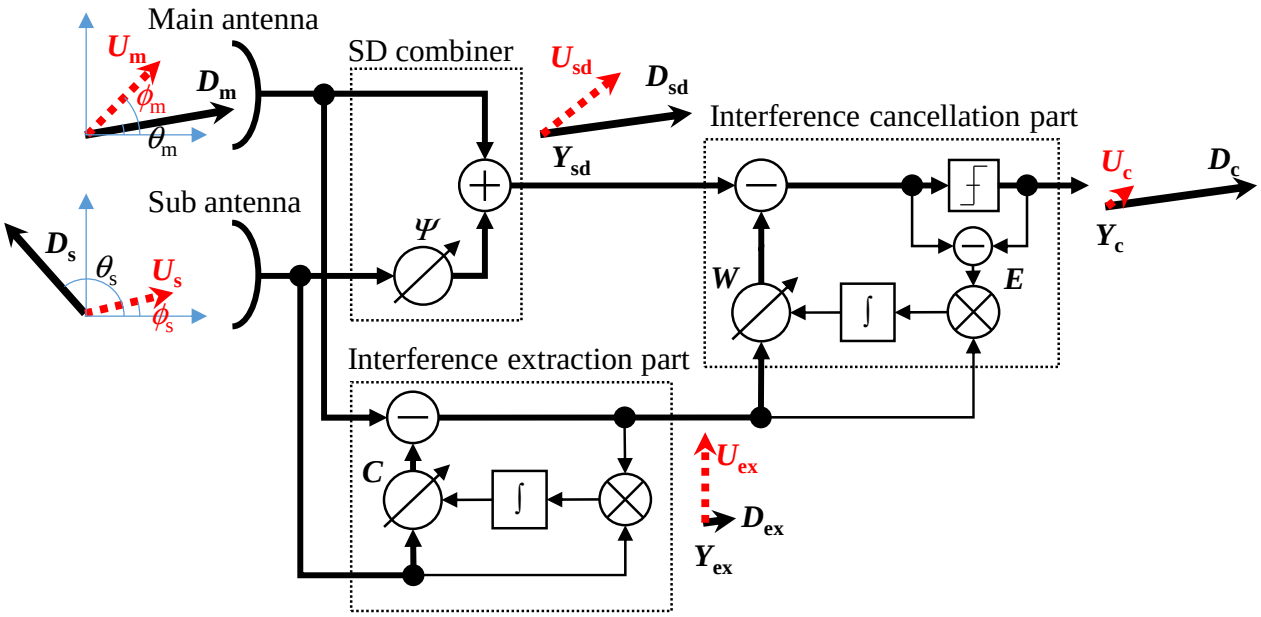

Fig. 5.1 Extraction and Reinjection-Type Interference Canceller configuration for theoretical investigation.

5.3 Interference Extraction Performance

With regard to *extraction UDNR* obtained in Section 5.2, this section shows typical estimation and experimental results. Due to the fact that the actual canceller is operated with digital signal processing, I calculate to the accuracy of 8-bit quantization. Figure 5.2 shows *extraction UDNR* versus power ratio D_m/U_m, which equals D_s/U_s. Here, the phases of the desired signal at the main antenna and the sub antenna are $\theta_m = 0^\circ$ and $\theta_s = 150^\circ$, respectively, and those of the interference signal at the main antenna and the sub antenna are $\phi_m = 30^\circ$ and $\phi_s = 0^\circ$, respectively. The amplitudes of the desired signal and thermal noise are constant, and those of the interference signal are variable.

Figure 5.2 shows two important points. The first is that *extraction UDNR* increases with D_m/U_m (= D_s/U_s), when they are nearly 0 dB. This is because when the power of U_s cannot be regarded as negligible compared with that of D_s, then the desired signal cannot be cancelled sufficiently; therefore, it remains. However, as the power level of the interference signal decreases, its influence on the correlation detection of the desired signal gradually decreases and thus the desired signal can be adequately suppressed, and as a result the interference signal can be extracted and *extraction UDNR* increases proportionally with D_m/U_m (= D_s/U_s).

The other important point is that *extraction UDNR* begins to decrease proportionally as D_m/U_m (= D_s/U_s) increases from a specific point. The reason is that the suppression of the desired signal reaches its maximum level due to the influence of the thermal noise and quantization noise but not due to the interference signal, and the power level of the extracted interference signal decreases as the level of the received interference signal decreases.

Due to these two points, *extraction UDNR* has a peak [5.8], [5.9]. For example, at D_m/U_m (= D_s/U_s) = 40 dB in Fig. 5.2, its peak of 16 dB is obtained at D_m/U_m (= D_s/U_s) = 20 dB.

To verify the performance of the interference extraction, an experiment was carried out using a 16-QAM signal with a bit capacity of 51.84 Mbps as the desired signal and a CW signal as the interference signal. In this experiment, the ratio of the desired signal power to the interference signal power was the same for the two interference extraction part inputs, i.e., $D_m/U_m = D_s/U_s$. In addition, the ratio of the desired signal power to the noise power was the same, i.e., $D_m/N_m = D_s/N_s$, and the phase difference of the interference is opposite to that of the desired signal. Figure 5.2 show the experimental results of *extraction UDNR* versus D_m/U_m (= D_s/U_s) for the two cases where D_m/N_m (= D_s/N_s) = 20 dB and 30 dB. These results conform closely to the estimated results.

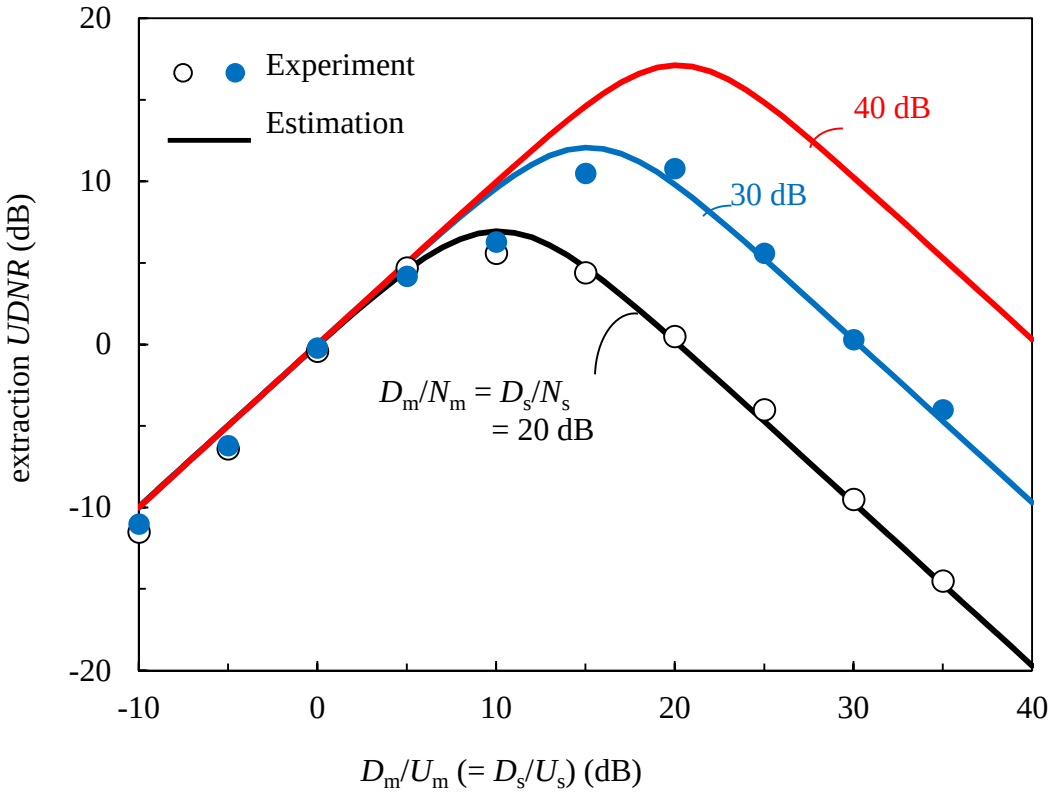

Fig. 5.2 Interference extraction performance extraction *UDNR* vs Dm/Um (= Ds/Us) (θm = 0°, θs = 150°, ϕm = 30°, ϕs = 0°).

5.4 Interference Cancellation Performance

From Eq. (5.12) and Eq. (5.17) a relationship between improvement factor α and *extraction UDNR* can be explained as follows. Figure 5.3 shows the improvement factor α versus *extraction UDNR* for the two cases where power rate U_{sd}/N_{sd} = 5 dB and 10 dB. When the interference signal can be extracted to a greater extent than the noise in the interference extraction pat, that is where *extraction UDNR* >0 dB, then α is increased with *extraction UDNR*, and achieves a rate close to that of power rate U_{sd}/N_{sd}. However, when the extracted interference signal is below the noise level, then α becomes 0 dB.

To verify this performance level of interference cancellation, I performed an experiment using the same signals in Section 5.3. In this experiment, I defined an improvement factor in interference cancellation as the difference in power ratio D_{sd}/U_{sd} at a BER of 10^{-4} with and without this canceller, Figure 5.3 indicates that the experimental results confirm the estimation shown in Eq. (5.17). For example, with *extraction UDNR* = 15 dB, I have improvement factor α = 5.8 dB for U_{sd}/N_{sd} = 5dB and α = 9.3 dB for U_{sd}/N_{sd} = 10 dB.

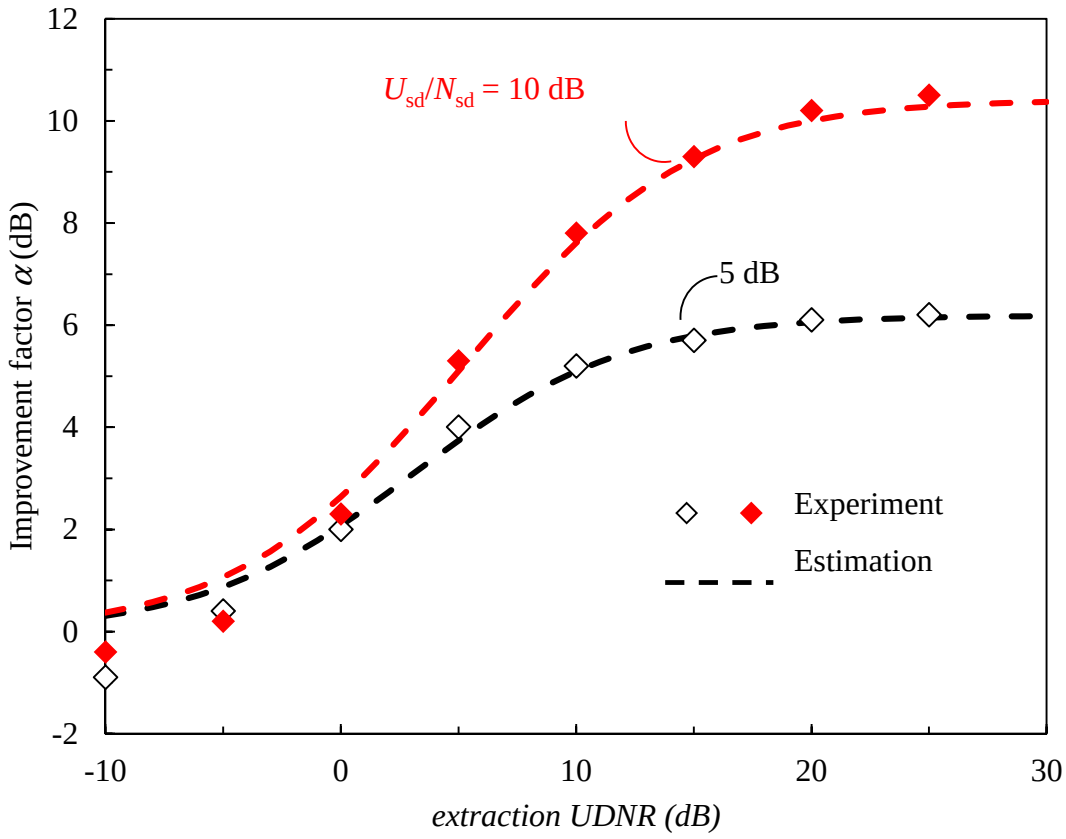

Fig. 5.3 Interference cancellation performance improvement factor α vs *extraction UDNR* for various U_{sd}/N_{sd}.

5.5 Improvement Effect of Interference Cancellation

In Section 5.4, it can be confirmed that the improvement factor is dependent on *extraction UDNR*. On the other hand, in Section 5.3, I can see that *extraction UDNR* is varied according to the power rate between the desired signal and the interference signal, and the phase difference between these two received signals. These transmission conditions fluctuate violently in a fading environment. This section describes the simulations I performed so that the improvement of the interference cancellation using the ERIC during fading can be estimated.

Table 5.1 shows simulation conditions where the received power distribution of the desired signal is given by Rayleigh distribution and that of the interference signal is given by constant distribution. This is because the propagation path of the desired signal is different from that of the interference signal and both signals have no correlation [5.8]. In general, problems involving interference become more severe when the received power level of the desired signal is attenuated due to fading; however, the received power level of the interference signal remains constant.

Figure 5.4 shows the distribution of *extraction UDNR* under the conditions indicated in Table 5.1 using, as a parameter, the average of power rate D/U for received signals, D_m/U_m and D_s/U_s. Here, D_m/N_m (= D_s/N_s) is set at 40 dB. It is clarified that the high power level of the extracted interference signal is obtained most frequently when D/U is 20 dB.

Figure 5.5 shows the cumulative distributions of power rate $D/(U+N)$ for the SD combiner output signal and the ERIC output signal for each case. The maximum improvement effect using the ERIC compared with the SD combiner is 2.6, 7.5, and 1.4 times for 10 dB, 20 dB, and 40 dB, respectively. ERIC is the most valid when the average of power rate D/U in received signals is 20 dB. The reason for this is that the probability of extracting the interference signal is largest when D/U = 20 dB.

Table 5.1 Simulation conditions.

	Desired signal	Interference signal
Received power distribution	Rayleigh	Constant
Phase distribution	Uniform	
Space correlation coefficient	0.5	1.0

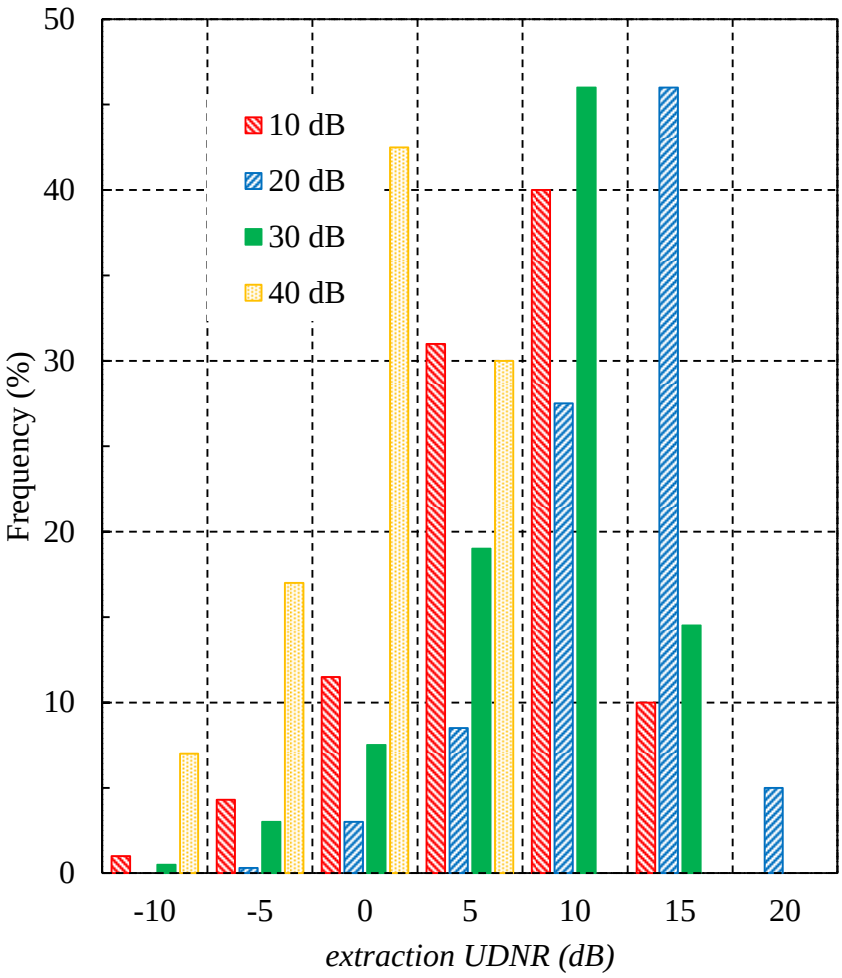

Fig. 5.4 Distribution of *extraction UDNR* (D_m/N_m (= D_s/N_s) = 40 dB).

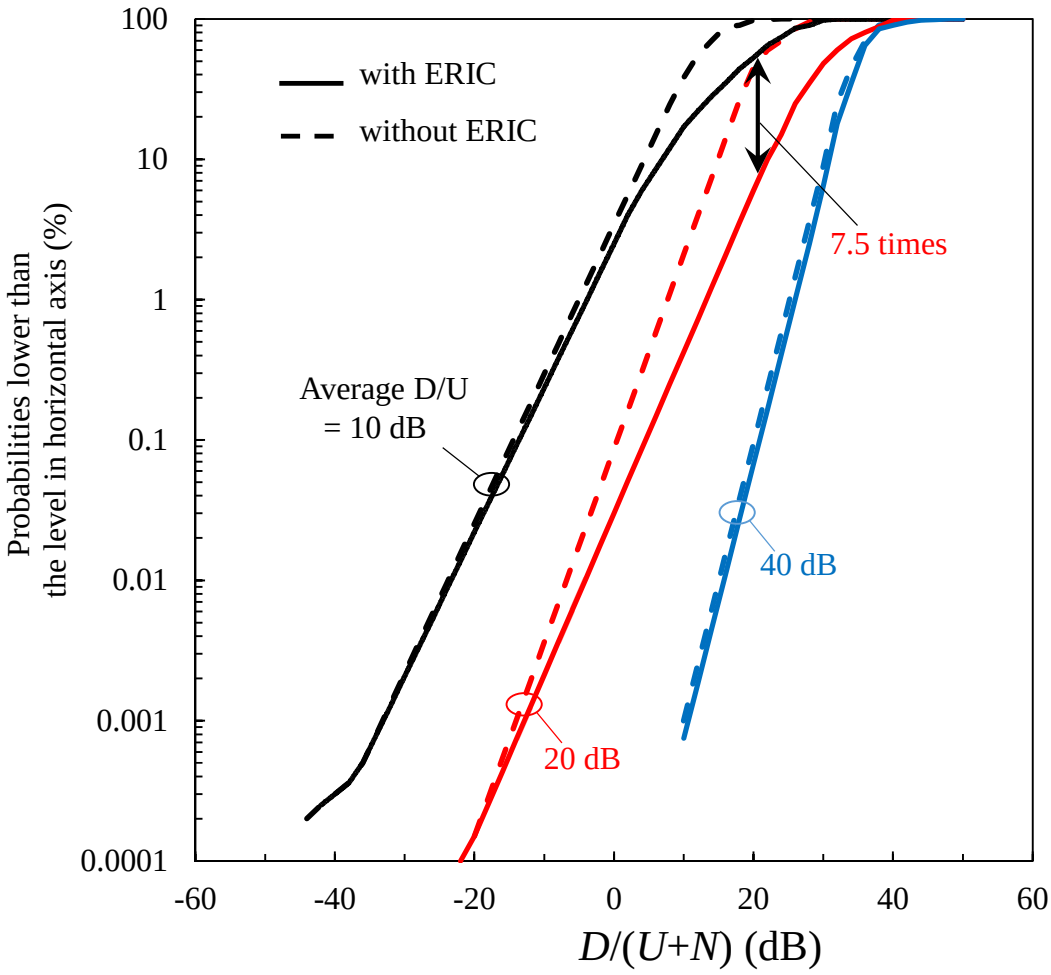

Fig. 5.5 Improvement of $D/(U+N)$ in fading environments using ERIC (D_m/N_m (= D_s/N_s) = 40 dB).

5.6 Conclusion

Theoretical evaluation is performed on the ERIC's performance level for interference cancellation. As a result, it can be clarified that the improvement factor of cancellation is dependent on the power level of the extracted interference signal. This level's upper bound is varied according to power rate D/U in received signals and the phase difference between the desired signals and the interference signals. As an example, when the power level of the interference signals is 15 dB, an improvement factor of 9.3 dB can be obtained. It is confirmed that theoretical estimations agree closely with the experimental results. Moreover, it is clarified through simulations that this canceller is the most valid when the average of power rate D/U in received signals is 20 dB. In a fading environment, and the maximum improvement effect using this canceller is 7.5 times better than without using the canceller. Further investigations will be done on the effects of this canceller in a fading environment through experiments on an actual propagation path, in order to ensure the validity of this estimation method.

References for chapter 5

[5.1] T. Kaitsuka and T. Inoue, "Interference cancellation system for satellite communication Earth station," IEEE Trans. On Comm., vol. COM-32, no.7, July 1984.

[5.2] H. Matsue and T. Murase, "Vector Correlation Detection Type Interference Canceller," IEEE GCOM'87, vol.1, pp. 1233-1238, Nov. 1987.

[5.3] J. Namiki, "FM Interference Elimination Systems for Digital Microwave Transmission," IEICE Trans. Commun., vol. J64-B, No. 6, pp.505-512, June 1981.

[5.4] K. Watanabe, H. Matsue, and T. Murase, "Extraction and Reinjection-type Interference Canceller," IEICE Trans. Commun., vol. J74-B-II, No. 9, pp.469-478, Sept. 1991.

[5.5] K. Watanabe, S. Uwano, and H. Matsue, "Pre-Interference Canceller for Digital Microwave Radio Systems," IEICE Trans. Commun., vol. J77-B-II, No. 7, pp.359-366, July 1994.

[5.6] Y. Ohwatari, N. Miki, T. Asai, T. Abe, and H. Taoka, "Performance of Advanced Receiver Employing Interference Rejection Combining to Suppress Inter-Cell Interference in LTE-Advanced Downlink," IEEE VTC 2011-Fall, pp. 1-7, Sept. 2011.

[5.7] T. L. Marzetta, "Noncooperative cellular wireless with unlimited numbers of base station antennas," IEEE Trans. on Wireless Communications, vol. 9, No. 11, pp. 3590–3600, Nov. 2010.

[5.8] R. T. Compton, Jr., "The power-inversion adaptive array: concept and performance," IEEE Trans. on Aerospace and Electronic Systems, vol. AES-15, No. 6, pp.803-814, Nov. 1979.

[5.9] S. Uwano and K. Watanabe, "Analysis and experiment of interference extraction performance on extraction and reinjection-type interference canceller," IEICE Comm. National Conf., B-497, April 1994.

[5.10] S. Uwano and K. Watanabe, "Path correlation of fading occurrence in interference

cancellation," IEICE Comm. National Conf., B-530, April 1995.

Appendix

The optimum weight $\boldsymbol{C}_{\text{opt}}$ and $\boldsymbol{W}_{\text{opt}}$, at the interference extraction part and the interference cancellation part, respectively, are determined as follows. At the interference extraction part by detecting the correlation between $\boldsymbol{Y}_{\mathbf{ex}}$ and $\boldsymbol{X}_{\mathbf{s}}$, in other words, by multiplexing $\boldsymbol{Y}_{\mathbf{ex}}$ by $\boldsymbol{X}_{\mathbf{s}}^{*}$ (* denoted the complex conjugate), taking a time integral, and setting the equation to zero, the following expression is obtained

$$\int \boldsymbol{X}_{\mathbf{s}}^{*} \cdot \boldsymbol{Y}_{\mathbf{ex}} dt = 0 . \tag{5.18}$$

The optimum weight, $\boldsymbol{C}_{\text{opt}}$, can be obtained from (5.1), (5.2), (5.9), and (5.18).

$$\boldsymbol{C}_{\text{opt}} = \int \boldsymbol{X}_{\mathbf{s}}^{*} \cdot \boldsymbol{X}_{\mathbf{m}} dt \Big/ \int \boldsymbol{X}_{\mathbf{s}}^{*} \cdot \boldsymbol{X}_{\mathbf{s}} dt . \tag{5.19}$$

From (5.3)-(5.6), $\boldsymbol{C}_{\text{opt}}$ results in (5.10) by using following correlation functions:

$$\int \boldsymbol{D}_{\mathbf{s}}^{*} \cdot \boldsymbol{D}_{\mathbf{m}} dt = D_{\text{m}} D_{\text{s}} \exp[\boldsymbol{j}(\theta_{\text{m}} - \theta_{\text{s}})],$$

$$\int \boldsymbol{U}_{\mathbf{s}}^{*} \cdot \boldsymbol{U}_{\mathbf{m}} dt = U_{\text{m}} U_{\text{s}} \exp[\boldsymbol{j}(\phi_{\text{m}} - \phi_{\text{s}})],$$

$$\int \boldsymbol{U}_{\mathbf{s}}^{*} \cdot \boldsymbol{D}_{\mathbf{m}} dt = 0,$$

$$\int \boldsymbol{N}_{\mathbf{s}}^{*} \cdot \boldsymbol{N}_{\mathbf{m}} dt = 0 . \tag{5.20}$$

On the other hand, by passing $\boldsymbol{Y}_{\mathbf{c}}$ through a detection circuit at the interference cancellation part, the following error signal is obtained by taking the difference between the input and output of each component:

$$\boldsymbol{E} = \boldsymbol{Y}_{\mathbf{c}} - \boldsymbol{D}_{\mathbf{sd}}. \tag{5.21}$$

Using the correlation detection between $\boldsymbol{E}$ and $\boldsymbol{X}_{\mathbf{ex}}$, the optimum weight, $\boldsymbol{W}_{\text{opt}}$, is given as (5.15), similarly to $\boldsymbol{C}_{\text{opt}}$.

Chapter 6

Cell Enhancer for Broadband Wireless Access Systems

6. Cell Enhancer for Broadband Wireless Access Systems

6.1 Introduction

The demand is increasing for high-speed wireless multimedia communications, such as Internet access via wireless portable terminals. High performance radio LAN type 2 (HIPERLAN2) developed by ETSI-BRAN [6.1] and the High Speed Wireless Access Network (HiSWANa) developed by MMAC [6.2] represent the outcome of discussions concerning broadband wireless access systems in the 5-GHz U-NII band [6.3]. Both standards have very similar physical layer specifications as a result of harmonization between the standards. These systems provide high-speed (up to 54-Mbps data rate) wireless communications between portable terminals and broadband IP, ATM, and other types of core networks. The typical operating environment is indoors such as a wireless LAN in an office or a factory, or as a wireless Homelink, and user mobility is supported within a local service area. Furthermore, centralized control makes it possible to guarantee various levels of Quality of Services (QoSs) to users [6.3], [6.4]. The notable characteristics of the systems are: (1) that it adopts orthogonal frequency division multiplexing (OFDM), which provides robustness against multipath fading (frequency-selective fading); (2) it uses a dynamic slot assignment (DSA) scheme, i.e., scheduling at an access point (AP) with flexible responses to traffic; and (3) it supports transmit power control (TPC) to reduce the interference to mobile satellite service (MSS) systems. Note that TPC is required in HIPERLAN2, but it is an optional function in HiSWANa.

Although a 5-GHz band is excellent in providing broadband radio channels, it has difficulty in realizing wide area coverage in comparison to the UHF band because of its relatively high propagation loss. The high values of path loss and diffraction loss cause blind areas to occur more frequently in indoor radio zones. In addition, the 5-GHz indoor access system is limited in terms of effective isotropic radiated power (EIRP) for the purpose of frequency sharing with other systems. The cell radius of the target systems calculated based on the transmission of 36 Mbps by using the path loss model in the ITU-R recommendation [6.5], is approximately 30 m. A cell radius of greater than twice this distance is required for a large office [6.6]. This chapter proposes a radio repeater that targets HIPERLAN2 and HiSWANa without system modification to expand the coverage area of one AP. Employing a radio repeater is one of the methods that extends the radio zone by amplifying the received signals and transmitting them again. However, the DSA scheme in the target systems demands dynamic switching of the relaying direction according to the scheduling of the AP. No radio repeater that is applicable to the DSA scheme in the target system has been developed yet. The radio repeater proposed in this chapter adopts a non-regenerative repeating scheme to transfer signals since it achieves a good balance with DSA based on its short processing delay, and it can be implemented using relatively simple circuits [6.7]. I show that the repeating system with the proposed repeater suitably extends the radio zone in a large office. In this chapter, the proposed radio repeater is referred to as a cell enhancer (CE).

Conventionally the non-regenerative repeating system has been employed in digital microwave communications. In this system, known as the heterodyne repeating system, a relay station converts the received signals to intermediate frequency (IF) signals, and after amplifying them with an auto gain controller (AGC), it transmits the signals at different radio frequencies. To apply the CE to the target systems, two novel approaches are proposed in this chapter. One involves the timing control. In order to apply this approach to DSA, the CE extracts the slot assignment information of each frame by demodulating the broadcast signals from the received signals. Based on this timing information, the CE changes the signal direction from the downlink to the uplink or visa versa. The other approach involves gain control. Without fast gain control respective to the received burst signal, the CE makes use of TPC, which the mobile terminal (MT) usually applies to the transmission to the AP. In the downlink, the CE transmits the signals received from the AP to the MTs at the same power level as that used by the AP. In the uplink, the CE receives the signals at a constant power level since the MT applies TPC to the transmission to the CE, and the CE relays the signals to the AP while holding the gain constant.

From the viewpoint of propagation characteristics, as in the ITU-R recommendation [6.5], the delay spread is from 45 nsec to 150 nsec in a 5-GHz indoor environment. In this type of multipath fading environment, broadband wireless transmission is affected by frequency-selective fading. The OFDM system, through use of the non-regenerative repeater, has the following advantage and disadvantage. The disadvantage is that since the CE amplifies the received signals in the whole signal band, some of the subcarriers are degraded by frequency-selective fading which is passed onto the second path of the tandem link. The additive effect of both the AP-CE path and CE-MT path results in more violent subcarrier fluctuations and increased delay spread. To abate this effect, the CE is restricted to locations where stable propagation environments with the AP can be achieved. On the other hand, the advantage is that multiple transmissions are possible in single frequency networks (SFNs) in television relay systems for digital terrestrial video broadcasting (DVB-T) [6.8]-[6.10]. In other words, the AP or MT can receive signals relayed from several CEs by using the same second frequency [6.11]. This makes it easy to increase the number of CEs.

First, this chapter describes the target system design in Section 6.2. Section 6.3 proposes a novel CE (radio repeater) and describes its operating principle. The propagation characteristics of non-regenerative repeating systems are examined by using multipath fading models in Section 6.4. In Section 6.5, the fundamental repeating system performance of the CE is verified by simulating its downlink and uplink performance in the target systems, and its macro diversity gain by using multiple CEs. Section 6.6 concludes the chapter.

6.2 Broadband Wireless Access System

6.2.1 System Configuration

Table 6.1 gives the main system parameters of the target systems [6.1], [6.2]. The coded OFDM employed in these systems achieves superior transmission performance in frequency-selective fading channels. The OFDM guard interval (GI) can eliminate intersymbol interference generated by multipath delay waves. Moreover, it has the effective function of forward error correction (FEC) by using bit interleaving to randomize the errors caused by the frequency-selective fading.

The air interface is based on dynamic Time Division Multiple Access (TDMA) and Time Division Duplex (TDD) [6.1], [6.2]. The Media Access Control (MAC) frame format is shown in Fig. 6.1. The MAC frame has a fixed duration of 2 msec, the former part is for the downlink and the latter part is for the uplink. The AP dynamically schedules and allocates the bandwidth to each MT according to resource requests received from the MTs. The number of slots assigned to each MT and the border between the downlink and uplink are variable in each frame. The broadcast control channel (BCCH), which is carried at the beginning of the frame [6.4], announces the system control information such as the network identifier or AP identifier. The BCCH also includes the information pertaining to the transmitting and receiving power levels of the AP, which are used in the TPC. The following frame control channel (FCCH) provides information regarding the slot assignment. By receiving the FCCH, the MT can identify the position of its assigned slot as the User data channel (UDCH) in the MAC frame.

TPC of the MT is used to simplify the design of the AP receiver and for regulatory reasons to decrease the interference to other systems using the same band [6.1]. The MT transmission power level is set as follows,

$$MT\_Tx\_Level = \min (AP\_Tx\_Level - RSSI + AP\_Rx\_UL\_Level, AP\_Tx\_Level), \quad (6.1)$$

where the AP_Tx_Level denotes the AP transmission power level and the AP_Rx_UL_Level represents the power level that the AP is expecting to receive for the uplink signals. These values are carried by the BCCH. RSSI is the received signal strength measured by the MT. As a result, the MT transmission power level is controlled so that the power level received at the AP becomes the AP_Rx_UL_Level.

6.2.2 Radio Zone in Indoor 5-GHz Systems

In the case of a wireless LAN in a large office, it is preferable that the AP be established at a location overlooking all the MTs such as affixed to the ceiling in the center of a room. However, the difficulty in wiring construction sometimes places the AP unavoidably at the edge such as in the corner. Since partitions or office automation equipment may block microwaves, blind service areas occur. Increasing the number of APs, which seems to be the easiest way to address this problem,

Table 6.1 Main system parameters.

Standardization body	ETSI BRAN	MMAC
System	HIPERLAN/2	HiSWANa
Frequency	5.15-5.35, 5.47-5.725 GHz	5.15-5.25 GHz
Channel spacing	20 MHz	
Modulation	Coded OFDM with 52 subcarriers	
Transmission rate	6, 9, 12, 18, 27, 36, (54) Mbps	
Frame length	2 msec	
Multiple access	TDMA-TDD with DSA	
TPC	Mandatory	Option

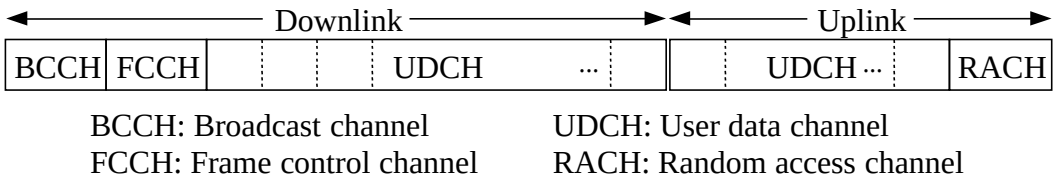

Fig. 6.1 MAC frame format.

increases the cost of the system construction. The blind areas must be eliminated without increasing the EIRP. Although the data rate of one AP is enough to meet the system capacity, to expand the coverage area, a radio repeating system that has a high performance level even in severe multipath environments is sorely needed for 5-GHz indoor access systems. Figure 6.2 shows radio repeating system configurations. Radio repeaters can be easily established at relatively low cost; only power source wiring is needed.

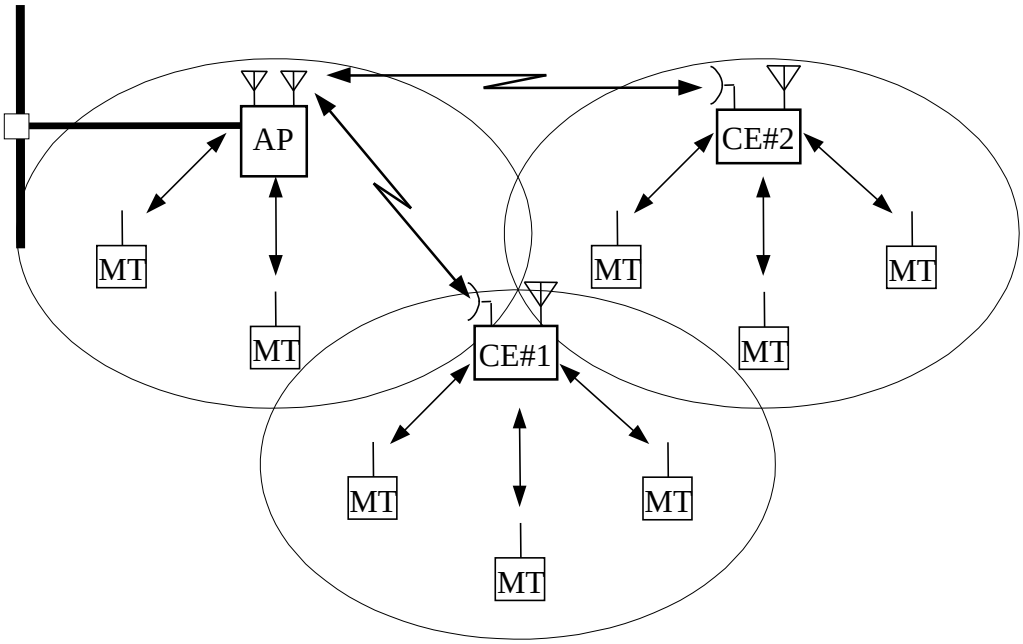

Fig. 6.2 Radio repeating system configuration.

6.3 Proposed Radio Repeating System

6.3.1 Repeating System Comparison

In this subsection, the radio repeating system is classified into four basic configurations and the most suitable candidate for the target systems is selected. Figure 6.3 shows the four radio repeating system configurations and Table 6.2 shows the comparative results. The direct repeating system of Fig. 6.3(a) is employed in DVB-T to achieve SFN [6.8]-[6.10]; the same frequency is used by the transmitting and receiving antennas. However, given the small antenna size of wireless access systems, it is very hard to ensure sufficient isolation between the antennas [6.12]. In contrast, the non-regenerative repeating system of Fig. 6.3(b), also known as the heterodyne repeating system [6.7], avoids the antenna coupling problem because it uses different frequencies, and applies small antennas consequently. The regenerative repeating system, Fig. 6.3(c), makes it necessary to increase the guard time to allow for the processing delay of the modulator and demodulator. The digital processing delay of the OFDM is particularly long and this decreases the frame efficiency. On the other hand, in Fig. 6.3(b), the delay of the analog circuits is acceptably short. Figure 6.3(d) shows a repeating system with a buffer which stores the received data in one frame and transmits them in the succeeding frame. This type is employed to establish the Home Antenna in the personal handy-phone system (PHS). However, because the slot assignment is different in each frame, this method cannot be applied to the target systems. The above discussion suggests that non-regenerative repeating systems are the most suitable for the target systems, because it is possible to support the DSA scheme by transferring the signals with no processing delay.

On the issue of transmission quality, Fig. 6.3(c) and Fig. 6.3(d) carry over no waveform distortion by means of a 3R function, i.e., Reshaping, Retiming, and Regeneration. Whereas, in the non-regenerative repeating system of Fig. 6.3(b), the signal degradation that occurs in the first path is additive to that in the second path of the tandem link. This chapter evaluates the degree of impact of such a tandem link on the OFDM transmission. Moreover, although the configuration depicted in Fig. 6.3(b) is inferior to that in Fig. 6.3(a) in terms of effectively utilizing the frequency bands, when spare frequency channels do exist in a closed local area, it can improve the coverage probability without the need to establish a new AP.

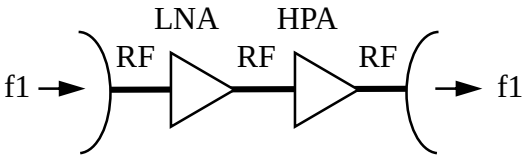

(a) Direct repeating system

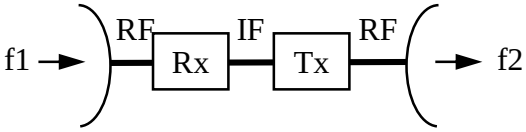

(b) Non-regenerative repeating system

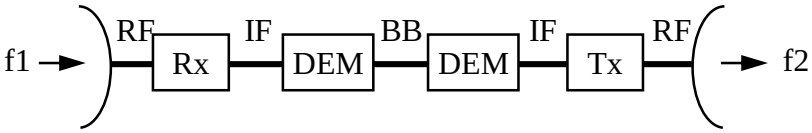

(c) Regenerative repeating system

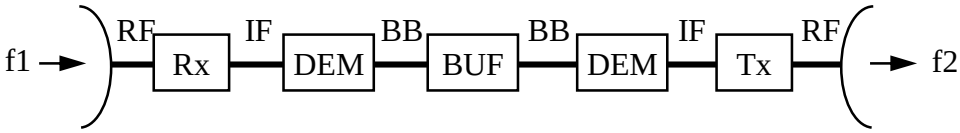

(d) Regenerative repeating system with buffer

Fig. 6.3 Typical radio repeating systems.

Table 6.2 Comparison of radio repeating systems.

Repeating system	Frequency channel	Antenna size	Processing delay	3R function	Suitability
Fig. 6.3(a)	1	Large	Short	Without	Not
Fig. 6.3(b)	2	Small	Short	Without	Highly
Fig. 6.3(c)	2	Small	Long	With	Not
Fig. 6.3(d)	2	Small	1 frame	With	Not

6.3.2 Proposed Cell Enhancer

A block diagram of the proposed radio repeating system is given in Fig. 6.4. The proposed radio repeater (CE) links an AP to some MTs by employing the conventional non-regenerative repeating system, amplifying the received signals with AGC after converting them to IF signals [6.7]. Two antennas are mounted on the CE, one of which is directed towards the AP and the other is an omni-directional antenna for the MTs. Each antenna is connected to a filter to separate the frequency band into f1 and f2, and the IF signal can be extracted into one of the frequency channels using a steep band-pass-filter (BPF) such as a SAW filter. Two TDD switches are used to change the signal direction from the downlink to the uplink or vice versa.

In the initial setting, the CE detects the first frequency channel, f1, which the AP uses by scanning the radio frequency, selects the second frequency channel, f2, which is different from f1, and determines the pairing of the RF filters. In HIPERLAN2, likewise, the CE is required to shift f1 according to the Dynamic Frequency Selection (DFS). These mechanisms are omitted in Fig. 6.4. The MT selects the frequency channel, either f1 or f2, with the higher received power level as the usual BCCH searching procedure.

In order to operate well in the target systems, the CE employs two novel techniques. One of which pertains to timing control, the CE must obtain the timing information of each MAC frame when switching the downlink or uplink. The CE branches off the downlink signals from the relay line and inputs them into the control channel processor through the OFDM demodulator and FEC decoder. The CE drives the TDD SW1 and TDD SW2 using the switching time derived from the FCCH contents at the control channel processor. The other pertains to gain control. When the CE quickly controls the gain with respect to the received burst signals, the magnitude of the signal vibrates to some degree at the beginning of the burst before the AGC circuit stabilizes. If this ringing is transferred from the CE to the AP or the MT, it degrades the performance of the receiver. The proposed gain control method solves this problem by applying TPC, which the MT usually performs on the transmission to the AP as mentioned in Section 6.2. In the downlink, the CE determines the gain, G_down, from the BCCH strength received in the previous frame, and holds the gain constant while relaying the burst. The CE transmits the downlink signals at the same power level of the AP, i.e., AP_Tx_Level. In the uplink, the MT controls the transmission power level based on the BCCH received from the CE. The received signal power level at the CE results in a constant value, AP_Rx_UL_Level. Furthermore, in the uplink, the CE sets the gain, G_up, as follows without regard to the received power level, and the CE transmits to the AP at a constant gain within one MAC frame:

$$G\_up = \min (G\_down, AP\_Tx\_Level - AP\_Rx\_UL\_Level). \quad (6.2)$$

The maximum transmitting power level of the CE is AP_Tx_Level. The G_down corresponds to the propagation loss between the AP and CE, and when it is small, the AP receives the

signal at the power level of AP_Rx_UL_Level. Thus, the gain control of the CE can be performed by applying the current TPC such that the power level received at the AP becomes a constant value.

In addition, the CE also synchronizes the carrier frequency, f1, to the AP by demodulating the BCCH. The second frequency, f2, can be generated from the synchronized reference frequency using a phase locked loop (PLL).

The proposed repeating system is equivalent to the type depicted in Fig. 6.3(b) in that the main signals are transferred with no processing delay. However, the repeater needs a demodulator that demodulates the control channels for the timing control. Therefore, in the target systems, since the CE can obtain the frame timing, the information concerning the power level and the reference frequency of the AP by monitoring the control channels broadcast from the AP, the CE can pose as the AP using the other frequency channel. The MT forms a link with the AP via the CE without the MT realizing that the CE is a copy of the AP.

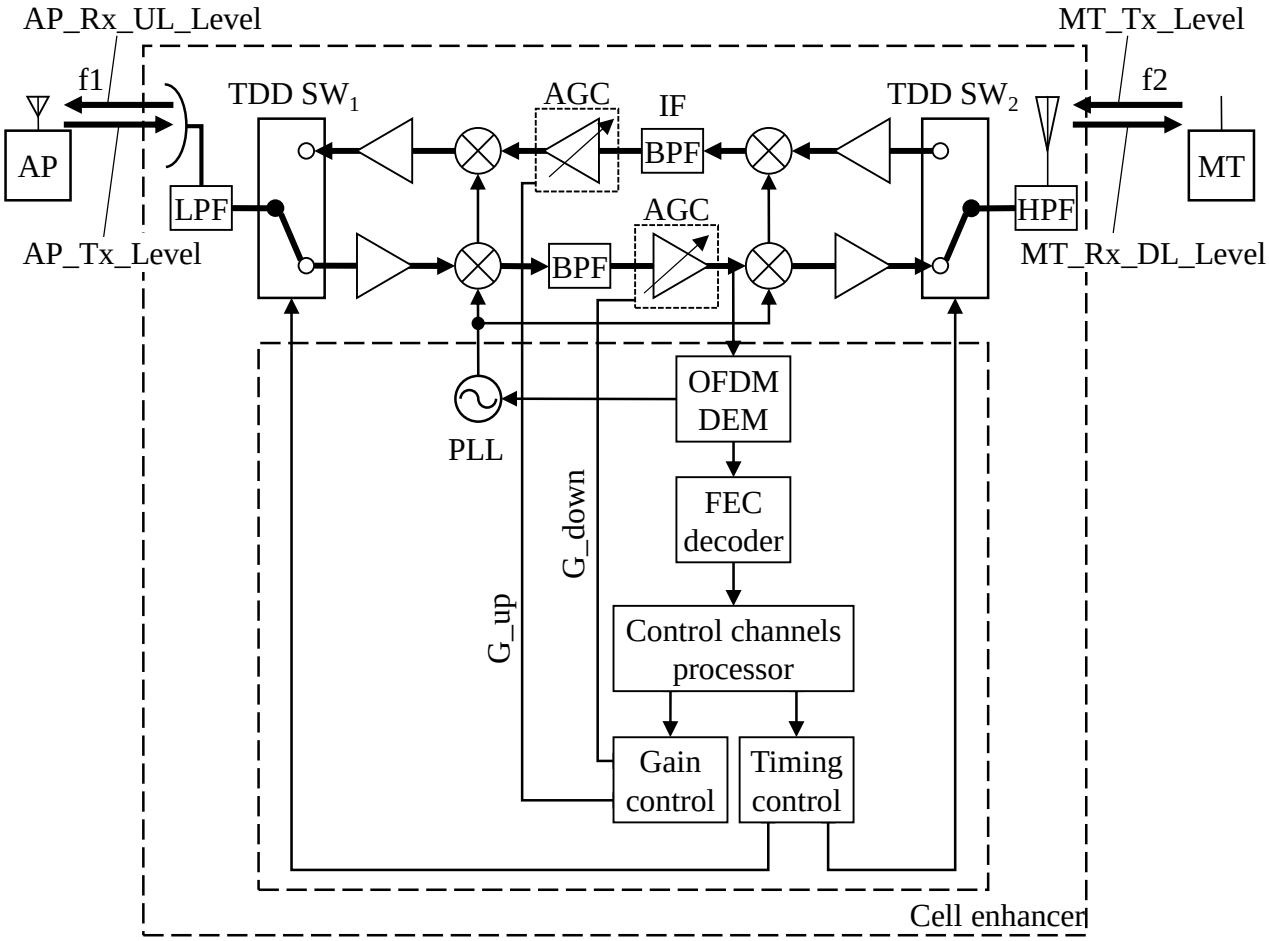

G_down and G_up represent total gain CE.

Fig. 6.4 Configuration of the proposed radio repeating system.

6.4 Propagation Characteristics

This section describes the propagation characteristics assumed in the simulation, for the single-hop case and for the two hops relayed by the non-regenerative repeating system.

6.4.1 Multipath Fading Model of Single hop

A single hop is assumed in each of two multipath fading models. One model provides multipath Rayleigh fading for a non-line-of-sight (NLOS) case with an exponentially decaying power profile as shown in Fig. 6.5(a) [6.13]. The delay interval is sampling duration T_s and the delay profile is expressed by the following equation,

$$P_n = (1 - \exp(-T_s / \sigma_{\text{nlos}})) \cdot \exp(-n \cdot T_s / \sigma_{\text{nlos}}), \qquad n = 0, 1, 2, ..., \tag{6.3}$$

where σ_{nlos} is the root-mean-square delay spread. The probability density function of the magnitude of each delay wave is given as a Rayleigh distribution, and the functions are statistically independent. This model has been referred to in the ITU-R recommendation for the 5-GHz band [6.5], and was used in the standardization of IEEE802.11a as a criterion [6.14].

The other model provides multipath Rician fading for the case where a line-of-sight (LOS) exists as a stable direct wave in addition to multipath Rayleigh-distributed waves as shown in Fig. 6.5(b) [6.15]. Factor k is expressed as the power ratio of the stable direct wave to the multipath Rayleigh-distributed waves. The delay spread, σ_{los}, of multipath Rician fading is given by the following equation,

$$\sigma_{\text{los}} \approx \frac{\sqrt{2k+1}}{k+1}\sigma_{\text{nlos}}, \tag{6.4}$$

which becomes smaller than the σ used to model multipath Rayleigh fading.

When OFDM signals are affected by multipath Rayleigh fading, the cumulative distribution, $F(X)$, of the total instantaneous power of a multicarrier signal, X, is given by the following equation [6.16],

$$F(X) = \sum_{n=0} \frac{1-\exp(-X/P_n)}{P_n \prod_{\substack{m=0 \\ m \neq n}} (1 - P_m / P_n)}. \tag{6.5}$$

Figure 6.6 shows the calculation results and the cumulative distributions of subcarrier power. It is apparent that the total power is stable as the delay spread increases. On the other hand, each subcarrier violently fluctuates regardless of the delay spreads. In the case of multipath Rician fading (Fig. 6.7), the total power is basically constant due to the presence of the stable direct wave. When k = 3 dB, even if the Rayleigh-distributed waves are lost entirely, the reduction in total power is only 1.8 dB, while the power of each subcarrier decreases extensively. This fact means that frequency-selective fading does not damage all subcarriers simultaneously, only some. These facts occur when the inverse number of the delay spread is larger than the subcarrier frequency spacing yet

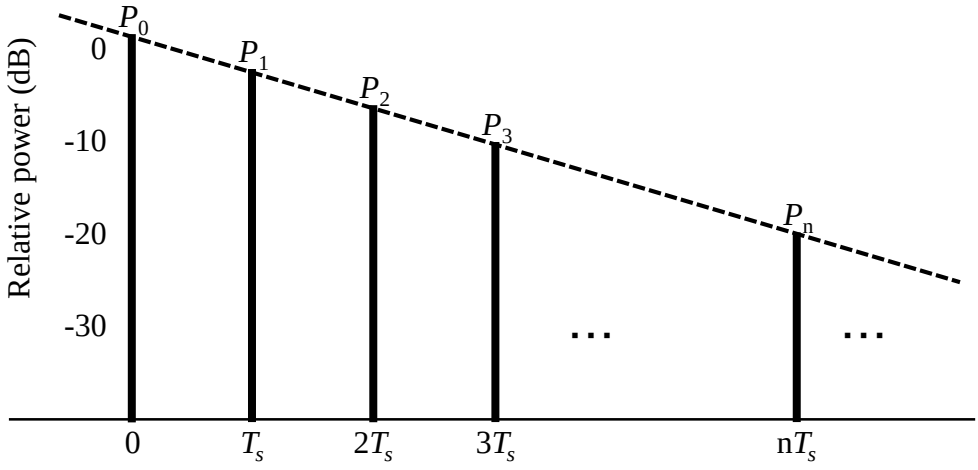

(a) Multipath Rayleigh fading

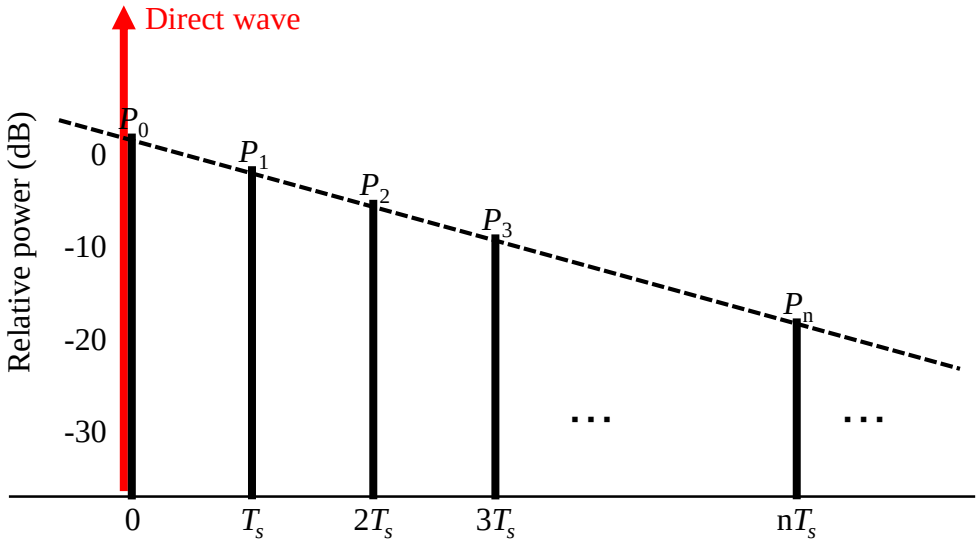

(b) Multipath Nakagami-Rice fading

Fig. 6.5 Multipath fading models.

smaller than the whole signal band. OFDM systems perform well in this case, and in order to establish this scenario, the number of the subcarriers is designed for the delay spread of the assumed environments.

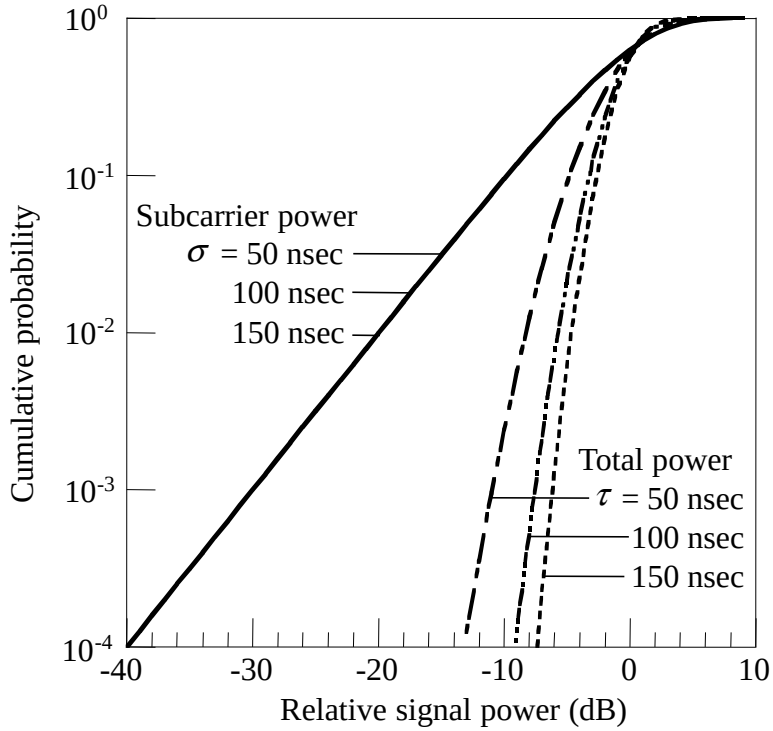

Fig. 6.6 Comparison of distribution under multipath Rayleigh fading.

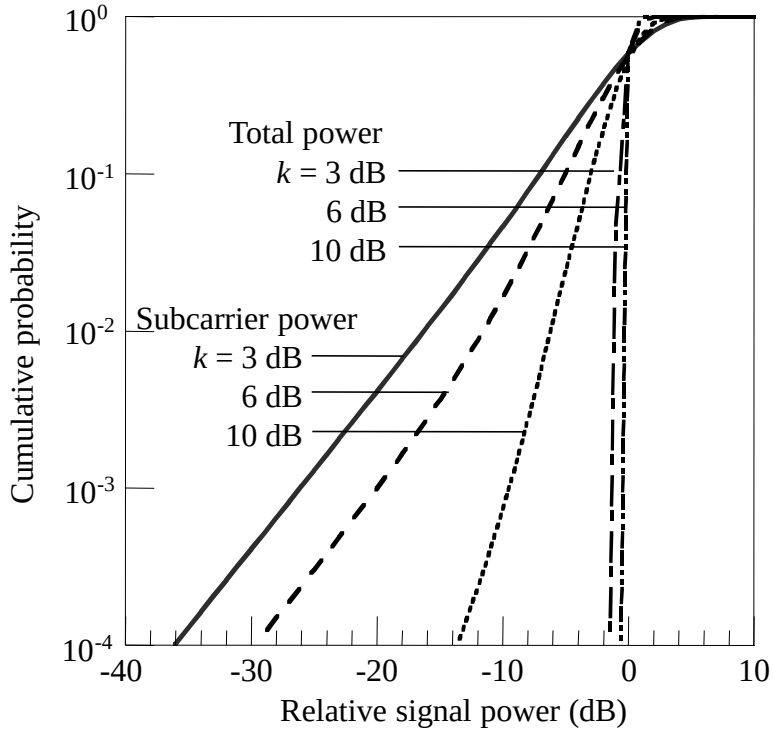

Fig. 6.7 Comparison of distribution under multipath Nakagami-Rice fading.

6.4.2 Propagation Characteristics with Non-regenerative Repeating System

Figure 6.8 shows an example when the CE relays OFDM signals over two hops. The frequency spectrums and the delay profiles of AP-CE ($Path_1$), CE-MT ($Path_2$), and the coupled path ($Path_{1+2}$) through the CE are shown in this figure. The AGC of the CE amplifies the total signal, not the individual subcarriers. For this reason, when the received power levels of each subcarrier are decreased by the same degree by flat fading, the AGC can amplify the subcarriers equally. However, when some subcarriers are degraded by frequency-selective fading in $Path_1$ as shown in Fig. 6.8, they would be passed to $Path_2$ without recovery of the notch, and they would degrade further in $Path_2$. Thus, due to the fact that the fading of both paths is additive by relaying the signal (see $Path_{1+2}$ in Fig. 6.8), the individual subcarriers fluctuate more violently than in the single-hop case. By combining the two distributions of the subcarrier power from the respective paths, this results in a product distribution. For example, the probability density function and the cumulative distribution of the product distribution of two Rayleigh-distributions, are calculated as

$$f_{12}(z) = \int_0^\infty \frac{1}{\Gamma}\exp(-\frac{x}{\Gamma})\frac{1}{x}\exp(-\frac{z}{x})dx = \frac{2}{\Gamma}K_0(2\sqrt{z/\Gamma}), \tag{6.6}$$

$$F_{12}(z) = \int_0^z \frac{2}{\Gamma}K_0(2\sqrt{z'/\Gamma})dz' = 1-2\sqrt{z/\Gamma}K_1(2\sqrt{z/\Gamma}), \tag{6.7}$$

where x is power variables of one path and z is that of the coupling path. Term Γ is the average received power, $K_0(z)$ is a modified Bessel function of the first kind with zero order, and $K_1(z)$ has the order of 1. This is similar to the case of reflection from building walls, and the derivation of the product distribution is detailed in [6.17]. Figure 6.9 shows the calculation results. The power variation of the product distribution exceeds that of the Rayleigh-distribution of the single-hop case. Figure 6.9 shows several samples of the product distribution of the Rayleigh and Rician distributions. As the k factor increases, the product distribution becomes similar to the Rayleigh distribution.

Next, since the non-regenerative repeating system uses different radio frequencies, each path seems to be independently affected by fading. It is expected that the delay spread increases according to the following additivity of variance,

$$\sigma_{1+2} = \sqrt{\sigma_1^{\,2} + \sigma_2^{\,2}}, \tag{6.8}$$

where σ_1 and σ_2 are the delay spreads of $Path_1$ and $Path_2$, respectively. Term σ_{1+2} is the delay spread of the coupling path with the CE as shown in Fig. 6.8. To verify this relation, I measured the delay spreads using a shielded room. Figure 6.10 shows the measurement configuration. The transmitter (Tx1 and Tx2) and the receiver (Rx1 and Rx2) are used to measure delay profiles using a PN sequence [6.18]. The repeater consists of the receiving antenna, the transmitting antenna, and the amplifier, and it directly relays the signal. First, the delay spread of $Path_1$, σ_1, was measured. Second, the delay spread of $Path_2$, σ_2, was measured. At the same time, the delay spread of $Path_{1+2}$, σ_{1+2},

relayed through the repeater was measured. This measurement was done several times while changing the position of the MT. Since I dealt with only one frequency in the experiments, I used a shielded room so that the AP would not receive the signal directly from the MT, and so that the antenna coupling problem would not occur at the repeater. Figure 6.11 shows that the experimental results agree fairly well with Eq. (6.8). As a simple example, when σ_1 and σ_2 are each 150 nsec, σ_{1+2} becomes 212 nsec. This fact indicates that the intersymbol interference is further increased by the growing multipath delay waves.

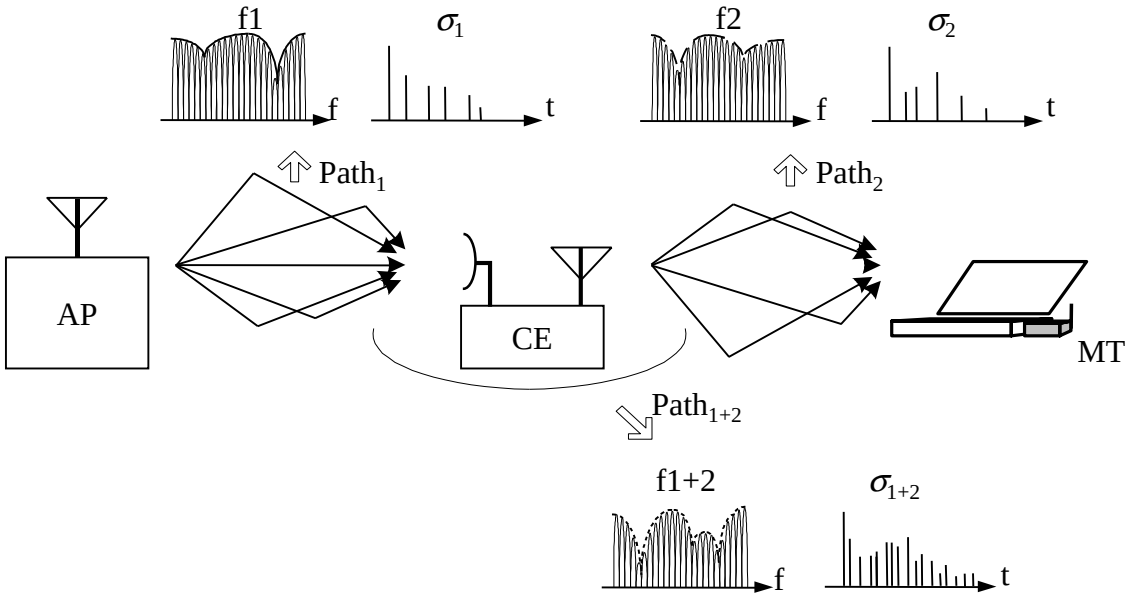

Fig. 6.8 Degradation over two hops.

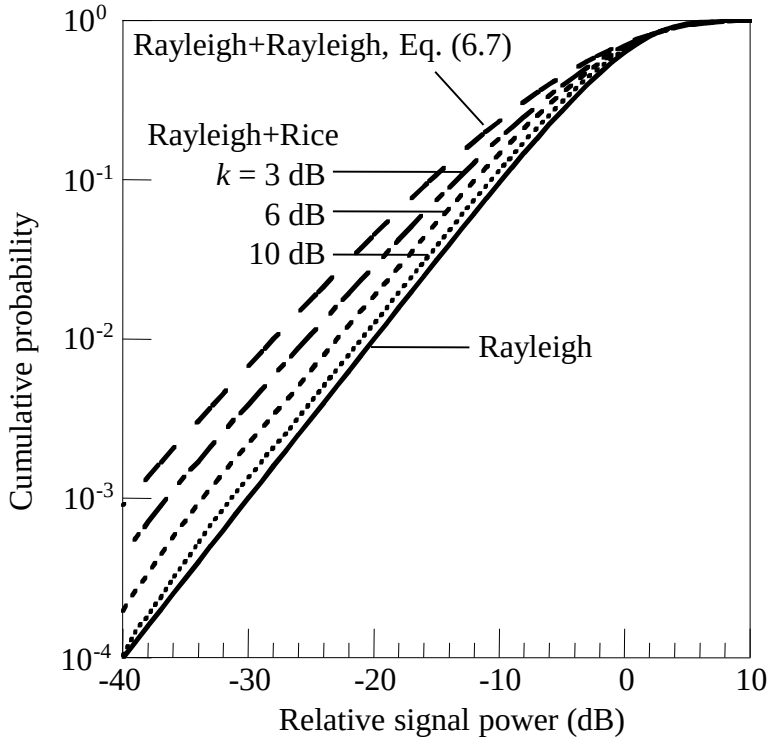

Fig. 6.9 Cumulative probability of product distribution.

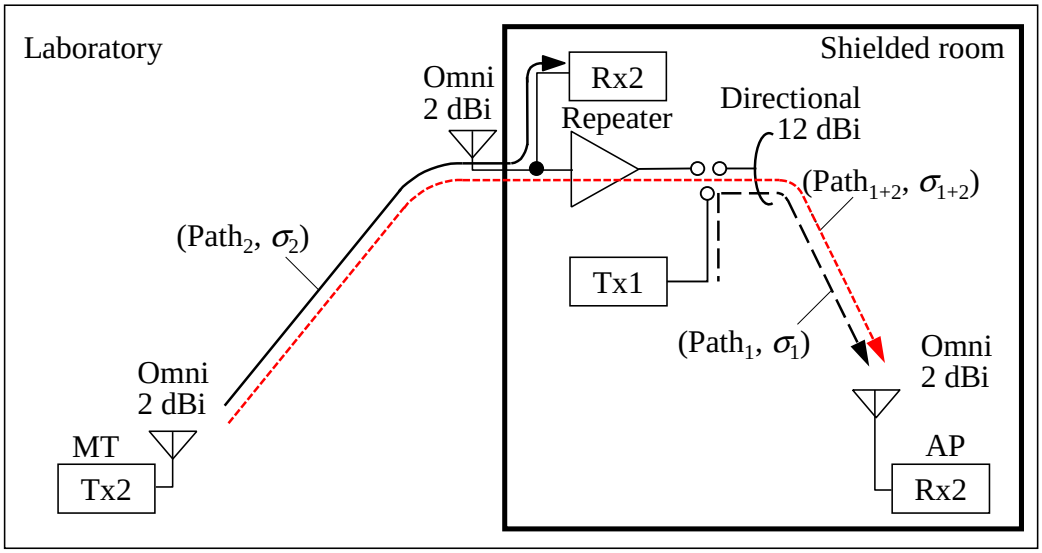

Frequency: 5.2 GHz
Scattering code: PN series 10 steps
Transfer rate: 60 MHz
Modulation: BPSK
Demodulation: Sliding correlation detection

Fig. 6.10 Measurement configuration for delay spread.

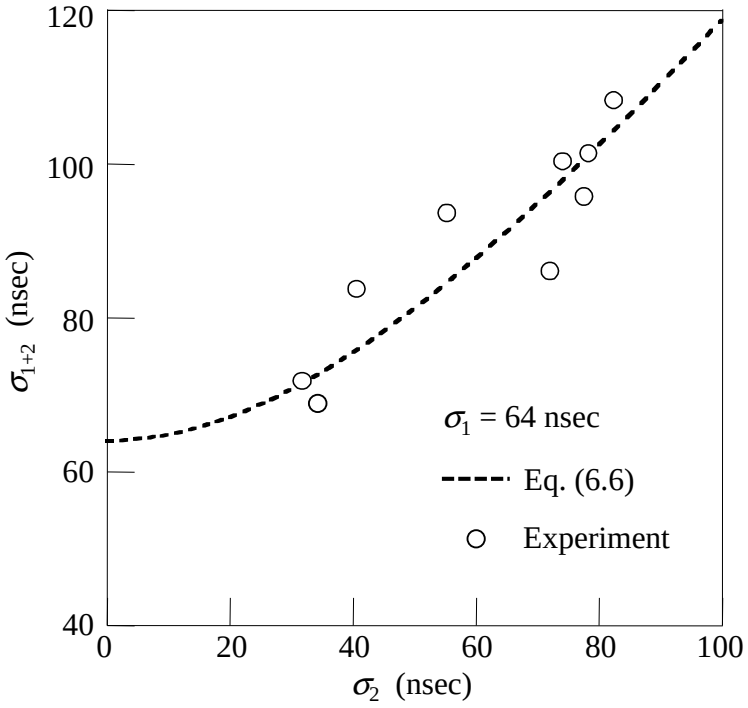

Fig. 6.11 Increase in delay spread with coupled path.

6.5 Performance Evaluation

6.5.1 Fundamental BER Performance

This subsection analyzes the fundamental bit error rate (BER) performance for the single-hop and the two-hop cases. The simulation parameters are listed in Table 6.3 [6.14], [6.19]. I consider here OFDM signals in which the subcarrier modulation scheme employs 16-quadrature amplitude modulation (16-QAM) without FEC. The GI duration is 800 nsec within the OFDM symbol interval of 4 μsec. Initially, for the single-hop case without the CE, the average BER performance of a 16-QAM single carrier in a Rayleigh fading channel is calculated as

$$\overline{Pe_1} \approx \int \frac{3}{8}\mathrm{Erfc}\left(\sqrt{\frac{x/n}{10}}\right)\frac{1}{\Gamma}\exp\left(-\frac{x}{\Gamma}\right)dx$$

$$= \frac{3}{8}\left(1-\frac{1}{\sqrt{1+10n/\Gamma}}\right), \tag{6.9}$$

where Γ/n is the average CNR [6.20]. Next, OFDM transmission was simulated in the multipath Rayleigh fading channel shown in Fig. 6.5(a). The results are shown in Fig. 6.12 with delay spread σ as a parameter. Since the received power levels of each subcarrier are Rayleigh-distributed as shown in Fig. 6.6, when σ is small (i.e., σ = 50 nsec), the BER performance is close to Eq. (6.9). However, the BER floor rises as σ increases due to the intersymbol interference generated by the delay waves that exceed the GI duration.

Second, the BER performance using the CE was examined. The fading channels were assumed to be the product distribution combined with two Rayleigh fading channels, which is represented as Eq. (6.6) in the previous subsection. In much the same way as in Eq. (6.9), the average BER performance of the 16-QAM single carrier is approximately given by

$$\overline{Pe_{12}} \approx \int \frac{3}{8}\mathrm{Erfc}\left(\sqrt{\frac{z/n}{10}}\right)\frac{2}{\Gamma}K_0\left(2\sqrt{z/\Gamma}\right)dz$$

$$= \frac{3}{8}\left\{1-\frac{\sqrt{\pi}}{2}U\left(\frac{1}{2},0,\frac{10n}{\Gamma}\right)\right\}, \tag{6.10}$$

where U(a, b, c) is a confluent hypergeometric function. The OFDM transmission was simulated in this case; the results are shown in Fig. 6.12 with the same delay spread, σ, in both paths. Adding the CE degrades the BER performance as a result of the product distribution. Moreover, the BER floor rises as the delay spread increases as predicted from Eq. (6.8).

Table 6.3 Simulation parameters.

Data rate	36 Mbps
Modulation	16-QAM-COFDM
FEC	Convolutional coding and Viterbi decoding
Coding rate	3/4
Constraint length	7
Number of subcarriers	48
Subcarrier frequency spacing	312.5 kHz
OFDM symbol interval	4 μsec
Guard interval duration	800 nsec
Packet length	54 bytes

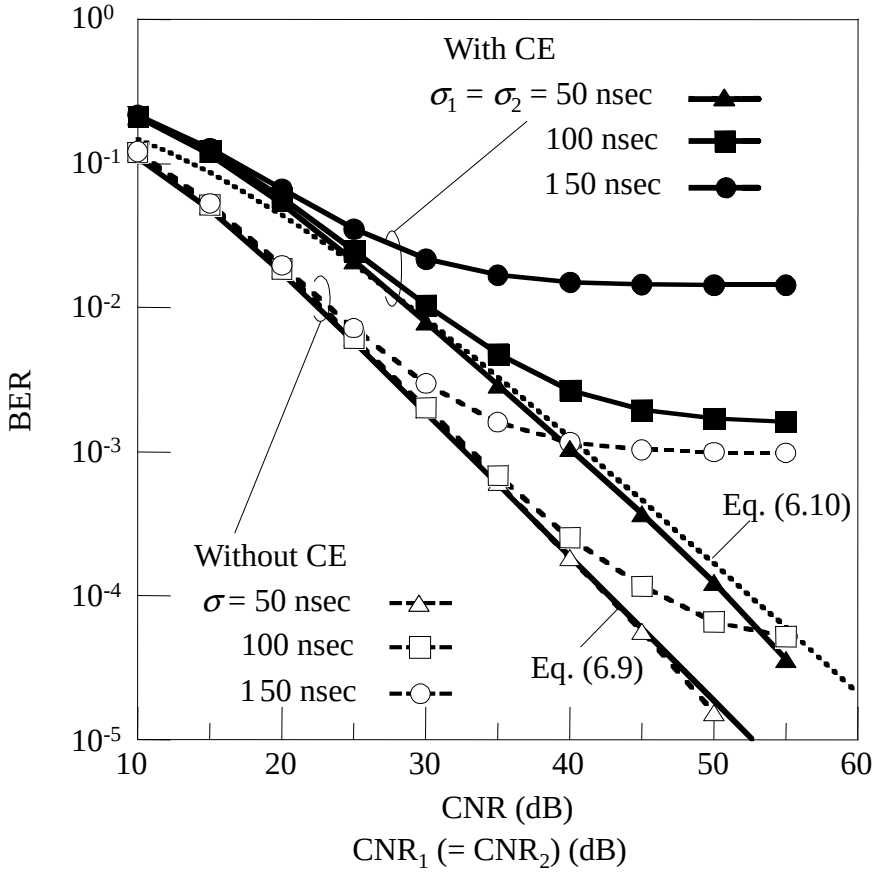

Fig. 6.12 Fundamental BER performance with and without CE.

6.5.2 Downlink PER Performance

The CE performance in the target systems is evaluated in this subsection. The performance is evaluated in terms of the packet error rate (PER) where the packet length is 54 bytes. The simulations consider coherent detection for 16-QAM; carrier recovery and symbol synchronization are assumed to be ideal [6.19], [6.21]. For FEC, convolutional coding and Viterbi decoding (constant length = 7) with a coding rate of 3/4 are applied together with interleaving. The simulation diagram is shown in Fig. 6.13. Stable propagation environments such as $Path_1$ (AP-CE) can be achieved by placing the CE in a clear LOS path to the AP and using a directional antenna. For this reason, the fading of $Path_1$ is assumed to be multipath Rician fading with the k factor as a parameter. $Path_2$ (CE-MT) is considered to be the multipath Rayleigh fading channel case with the delay spread σ_2 of 150 nsec, which is a value referred to by the ITU-R as being representative of a large office [6.5]. In contrast, the delay spread of $Path_1$, σ_1 can be suppressed according to Eq. (6.4). The relations between the k factor and the delay spread are given in Table 6.4. In the downlink, as shown in Fig. 6.13(a), the CE receives the signals degraded by $Path_1$ fading, and transmits the signals to the MTs, after amplifying them to the same power level as that used by the AP. With regard to the CNRs of the received signals in each path, the CNR_1 of $Path_1$ and CNR_2 of $Path_2$ are set to equal values. The downlink PER performance is given in Fig. 6.14. The PER performance improves as k increases. The reason for this is that the product distribution of the coupling path approaches a Rayleigh-distribution (see Fig. 6.9), and the delay spreads can be reduced. For example, when k = 10 dB, the degradation with the CE becomes 1.5 dB at a PER of 1%. Therefore, it is very important for the CE to hold the direct wave stable from the AP. When the appropriate antenna configuration can be chosen, a k factor value greater than 8-10 dB is easily acceptable [6.22]. Directional gains over 10 dB can be achieved with a patch antenna.

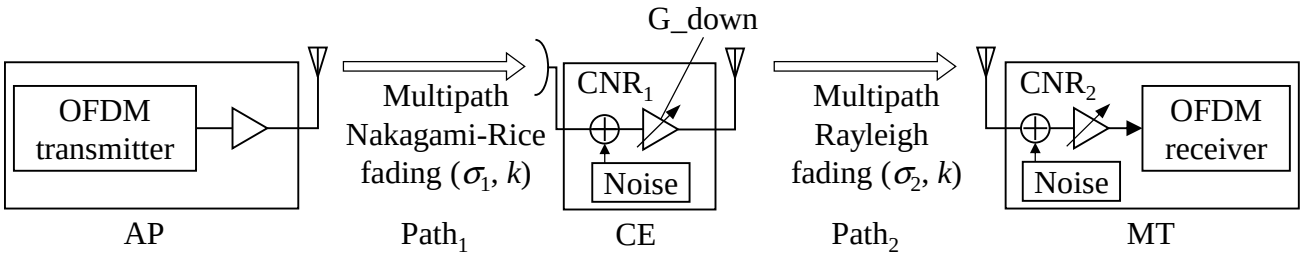

(a) Downlink

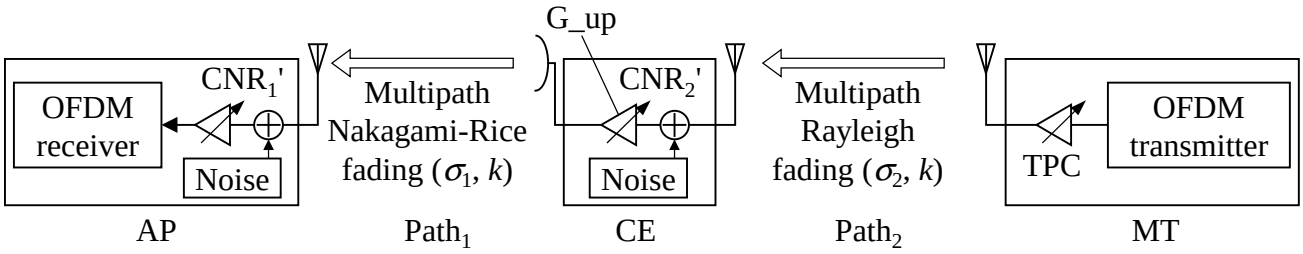

(b) Uplink

Fig. 6.13 Simulation diagram with CE.

Table 6.4. Relation between k factor and delay spreads.

	σ_1 (nsec)	σ_2 (nsec)	σ_{1+2} (nsec)
Case 1 Rayleigh + Rayleigh	150	150	212
Case 2 Rice + Rayleigh k = 3 dB k = 6 dB k = 10 dB	 112 90 62	 150 150 150	 187 175 162

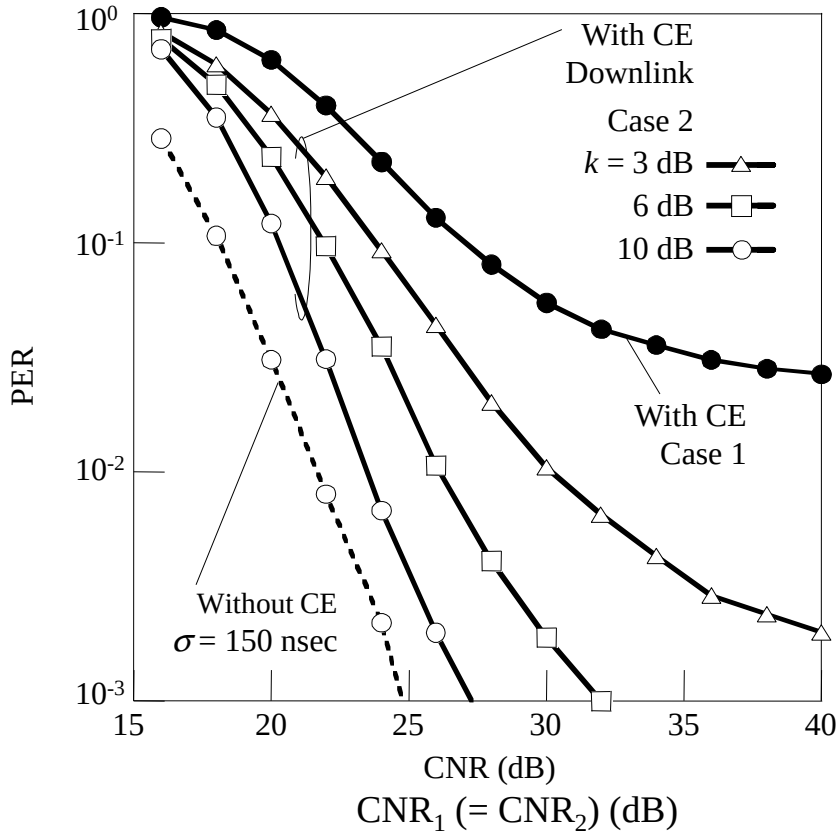

Fig. 6.14 Downlink PER performance.

6.5.3 Uplink PER Performance

The CE performance in the uplink as shown in Fig. 6.13(b), is estimated. As mentioned in Section 6.3, the MT performs TPC for the propagation loss of $Path_2$, and the CE controls the gain for the propagation loss of $Path_1$. The fading conditions of each path are the same as those of the downlink. The uplink PER performance is shown in Fig. 6.15. The uplink exhibits worse PER performance than the downlink. The reason for this is that in the uplink, the CE receives the signals degraded by severe frequency-selective fading compared to the downlink, and it transfers the signals while the power of some subcarriers is severely decreased. In contrast, in the downlink, since the CE receives the signals affected by the respective flat fading, it can amplify each subcarrier uniformly. In addition, the CNR of the downlink signals is relatively high because the CE points the receiving antenna, which has directional antenna gain, toward the AP. However, in the uplink, since the CE must use an omni-directional antenna, which has a small receiving gain, toward the MTs, the CNR of the uplink signal is low.

Figure 6.16 shows the relation between CNR_1 and CNR_2 in the downlink, and the relation between CNR_1' and CNR_2' in the uplink, required to achieve a PER of 1%. It is apparent that the minimum required CNR_1' of the uplink must be 5 dB higher than CNR_1 of the downlink. Both CNR_1 and CNR_1' must exceed 30 dB, if both links are to have the same PER performance. Then the required CNR in $Path_2$ becomes 23 dB. As a simple sketch of the zone design, when radio frequency = 5200 MHz, EIRP = 200 mW, and kTBF = -91 dBm, the indoor path loss model of ITU-R is represented as follows [6.5],

$$L = 20*\text{Log}(\text{frequency}) + 31*\text{Log}(d) - 28. \quad (6.11)$$

Provided that all the receiving antenna gain values are zeros, without the CE, the distance between the AP and MT is about 30 m to achieve the required CNR of 22 dB (see Fig. 6.14). However, when the CE is employed, because the path between the AP and CE with a LOS component is dominated by free-space loss, this distance results in 77 m to acquire the CNR of 30 dB. In addition, the distance between the CE and MT is approximately 28 m to achieve the required CNR of 23 dB from Eq. (6.11).

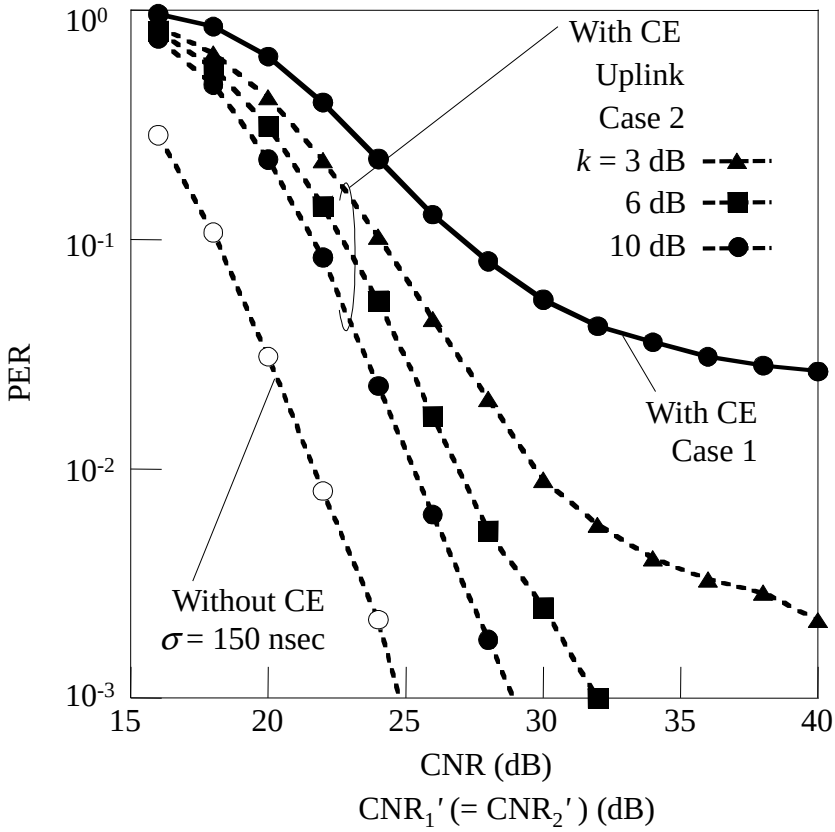

Fig. 6.15 Uplink PER performance.

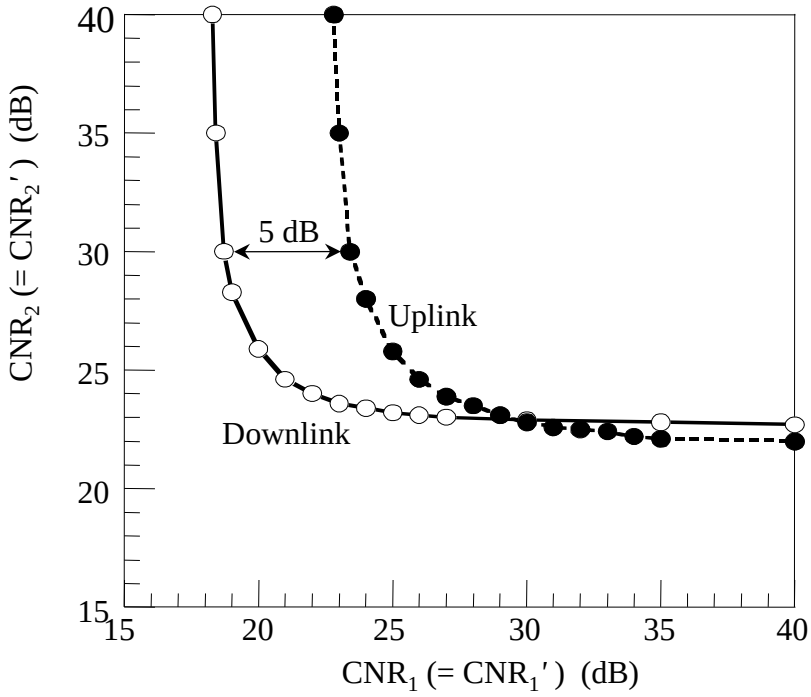

Fig. 6.16 Required C/N ratio of $Path_1$ and $Path_2$ with PER = 1% (k = 10 dB, Case 2).

6.5.4 Performance of Multiple CEs

Figure 6.17 shows the simulation model for the case in which two CEs transfer the same signal from an AP to an MT [6.23]. The two signals received at the MT are set to the same power, and all CNRs are the values needed to achieve the PER of 1% with a single route. The two CEs use the same second frequency; it is assumed that both CEs are fully synchronized to the reference frequency of the AP. Figure 6.18 shows the simulation results with the *k* factor as the parameter. When the delay difference between the two received signals is less than 300 nsec, the PER performance is improved relative to the single route since the two signals are received with little intersymbol interference. Due to the influence of the multipath delay waves, the tolerable delay difference becomes smaller than the OFDM GI duration of 800 nsec. Note that the delay difference of 300 nsec corresponds to the propagation distance of about 90 m, since the difference in the processing delay created within the two CEs is negligible. This range appears to be common in indoor environments. It is generally accepted that transmission quality is degraded if the Doppler shift exceeds 1% of the OFDM subcarrier spacing, which is likely to occur if the MT moves [6.24]. Although the Doppler shift with microwaves is larger than that with either VHF or UHF, the difference is small due to the wide subcarrier spacing, 312.5 kHz, and it is negligible when walking. Consequently, multiple CEs can use the same second frequency with the aims of increasing the macro diversity gain and providing better coverage. In other words, the MT can easily move from one CE area to a neighboring CE area without switching the route.

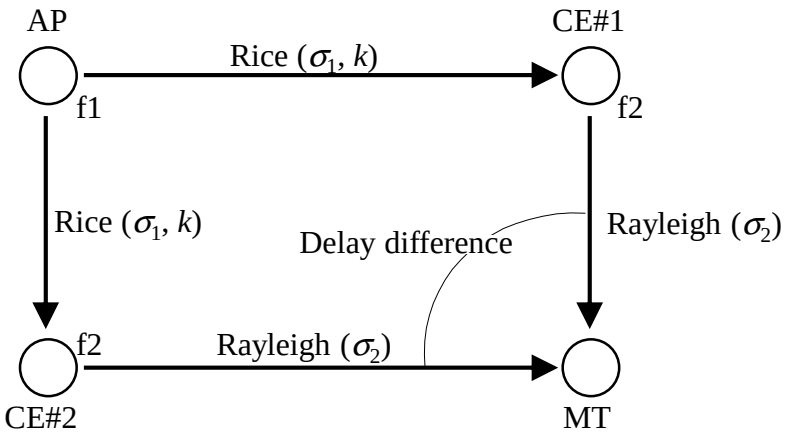

Fig. 6.17 Dual route configuration.

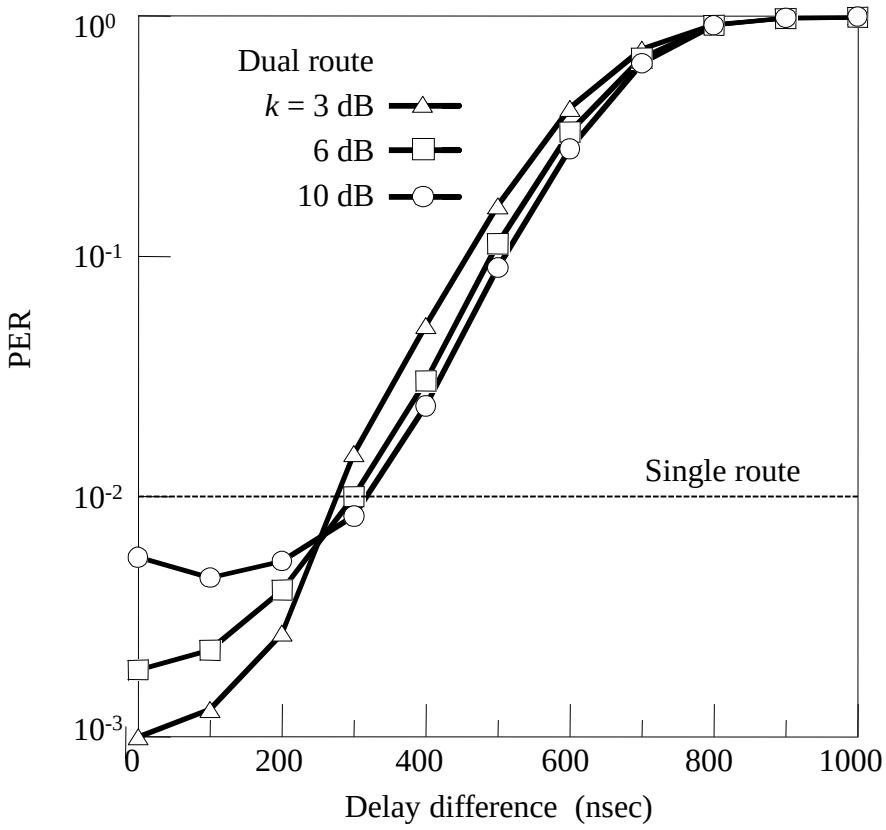

Fig. 6.18 PER performance vs. delay difference
(D/U = 0 dB, Case 2).

6.6 Conclusion

This chapter proposed a radio repeater, the cell enhancer (CE), to extend the radio zone in broadband wireless access systems such as HIPERLAN2 or HiSWANa. The CE adopts a conventional non-regenerative repeating scheme to transfer signals and implements two novel approaches, timing control and gain control, to apply to the target systems. The CE switches signal direction, downlink or uplink, based on the timing information of every MAC frame by monitoring the control channels broadcast from the AP. In addition, without fast gain control in response to the received burst signal, the CE holds the gain constant while relaying the burst by applying the current TPC of the MT. Thus, the CE is applicable to the DSA scheme in the target systems.

Furthermore, I evaluated the propagation characteristics of the two hops formed by the CE, and clarified that the distribution of the OFDM subcarrier power turns into a product distribution (see Eq. (6.6)), and that the delay spread increases (see Eq. (6.8)). I simulated 16-QAM-COFDM transmission of 36 Mbps in the target systems. The antenna system and the CNRs required for the CE to achieve a PER of 1% were clarified from the viewpoint of maintaining a stable propagation environment for the AP. As a result, by setting the CE such that the CNR of over 30 dB to the AP is maintained, the required CNR of the path between the CE and MT becomes 23 dB. In addition, I found that using multiple CEs yields a useful macro diversity gain with little intersymbol interference in indoor environments.

I concluded that the proposed CE suitably extends the radio zone of the target systems in indoor environments such as a large office. Furthermore, the CE will also be applicable to fixed wireless access (FWA). For example, by setting the CE beside a window, it can combine indoor 5-GHz systems with outdoor systems using another frequency such as 2.4-GHz or quasi-millimeter wave bands.

References for chapter 6

[6.1] ETSI. BRAN, “HIPERLAN Type 2; physical (phy) layer. Technical Specification ETSI TS 101 475 V1.2.2 (2001-02),” ETSI, Feb. 2001.

[6.2] ARIB-STD-T70; “Broadband Mobile Access Communication System (HiSWANa),” Ver. 3.1, Nov. 2005.

[6.3] M. Umehira, H. Hojo, T. Manabe and H. Tanaka, “Development of an Advanced Wireless Access System,” NTT R&D, vol. 50, no. 2, pp.66-75, 2001.

[6.4] O. Kagami, A. Sato, S. Kurosaki, N. Kita and T. Tsubaki, “An Advanced Wireless Access System - System Design -,” NTT R&D, vol. 50, no. 2, pp.76-85, 2001.

[6.5] Rec. ITU-R P.1238-7, “Propagation data and prediction methods for the planning of indoor radiocommunication systems and radio local area networks in the frequency range 900 MHz to 100 GHz,” ITU-R recommendations, P Series, 2012.

[6.6] N. Kita, S. Uwano, A. Sato D. Mori, H. Hosoya and H. Watanabe, “Characteristics of Delay Spread for a Large Office Building at 5GHz Band,” Proceedings of the 2000 Communications Society Conference of IEICE, B-1-19, 2000.

[6.7] K. Watanabe, “Estimation method of Route Outage Probability in Non-regenerative Repeater Digital Microwave Radio Systems,” IEICE Trans. Commun., vol. E81-B, no.1, pp.89-95, Jan. 1998.

[6.8] W. Bretl and R. Citta, “Single Carrier VSB Digital Television Transmission, Single-Frequency Networks, and Repeater Systems,” IEEE Trans. on Consumer Electronics, vol.42, no.1, pp.1-10, Feb. 1996.

[6.9] Z. Sayeed and V. Weerackody, “Transmit Diversity for Coded OFDM Systems in Single Frequency Networks,” IEEE GCOM’99, vol.1b, pp.852-856, 1999.

[6.10] A. Ligeti and J. Zander, “Minimal Cost Coverage Planning for Single Frequency Networks,” IEEE Trans. on Broadcasting, vol.45, no.1, pp.78-87, March 1999.

[6.11] A. Tsuzuku and H. Fukuchi, “Digital Terrestrial Television Broadcasting with OFDM - A Study of Double Frequency Network -,” ITE Annual Convention, 19-4, 1995.

[6.12] W. T. Slingsby and J. P. McGeehan, “Antenna Isolation Measurements for On-frequency Radio Repeaters,” Ninth International Conference, Antennas and Propagation, No. 407, vol. 1, pp.239-243, 1995.

[6.13] J. G. Proakis, “Digital Communications,” Third Edition, ch14, pp.795-797, McGraw-Hill, 1995.

[6.14] H. Takanashi, M. Morikura and R. van Nee, “OFDM physical layer specification for the 5GHz band,” IEEE802.11-98/072-r6.

[6.15] Y. Karasawa and H. Iwai, “Formulation of Spatial Correlation Statistics in Nakagami-Rice Fading Environments,” IEEE Trans. on Antennas and Propagation, vol. 48, No. 1, pp.12-18, Jan. 2000.

[6.16] W. C. Y. Lee, Mobile Communications Engineering, ch10, pp.307-308, McGraw-Hill, 1982.
[6.17] A. Sato and E. Ogawa, “An Evaluation Method for the Reflection Coefficient of Building Walls,” IEICE Trans. B-II, vol. J72-B-II, No.5, pp.209-217, May 1989.
[6.18] N. Kita, K. Oosawa, A. Sato, H. Watanabe and H. Hosoya, “Characterization of Multipath Delay Profiles for a Wideband Wireless Access System in a 5GHz Band,” IEEE PIMRC'99, vol. 3, pp.1465-1469, Sept. 1999
[6.19] N. Mochizuki, Y. Matsumoto, M. Mizoguchi, T. Onizawa and M. Umehira, “A High Performance Frequency and Timing Synchronization Technique for OFDM,” IEEE GCOM’98, vol.6, pp.3443-34483, 1998.
[6.20] Y. Saito, Digital Modulation Techniques for Wireless Communications, ch5, pp.171, EIC, 1996.
[6.21] S. Uwano, Y. Matsumoto, M. Mizoguchi and M. Umehira, “Linearized Constant Peak-power Coded OFDM Transmission for Broadband Wireless Access Systems,” IEICE Trans. Commun., vol. E82-B, no.12, pp.1932-1938, Dec. 1999.
[6.22] Y. Sun, P. Hafezi, A. Nix and M. Beach, “Indoor Channel Characterization Measurements with Directional Antennas for Future High Frequency ATM Wireless Access Systems,” IEEE PIMRC'97, vol. 1, pp.184-188, 1997.
[6.23] A. Palin and J. Rinne, “Enhanced Symbol Synchronization Method for OFDM System in SFN Channels,” IEEE GCOM’98, vol.5, pp.2788-2793, 1998.
[6.24] R. Nakamura, H. Ohta and A. Tsuzuku, “Digital Terrestrial Television Broadcasting with OFDM - BER Degradation by Doppler Shift -,” ITE Technical Report, vol.21, No.12, pp.73-76, Feb. 1997.

Chapter 7

Conclusions

7. Conclusions

This dissertation presented research results regarding techniques that improve interference compensation and performance evaluation in digital radio systems. As mobile Internet access becomes more widely used and the ubiquity of radio communication devices increases, interference issues will becomes more serious in light of the lack of unused frequency bands. Interference compensation techniques must be established in order to avoid interference in the same system and the interference between different systems, or to expand the coverage area. Interference compensation techniques should be provided without the need to change standard specifications, because interference may not always occur.

However, conventional interference compensation schemes have four main problems that must be addressed to achieve high performance in digital radio systems.

(1) The problem of ACI in the wireless LAN system is caused by nonlinear distortion characteristics of high power amplifiers at the transmitter.

(2) The problem of CCI occurs between BSs in PHS when there is mutual overlapping in a zone in a mixed cell architecture.

(3) The problem of the SPI between two routes in a fixed microwave communication system occurs when the desired signal level is degraded by fading.

(4) The problem of ISI between multiple radio repeaters in a wireless LAN occurs due to the delay difference between the two received waves.

In this study, in order to address these problems, four techniques were established and the following summarizes the results obtained through this research.

(1) The nonlinear distortion compensation technique, which reduces ACI, was established. In Chapter 3, in OFDM systems nonlinear distortion degrades the own transmission quality, and since it causes the spectrum to expand significantly, these out-of-band emission results in ACI. This chapter proposed the nonlinear distortion compensation technique LCP-COFDM. This technique combines the CP-OFDM technique with baseband predistortion. Simulation and experimental results verified that the proposed technique significantly reduces out-of-band power emission and ACI by more than 10 dB, respectively. In this case, given the propagation distance characteristic expressed as a power decay of 2.9 , LCP-COFDM allows the distance between the desired station and adjacent interfering station to be reduced to 1/3 that when not using LCP-COFDM. As a result, multiple APs can coexist without interfering with each other in a small area.

(2) An antenna technique to avoid CCI was established. In Chapter 4, the problem of CCI generated in a mixed cell architecture in microcellular systems was discussed. In this type of microcellular systems in which both microcells and macrocells co-exist in the same geographical urban area, the BS antennas mounted on the rooftops of buildings to cover wide circular radio zones suffer severe CCI from the surrounding low BSs. The combination of beam tilt and horizontal

polarization significantly reduced the CCI level by approximately 23 dB, which is equivalent to a reduction to 1/200 of the interference level that the BS receives. The distance between the interference receiving BS and the interfering BS can be shortened to approximately 1/6.

(3) An interference compensation technique to compensate for SPI was established. In Chapter 5, a theoretical evaluation was performed using the ERIC, which is effective even for SPI. The degree of improvement in the interference cancellation was estimated using this canceller in a fading environment. The results clarified that this canceller is the most valid when the average received signal power rate, D/U, is 20 dB, and the maximum improvement using this canceller is 7.5 times better than without using this canceller. The quality-degradation time due to the interference can be shortened from 28 seconds to 3.7 seconds per 50 km per month for the 16-QAM system in a fixed microwave communication system.

(4) A non-regenerative repeating technique comprising multiple radio repeaters was established without generating ISI. In Chapter 6, a new radio repeater, the CE, was proposed that targets 5-GHz broadband wireless access systems to improve the coverage probability without the need to set up a new AP. It was clarified that multiple CEs can use the same second frequency and provide better coverage with useful macro diversity gain in 5-GHz indoor environments, because when the delay difference between the two received waves is less than 300 ns, the ISI can be removed using the guard interval in an OFDM system.

The above research results show fundamental data regarding interference compensation for the exiting digital radio systems. These results should contribute to promoting the actualization of advanced radio communication systems. Finally, it is my sincere hope that this dissertation will aid in proliferating future radio communication systems.

Acknowledgements

I wish to express my gratitude to Associate Professor Naoto Wakatsuki of the University of Tsukuba for his invaluable advice and continuous encouragement. I am most grateful to Professors Koichi Mizutani, and Assistant Professor Tadashi Ebihara of the University of Tsukuba for their useful discussions.

I sincerely thank Dr. Atsuya Ando of NTT Wireless Systems Innovation Laboratory for his precious advice and unceasing encouragement.

I wish to express my deep gratitude to Associate Professor Takefumi Hiraguri of the Nippon Institute of Technology for his productive advice.

I especially thank Professor Hideaki Matsue of the Tokyo University of Science, Suwa, Professor Akio Sato of the Tokyo University of Technology, Professor Masahiro Umehira of the Ibaraki University and Dr. Kazuji Watanabe for their fruitful discussions and help.

List of publications

1-1 Papers

(J-1) S. Uwano and K. Watanabe, “Estimation Method for Extraction and Reinjection-Type Interference Canceller,” IEICE Trans. Commun., vol. E79-B, No. 3, pp.373-377, March 1996.

(J-2) S. Uwano, Y. Matsumoto, M. Mizoguchi and M. Umehira, “Linearized Constant Peak-Power Coded OFDM Transmission for Broadband Wireless Access Systems,” IEICE Trans. Commun., vol. E82-B, No. 12, pp.1932–1937, Dec. 1999.

(J-3) S. Uwano, “Cell Enhancer for Broadband Wireless Access Systems,” IEICE Trans. Commun., vol. E85-B, No. 5, pp.908-918, May 2002.

(J-4) S. Uwano, A. Ando, T. Seki, Y. Takatori and T. Hiraguri, “Experimental Investigations of Co-channel Interference Reduction Effect at High Elevation Base Station Using Beam Tilt and Orthogonal Polarization”, Hindawi Publishing Corporation International Journal of Antennas and Propagation, vol. 2014, Article ID 532743.

1-2 International Conferences

(P-1) S. Uwano and K. Watanabe, “Symbol synchronization performance using loop switching type quenching method”, IEEE GLOBECOM '97, pp.1199-1203, vol. 3, Nov. 1997.

(P-2) S. Uwano, Y. Matsumoto, M. Mizoguchi and M. Umehira, “Linearized constant peak-power coded OFDM transmission for broadband wireless access systems”, IEEE PIMRC'99, pp.358-362, Sept. 1999.

(P-3) S. Uwano and R. Ohmoto, “Application Area Expansion in Quasimillimeter Wave Band Fixed Wireless Access System”, Proc. 4th International Conference on Networking ICN '05, pp. 76-83, vol. 1, April 2005.